DEVELOPMENT OF THE 2ND GENERATION z(REDSHIFT) AND EARLY UNIVERSE SPECTROMETER & THE STUDY OF FAR-IR FINE STRUCTURE EMISSION IN HIGH-z GALAXIES.

A Dissertation

Presented to the Faculty of the Graduate School

of Cornell University

In Partial Fulfillment of the Requirements for the Degree of

Doctor of Philosophy

by

Carl Ferkinhoff

May 2014

DEVELOPMENT OF THE 2ND GENERATION z(REDSHIFT) AND EARLY UNIVERSE SPECTROMETER & THE STUDY OF FAR-IR FINE STRUCTURE EMISSION IN HIGH-z GALAXIES.

Carl Ferkinhoff, Ph. D.

Cornell University 2014

The 2nd generation z (Redshift) and Early Universe Spectrometer (ZEUS-2), is a long-slit echelle-grating spectrometer (R~1000) for observations at submillimeter wavelengths from 200 to 850 μm. Its design is optimized for the detection of redshifted far-infrared spectral lines from galaxies in the early universe. Combining exquisite sensitivity, broad wavelength coverage, and large (~2.5%) instantaneous bandwidth, ZEUS-2 is uniquely suited for studying galaxies between z~0.2 and 5—spanning the peaks in both the star formation rate and number of AGN in the universe. ZEUS-2 saw first light at the Caltech Submillimeter Observatory (CSO) in the Spring of 2012 and was commissioned on the Atacama Pathfinder Experiment (APEX) in November 2012. Here we detail the design and performance of ZEUS-2, first however we discuss important science results that are examples of the science enabled by ZEUS-2

Using the first generation z (Redshift) and Early Universe Spectrometer (ZEUS-1) we made the first high-z detections of the [NII] 122 μm and [OIII] 88 μm lines. We detect these lines from starburst galaxies between z ~2.5 and 4 demonstrating the utility of these lines for characterizing the properties of early galaxies. Specifically we are able to determine the most massive star still on the main sequence, the number of those stars and a lower limit on the mass of ionized gas in the source.

Next we present ZEUS-2's first science result. Using ZEUS-2 on APEX we have detected the [CII] 158 μm line from the z = 1.78 galaxy H-ATLAS J091043.1-000322 with a line flux of $(6.44 \pm 0.42) \times 10^{-18}$ W m^{-2}. Combined with its far-infrared luminosity and a new Herschel-PACS detection of the [OI] 63 μm line we are able to conclude that H-ATLAS J091043.1-000322 is a high redshift analogue of a local ultra-luminous infrared galaxy, i.e. it is likely the site of a compact starburst due to a major merger. This detection, combined with the ZEUS-1 observations of the [NII] and [OIII] lines represent examples of work we plan to continue with ZEUS-2. As such, they demonstrate the potential of ZEUS-2 for increasing our understanding of galaxies and galaxy evolution over cosmic time.

BIOGRAPHICAL SKETCH

Carl Ferkinhoff was born in St. Cloud, Minnesota on March 4, 1983 into the loving family of William and Karen Ferkinhoff and older sister Jennifer. In 1987 the family moved to the neighboring town, Sartell, where Carl quickly discovered the benefits of drifting snow in construction of winter habitats. About the same time he developed an affinity for LEGOs, spending many hours constructing spaceships and leaving strategically placed LEGO pieces to be lodged in his parent's feet. In 1994, at the suggestion of his mother, he became a fan of Star Trek with the premier of Deep Space Nine. To this day he remains a committed fan of the franchise.

In the real world Carl spent much time fishing and hunting with his father as well as camping with the Boy Scouts. His interest in science was nurtured by these activities and interests as well as his parents support. They themselves had studied biology in college, albeit the degrees were unused during Carl's childhood. By his freshman year in high school he was beginning to consider seriously studying science at college. While an avid reader of science fiction, it was several non-fiction books on physics including Lawrence Krauss' "Physics of Star Trek" and Kip Thorne's "Einstein's Outragous Legacy: Black Holes and Timewarps" that ultimately captured his imagination. These combined with favorite sci-fi works by Frank Herbert and Isaac Asimov cemented his decision to pursue physics in undergraduate.

In the fall of 2001, a graduate of Sartell High School, Carl traveled to Saint Peter Minnesota to start his freshman year at Gustavus Adolphus College. While spending most of his time in physics courses, Carl leveraged the benefits of a liberal arts education by taking courses in history, music, and philosophy as well as being active in many of the college choirs. In his sophomore year he participated in the January term course, "Astronomy of the Southern Skies"

learning about introductory astronomy while spending a month in Australia. Based on his budding interest in Astronomy, Carl spent the summer before his senior year at Cornell University doing research—aka. becoming an expert at soldering—in Prof. Gordon Stacey's research group, his eventual Ph.D. advisor.

After graduating from Gustavus, Carl moved to Baltimore, Maryland in August 2005. He spent the next two years there teaching high school physics and chemistry as a Teach For America corps member and pursuing a Masters of Teaching degree at The Johns Hopkins University School of Education. During the summers he worked as a computer system-administer for Teach For America at their training institute in Philadelphia, PA. Through these experiences he discovered his love of teaching, but also realized that he missed research and the academic setting. He eventually decided to go to graduate school to earn a PhD in Astronomy and become a professor at a small liberal arts college.

Carl chose to attend Cornell University and perform his PhD research with Prof. Gordon Stacey. Since beginning his graduate student career in the fall of 2007 he has focused his research efforts on submillimeter instrumentation and the study of galaxies in the early universe. He has gone on observing trips to the Caltech Submillimeter Observatory on Mauna Kea, Hawai'i and the Atacama Pathfinder Experiment in the Atacama Desert of Chile. In addition to research he was active in many other activities: he organized events for fellow graduate students; participate in and organized out-reach events like Ask an Astronomer LIVE! and Nerd Nite; and sung in choirs as well as karaoke. In January 2014, Carl took the next step in his journey by starting a postdoctoral research position at the Max Planck Institute for Astronomy in Heidelberg, Germany to expand his studies of high-z galaxies with Dr. Fabian Walter's research group.

This work is dedicated to my family, friends and the “Prof.”

ACKNOWLEDGMENTS

This dissertation is the result of many people both directly and indirectly. There are quite literally too many to mention, however, I will do my best to mention all who had an important impact on this work. First, I would like to acknowledge all of the support over the years from my family including my parents, Bill and Karen; sister, Jennifer, and most recently my brother-in-law, Michael, and nephews Auston and Wyitt, as well as my many extended family members who have sought updates to my academic journey over the years. Thank you to all of my friends for the nerdy discussions and support that have helped me be successful at the various stages of my journey. Thank you to my friends from high school (Adam, Will, Nate, Nick, Dave and Jerimiah), college (Jolene, Seth, Zach, Dan etc.), my Baltimore Students, my TFA family (Swift, Gordon, Stech, Abbie, etc.) and my Second Family (Jim, Cindy, Phil, Eloise). It was these last three groups who made my time Baltimore one I will cherish forever and helped me make the jump to graduate school.

At Cornell, I would like to acknowledge the contributions of the Submillimeter Astrophysics Group: Prof. Gordon Stacey for letting me spend a summer as an intern all of those years ago and all of the support since then; Thomas Nikola for all of your work on ZEUS-2, putting up with me for so much time on observing runs, and all of your insightful comments on my papers; Stephen Parshley without you, quite literally ZEUS-2 would never have become reality. Because of your work designing the mechanical, optical, and cryogenic systems of ZEUS-2 this thesis is as much a testament to your work as my own. Justin Shoenwald, thank you for your efforts getting the ZEUS-2 data acquisition systems in order.

There are many others at Cornell that also deserve mention. Chuck Henderson, I will always remember your wise words and our sailing adventure on Cayuga. Thank you to all of the

graduate students in and out of astronomy that I have come to know at Cornell: Steven Hailey-Dunsheath and Tom Oberst, thank you for your development of ZEUS-1, introducing me to TES and SQUIDs, and your input into the initial ZEUS-2 design; Drew Brisbin for all of your help in our initial explorations of SQUIDS, help on observing runs, and comments on my science. Oh and all the beer drinking too. Amit thank you for picking up where I left off and your work to realize ZEUS-2's full potential. Thank you to all of the grad students in my year (Betsey, Drew, Manolis, Shoshe) and especially to Dan, who put up with me in our apartment for 6 years. Lastly thank you to Matt, Amanda, Frances, Jason, Mark, Michael and all the others that helped ensure my time outside the lab was so much fun.

There are also many not at Cornell who contributed significantly to this work: Kent Irwin, Sherry Cho, and Mike Niemack at NIST made our detector arrays; Mark Halpern, Matthew Hasselfield, D.V. Wiebe, and Mandana Amiri developed and supported our use of the MCE; Dominic Benford and Johannes Staghun at Goddard Space Flight Center supported me through my NASA GSRP; Sarah Higdon and Jim Higdon at Georgia Southern University supported the MCE and observing runs; and finally,Peter Ade and Carol Tucker from Cardiff University who provided the filters for ZEUS-2. Last, but certainly not least, thanks to all of the staff at CSO and APEX. Your support really made this work possible.

This work has been funded via NSF grants AST – 0096881 and 0352855 for ZEUS-1, and 0705256, 0722220, 11105874 and 1109476 for ZEUS-2, as well as a NASA GSRP grant NNX10AM09H.

TABLE OF CONTENTS

LIST OF FIGURES

LIST OF TABLES

PREFACE: LOOKING BACK ON THE INFRARED UNIVERSE

Our understanding of the Universe has undergone a dramatic expansion over the past three decades. Advances in technology have opened new regimes of studies resulting in new and often surprising discoveries. Arguably the most well-known and the one with the largest impact has been the discovery of the accelerating expansion of the Universe and ΛCDM cosmology to explain it, i.e. the discovery of Dark Energy. It is amazing to consider that in 1996, my freshmen year of high school we had not yet discovered that regular matter only comprises ~4% of the total energy budget of the Universe.

The discovery of Dark Energy, while important, is still just one of the many groundbreaking discoveries made during the past thirty years that have changed the way humans view the Universe. In the 1980's the Infrared Astronomy Satellite (IRAS) discovered a significant population of galaxies emitting hundreds of times more light than the Milky Way galaxy, yet so dust enshrouded that nearly all of this emission was emitted at infrared wavelengths. Compared to these ultra-luminous infrared galaxies (ULIRG; $L_{IR} > 10^{12} L_{\odot}$), the Milky Way is quite modest, even insignificant in its properties. Additional observations across the electromagnetic spectrum eventually determined that nearby ULIRGs are produced through the merger two or more large galaxies. Moving ahead to the early 90's the Cosmic Origin Background Explorer (COBE) was launched to provided important details on the cosmic microwave background (CMB), but also measured the cosmic infrared background. This infrared background was unexpectedly equal to the total emission in the universe at visible wavelengths. Where does this infrared emission come from? At the time the numbers of nearby galaxies,

even including nearby ULIRGs, could only account for a small fraction of the observed infrared back ground.

In the late 90's new sensitive submillimeter and millimeter wave cameras were deployed and the survey's performed with these instruments, like SCUBA (the Submillimeter Common User Bolometer Array on the James Clerk Maxwell Telescope), resolved much of the far-infrared background into a population of infrared bright galaxies in the early universe. Many of these systems were observed to be undergoing extreme starbursts, producing hundreds to thousands of solar masses of stars per year so they will consume their supply of gas in only a few-hundred million years. Most surprising was discovering that these galaxies contain large quantities of dust that reprocesses the ultraviolet and optical light from stars into the observed infrared emission and suggest that galaxies even a few billion years after the Big Bang can have large quantities of dust. Ultimately the early submillimeter and millimeter surveys prompted many questions: Where did this dust come from? What is driving the high rates of star-formation? Do major mergers of two or more large galaxies, similar to local ULIRGs, power these extreme galaxies? Perhaps the accretion of gas via minor mergers or from the cosmic web can explain the properties of early galaxies? Continued advances in instrumentation are now allowing us to answer some of these outstanding questions from the previous submillimeter and millimeter surveys. Using the 1st-generation z (Redshift) and Early Universe Spectrometer (ZEUS-1) we began our own search for answers by studying the far-infrared fine-structure lines of high-z galaxies.

The far-IR fine-structure lines are powerful probes of the physical conditions of the interstellar medium (ISM) and arise in the ionized, atomic, and molecular phases of the ISM from the fine-structure levels of carbon, oxygen, nitrogen and their various ions. Transitions

between these fine-structure levels are quantum-mechanically forbidden, so that in most astrophysical environments collisional-excitation is typically responsible for placing the atom or ion in its excited state. In addition they are usually optically thin and weakly affected by extinction due to dust, as such the lines serve as important coolants of their respective phases of the ISM—in some cases they are the dominate coolants. These qualities can also make them excellent probes of both the density of the gas and source of gas heating. For instance the strength of the [CII] 158 μm line probes the strength of the FUV radiation field produced by stars that is responsible for heating the atomic gas in photo-dissociation regions. When compared to the far-IR emission of a galaxy, the line also constrains the size of the emission regions. The [OI] 63 μm line also arises in PDRs, but the [OI] emitting level has significantly higher critical density than the emitting level of [CII], so that the [OI] to [CII] line ratio measures the density of the gas. It is also possible to measure the hardness of the ionizing radiation field by comparing the relative strength of lines produced in different ionization states, such as the [OIII] 88 μm and [NII] 122 μm lines. For gas ionized by stars, measuring the hardness of the radiation of the field lets us determine the most massive star still on the main sequence.

The far-IR fine-structure emission lines begin falling into the submillimeter windows accessible from the ground for galaxies at $z \gtrsim 1$. ZEUS-1 was designed for detecting these lines in the short submillimeter windows at 350 and 450 μm. It featured an echelle-grating with resolving power (R~1000) to match to the broad lines of galaxies (~300 km/s) and background limited detectors resulting in excellent line-detection sensitivity. Using ZEUS-1 on the Caltech Submillimeter Observatory we made the first survey of the [CII] 158 μm line at high-z and the first detections of the [OIII] 88 μm and [NII] 122 μm from galaxies in the early universe. Building on this success we built the 2nd-generation z(Redshift) and Early Universe Spectrometer

(ZEUS-2) to continue and expand on the work begun with ZEUS-1.

The work covered in this dissertation includes the ZEUS-1 detections of the [OIII] and [NII] lines, the first science result of ZEUS-2 and lastly the design and performance of ZEUS-2. Chapters 1 and 2 discuss the first detection of the [OIII] 88 μm and [NII] 122 μm lines from high-redshift galaxies. Both chapters appeared in the Astrophysical Journal Letters as Ferkinhoff et al. 2010 and Ferkinhoff et al. 2011 respectively. Chapter 3 discusses the [CII] 158 μm line and the first light detection of this line with the ZEUS-2 on the Atacama Pathfinder EXperiment. This chapter has appeared in the Astrophysical Journal as Ferkinhoff et al. 2014. Lastly, Chapter 4 (to be submitted to the Astrophysical Journal) covers the details on the design and performance of ZEUS-2. In total this dissertation demonstrates the methods and instruments we can use to find answers to the many yet unanswered questions about early galaxies.

CHAPTER 1

FIRST DETECTION OF THE [OIII] 88 μm LINE AT HIGH REDSHIFTS: CHARACTERIZING THE STARBURST AND NARROW LINE REGIONS IN EXTREME LUMINOSITY SYSTEMS

We have made the first detections of the 88 μm [OIII] line from galaxies in the early Universe, detecting the line from the lensed AGN/starburst composite systems APM 08279+5255 at z = 3.911 and SMM J02399-0136 at z = 2.8076. The line is exceptionally bright from both systems, with apparent (lensed) luminosities ~10^{11} $L_{\odot}$. For APM 08279, the [OIII] line flux can be modeled in a star formation paradigm, with the stellar radiation field dominated by stars with effective temperatures, T_{eff} >36,000 K, similar to the starburst found in M82. The model implies ~35% of the total far-IR luminosity of the system is generated by the starburst, with the remainder arising from dust heated by the AGN. The 88 μm line can also be generated in the narrow line region of the AGN if gas densities are around a few 1000 cm^{-3}. For SMM J02399 the [OIII] line likely arises from HII regions formed by hot (T_{eff} >40,000 K) young stars in a massive starburst that dominates the far-IR luminosity of the system. The present work demonstrates the utility of the [OIII] line for characterizing starbursts and AGN within galaxies in the early Universe. These are the first detections of this astrophysically important line from galaxies beyond a redshift of 0.05.

1 INTRODUCTION

The 88 μm [OIII] line is one of eight bright far-infrared fine-structure lines that emerge from electronic ground state configurations of the astrophysically abundant atoms C^+ (158 μm), N^+ (122 & 205 μm), N^{++}(57 μm), O^0 (63 & 146 μm), and O^{++} (88 & 52 μm). These lines are major or even dominant coolants for much of the interstellar medium in dusty star-forming galaxies, and excellent extinction-free probes of the physical conditions of the gas, and/or the strength or hardness of the ambient interstellar radiation fields. Far-IR extragalactic spectral line surveys obtained with the Infrared Space Observatory (ISO) (Malhotra et al. 2001, Negishi et al. 2001, Brauher et al. 2008) detected many of these lines in >200 nearby galaxies. At least 88 galaxies were observed in the [OIII] 88 μm line, with a detection rate near 75%. The [OIII] line was typically the second or third most luminous line (after the [CII] and [OI] 63 μm lines), and in ~10% of the galaxies it was the most luminous far-IR line. The [OIII] line to far-IR continuum luminosity ratio ranges from 0.03 to 2%, with a median value ~ 0.15%.

To form O^{++} takes 35 eV photons so that hot (T_{eff} > 36,000 K) stars are required for strong [OIII] line emission. Since the [OIII] 88 μm line emitting level is only 164 K above ground, and has a critical density ~ 510 cm^{-3}, the line emission is insensitive to ionized gas temperature, and typically traces moderate density (~ 100 cm^{-3}) clouds. Oxygen is often doubly ionized near AGN, and indeed, the forbidden optical lines of O^{++} (e.g. [OIII] 5007 Å) are among the brightest optical lines from the narrow line regions (NLR) excited by AGN.

We report the first detections of the [OIII] 88 μm line from a galaxy beyond a redshift of ~ 0.05. We strongly (7.0σ) detected the line from the highly lensed (μ ~ 4 to 90, Riechers et al 2009, Egami et al. 2000) broad absorption line (BAL) quasar APM 08279+5255 (hereafter APM

08279) at z = 3.911, and made a weaker (4.1σ) detection of the line from the more moderately lensed (μ ~ 2.38, Ivison et al. 2010) submillimeter galaxy, SMM J02399-0136 (hereafter SMM J02399) at z=2.8076.

APM 08279 is a composite AGN/starburst system with an *apparent* bolometric luminosity[1] ~ 7×10^{15} $L_{\odot}$, of which 2×10^{14} $L_{\odot}$ emerges in the rest-frame FIR bands (Weiss et al. 2007). Dividing by the largest magnification advocated the luminosity of the system is still ~ 8×10^{13} $L_{\odot}$, making it both the system with the largest apparent luminosity known, and an intrinsically extremely luminous system. The strong lensing enables detection and imaging of the source in at least 6 CO rotational transitions, which arise from a disk-like structure with lensed radius ~ 900 pc containing ~ 5.3×10^{11} μ^{-1} $M_{\odot}$ of molecular gas (Riechers et al. 2009). Through detailed modeling of the far-infrared through radio continuum SED, Riechers et al. (2009) conclude that the dominant heating source for the system is the AGN.

SMM J02399 is also a composite AGN/starburst system. It was the first submillimeter galaxy discovered (Ivison et al. 1998), and the first to be detected in a rotational line of CO (Frayer et al. 1998). The molecular gas mass is quite large (~ 2.38×10^{11} μ^{-1} $M_{\odot}$, Ivison et al. 2010) as is the far-IR luminosity ($L_{far\text{-}IR}$ ~ 2.9×10^{13} μ^{-1} $L_{\odot}$, Frayer et al. 1998). The system has at least four distinct components within a 3" diameter region. Initial ground based BVR band imaging revealed two sources: L1, a weak BAL quasar, and L2, a wispy region stretching ~ 3" to the east of L1 (Ivison et al. 1998). Later HST imaging revealed two additional faint, extended (~0.5 to 1") components within the system, labeled L2SW and L1N (Ivison et al. 2010). Based on precise registration between VLA 1.6 GHz, and EVLA CO(1-0) mapping, Ivison et al. 2010 make a strong case that the source of most of the far-IR luminosity is neither L1 nor L2, but

rather from L2SW, located roughly between L1 and L2. L2SW has extremely red IRAC colors, and its coincidence with the molecular gas and rest-frame 333 μm continuum emission (centroid adjusted from Genzel et al. 2003) indicates that L2SW is the site of an extreme luminosity, very young starburst that likely dominates the far-IR luminosity of the system.

2 OBSERVATIONS

We employed the redshift (z) and Early Universe Spectrometer (ZEUS, Stacey et al. 2004, Hailey-Dunsheath 2009) on the Caltech Submillimeter Observatory (CSO)[2] for our observations. ZEUS is an echelle grating spectrometer that employs a linear 1 × 32 pixel bolometer array oriented along the dispersion direction that delivers background limited R ~ 1000 spectroscopy in both the 350 and 450 μm telluric windows. Band-pass filters enable half the array to operate in 5^{th} order (350 μm band) of the echelle, and the other in 4^{th} order (450 μm band) of the echelle so that we obtain simultaneous spectra in the two bands for a single beam on the sky. For APM 08279 (SMM J02399) at redshift of 3.911 (2.8076), the 88.356 μm line is redshifted to 433.916 μm (336.424 μm), and the pixel spacing (~ one resolution element) corresponds to 278 (321) km/sec. For both bands, the near diffraction limited ZEUS/CSO beam is ~11" full-width-at-half-maximum, determined by observations of Uranus. At the observed wavelengths, ZEUS achieves sensitivity equivalent to a single-side-band receiver temperature < 50 K. Data were taken in standard chop/nod mode with a chop frequency of 2 Hz and amplitude of 30". Spectral response flats were obtained on a cold load, and point-source coupling and calibration (estimated at ± 30%) was obtained through observations of Uranus (T_{Uranus} =63 and 71 K at 336 and 434 μm respectively, Hildebrand et al. 1985). On 14 March 2009 we made a 4.5σ detection of the line

[1] We assume a flat cosmology, $\Omega_\Lambda = 0.73$, $H_0 = 71$ km/sec/Mpc throughout this paper.

from APM 08279. This was confirmed at 7σ significance on 1 December 2009 in 77 minutes of on-source integration time with line-of-sight (l.o.s) transmission ~37%. The final spectrum (Figure 1) is this second, high significance integration. We detected (4.1σ) the line from SMM J02399 on 15 January 2010 in 77 minutes of on-source integration time with l.o.s. transmission ~ 23% (Figure 2).

3 RESULTS

3.1 *Line Luminosity*

Table 1 lists the source line fluxes and apparent luminosities. The line is extremely bright ~ 10^{11} μ^{-1} $L_{\odot}$ in both sources. For APM 08279, the [OIII] to far-IR continuum luminosity ratio is ~ 5.3×10^{-4}, and for SMM J02399 it is ~ 3.6×10^{-3}, so that the ratio is ~3 times smaller than the typical value in the ISO surveys for APM 08279, and ~2 times larger for SMM J02399. For both sources, the line is clearly narrow (< 400 to 600 km/sec), so that the line does not arise from broad-line region gas, and therefore either arises from the narrow line region of the AGN or from star formation regions within the system.

With APM 08279, we detected (12σ) the 434 μm continuum at ~ 348 ± 104 mJy, in very good agreement with the 450 μm SHARC-2 value (342 ± 26 mJy, Beelen et al. 2006) From SMM J02399 the 336 μm continuum was weakly (4σ) detected at ~ 133 ± 39 mJy. Extrapolating from the 450 μm SCUBA flux (69 mJy) using the dust temperature (45 K) and emissivity index (1.5) typical of luminous IRAS galaxies (Dunne et al. 2000), we predict a 336 μm continuum from SMM J02399 of ~ 98 mJy, in good agreement with our observed value.

---

[2] The Caltech Submillimeter Observatory is supported by NSF contract AST-0229008

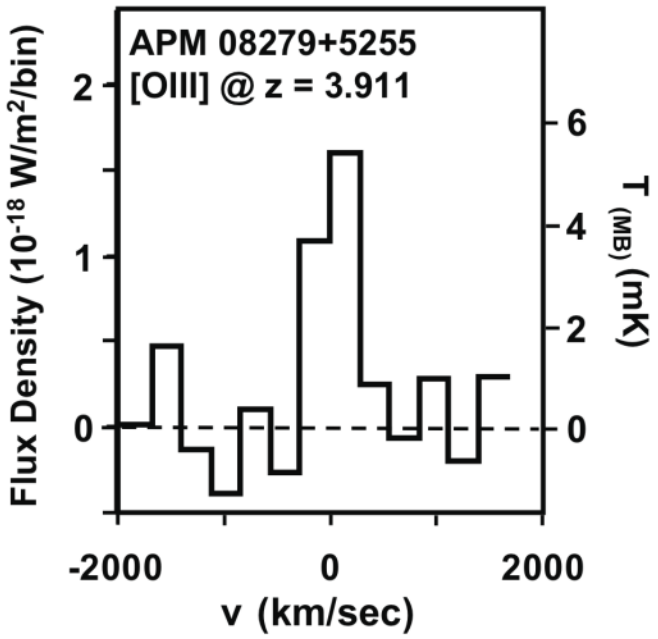

Figure 1: ZEUS/CSO detection of the [OIII] 88 μm line from APM 08279+5255. Velocity is referenced to z=3.911. The continuum emission has been subtracted off.

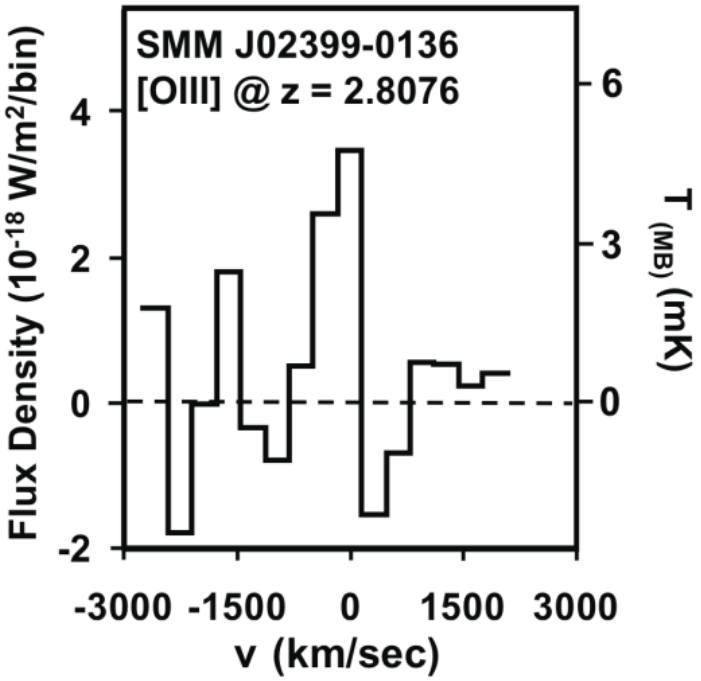

Figure 2: ZEUS/CSO detection of the [OIII] 88 μm line from SMM J02399-0136. Velocity is referenced to z=2.8076. The continuum emission has been subtracted off.

Table 1: Source Parameters

Source	RA (J2000)	Dec (J2000)	z	D_L (Gpc)	$L_{far\text{-}IR}$ ($L_\odot$)	F([OIII]) (10^{-18} W/m^2)[1]	L([OIII]) ($L_\odot$)
SMM J02399	$02^h\,39^m\,51.9^s$	-01°35'59"	2.8076	23.8	2.9E13[2]	6.04 ± 1.46	1.06E11
APM 08279	$08^h\,31^m\,41.6^s$	52°45'17"	3.911	35.6	2.0E14[3]	2.68 ± 0.38	1.05E11

[1]Statistical uncertainties only. Calibration uncertainties are ~ 30%.
[2]Weiss et al. 2007,
[3]Frayer et al. 1998.

3.2 *Minimum Mass of Ionized Gas.*

Without knowledge of the gas density, one may only rigorously calculate a *minimum ionized gas mass* required to support the observed [OIII] line emission. The minimum mass is obtained for the high density, high temperature limit, assuming all the oxygen is in the state O^{++} for the entire HII region. This latter assumption is realistic only for nebula created by very hot (T_{eff} >40,000 K) stars. Under such simplifications, the 88 μm line flux, F([OIII]) is related to the minimum mass, $M_{min}(H^+)$ by:

$$M_{min}(H^+) = F([OIII]) \frac{4\pi\, {D_L}^2}{\frac{g_1}{g_t} A_{10} h\nu_{10}} \frac{m_H}{\chi(O^{++})}, \qquad (1)$$

where A_{10}, and g_l, are the Einstein A coefficient, and statistical weight (=3), for the (J=1) 88 μm photon emitting level, $g_t = \Sigma g_i \exp(-\Delta E_i/kT)$ is the partition function, h is Planck's constant, ν_{10} is 88 μm line frequency, D_L is the source luminosity distance, and $\chi(O^{++})$ is the relative abundance of O^{++}/H^+ within the HII region, which, for minimum mass = O/H. Assuming "HII region" gas phase oxygen abundance ($O/H = 5.9 \times 10^{-4}$, Savage and Sembach, 2004) for both APM 08279 and SMM J02399 we have $M_{min}(H^+) \sim 3.0 \times 10^9\ \mu^{-1}\ M_\odot$, ~ 1% of the apparent molecular gas mass in these systems. For both systems, the minimum ionized gas/molecular mass fraction is small compared with that of the nearby starburst galaxy M82 (~ 12%, Lord et al. 1996, Wild et al. 1992). Note that the ionized gas mass is inversely proportional to the O/H ratio, and a strong function of the effective temperature of the ionizing stars. If, for example, the HII region is formed by stars with T_{eff} ~ 36,000 K, then only ~ 14% of the oxygen within the HII region is in the form O^{++}, so the ionized gas mass is 7 times larger than the value given above.

4 DISCUSSION: GAS EXCIATION MECHANISMS

The ionization source for the observed [OIII] line emission can be either UV photons from early type stars, or from the AGN. Both sources are viable for APM 08279, while for SMM J02399 we prefer a star formation model.

4.1 *APM 08279*

4.1.1 *The Ionization State of the Gas.*

Very few lines useful for estimating the ionization state of the gas have been detected from APM 08279. However, an upper limit to the 205 μm [NII] line is available (Krips et al. 2007), and this limit can provide a good constraint. Due to their similar ionization potentials, when O is in the form O++, N will be in the form N++. Therefore, the [NII] 205 μm to [OIII] 88 μm line ratio is very sensitive to the hardness of the local radiation fields. Krips et al (2007) give a 3σ upper limit of 9 Jy-km s^{-1} $beam^{-1}$ for the [NII] line within 1000 km/sec of the line center. Integrating over their map, and assuming the [NII] morphology matches the 200 μm continuum morphology, the upper limit scales to ~16 Jy-km s^{-1}, or 1.56×10^{-19} W m^{-2}. Therefore the [OIII] 88 μm/[NII] 205 μm line flux ratio is greater than 17.

4.1.2 *Stars as the Energy Source.*

Rubin (1985) calculates the expected far-IR line intensities for HII regions as a function of gas density, elemental abundances, and stellar effective temperature. We use the "K" model abundances (O/H = 6.76×10^{-4}, N/H = 1.15×10^{-4}), close to the "HII region" values given by Savage and Sembach (2004), since the dust to gas ratio (reflecting metalicity) appears near the Milky Way value for APM 08279 (Riechers et al. 2009). The lower limit on the [OIII]/[NII] line ratio imposes a strong lower limit of T_{eff} > 36,000 K (O9V stars, Vacca et al. 1996). The gas

density must be > few cm^{-3} if we assume the ionized gas mass is less than the molecular gas mass, and < 10,000 cm^{-3} if we assume that the luminosity of the ionizing stars is less than or equal to the far-IR luminosity of the system. Taking densities between 100 and 1000 cm^{-3} which are typical of starburst regions, and using "K49" models (10^{49} ionizing photons s^{-1} HII region^{-1}), the total gas mass traced by the [OIII] 88 μm line is ~ 4.3×10^{10} μ^{-1} $M_\odot$ if the HII regions are formed by stars with T_{eff} = 36,000 K, and 3-8 × 10^9 μ^{-1} $M_\odot$ if they are formed by hotter (T_{eff} = 40,000 K) stars. The ionized gas is therefore between 0.6 - 8% of the molecular gas mass. The total ionization requirement is equivalent to 3 – 30 ×10^8 μ^{-1} O9V or 3 – 10 × 10^7 μ^{-1} O7.5V stars (T_{eff} = 36,000, and 40,000 K respectively, Vacca et al. 1996). These ionizing stars generate a total luminosity of 4 – 40 × 10^{13} μ^{-1} $L_\odot$, and 6 – 20 × 10^{12} μ^{-1} $L_\odot$ for the O9V and O7.5V solutions respectively. The lower metalicity (O/H = 1.27×10^{-4}, N/H = 1.47×10^{-4}) "D49" models of Rubin (1985) yield the same constraints on ionization, but require about five times the ionized gas-mass and three times the number of ionizing stars.

For a starburst model, it is instructive to compare the physical conditions of the starburst in APM 08279 to that occurring in nearby, well studied, and resolved systems such as M82. A comprehensive description of the excitation of the ISM in M82 has emerged from far-IR line studies. The ionized gas component in M82 is well fit by a collection of 60,000 ionization-bounded HII regions, with n_e ~ 180 cm^{-3}, each photo-ionized by a single star generating 10^{49} ionizing photons (Lord et al.1996). The starburst is fueled by a concentration of 8 × 10^8 $M_\odot$ of molecular gas (Wild et al. 1992). Colbert et al. (1999) model the current day stellar population as having evolved from an instantaneous starburst that occurred 2 – 3 Myr ago and was topped by 100 $M_\odot$ stars. This population generates a total stellar luminosity of 3 – 5 × 10^{10} $L_\odot$, consistent with the observed M82 far-IR luminosity, L_{FIR} ~ 2.3×10^{10} $L_\odot$ (Rice et al 1988).

Unfortunately, common star formation tracers like the hydrogen recombination lines and the PAH features, are not useful for a comparison between M82 and APM 08279. The Hα, Paα, and Paβ lines were observed with Spitzer/IRS and AKARI spectrometers, but since the line widths are ~ 9000 km/sec, and the line fluxes are variable, they clearly arise from the broadline regions of the AGN (Soifer et al. 2004, Oyabu et al. 2009). Relative to the [OIII] 88 μm line, these lines are ~100 times more luminous in APM 08279 than in M82, and so we make no attempt to isolate the narrow component that may be produced in star-forming regions. The Spitzer 6.2 μm PAH feature upper limit (2.3×10^{-17} W m^{-2}, Soifer et al. 2004) is ten times our [OIII] flux. The 6.2 μm PAH/[CII] line ratio is ~ 3:1 for star forming galaxies (Luhman et al. 2003), and the [CII]/[OIII] ratio increases to ~ 1:3 for warmer dust galaxies, so that for luminous star forming galaxies one expects a 6.2 μm PAH/[OIII] 88 μm line ratio near unity. Therefore, the Spitzer upper limit does not constrain our models.

An examination of the [OIII] luminosity, far-IR luminosity, and the molecular gas mass of APM 08279 (Table 2) indicates that these tracers are well matched by a superposition of ~3000 μ^{-1} M82 like starbursts if about 1/3 to 1/2 of the far-IR radiation observed from APM 08279 is attributed to that starburst. The remainder of the far-IR flux would arise from AGN heated dust, which is consistent with the higher dust temperature of APM 08279 (65K, Weiss et al. 2007) as compared to that of M82 (48K, Colbert et al. 1999; 50K, Negishi et al. 2001). If the stellar population is similar to that modeled for M82 (Colbert et al., 1999), then we require the equivalent of 5×10^8 μ^{-1} O9V stars and their associated lower mass brethren to heat the dust providing a far-IR luminosity ~ 6.9×10^{13} μ^{-1} $L_\odot$. For this case, the HII regions would have gas densities similar to that of M82, n_e ~ 180 cm^{-3}. The far-IR luminosity due to star formation is equivalent to a star formation rate of 12,000 μ^{-1} $M_\odot$ yr^{-1} using the Kennicutt (1998) law.

Table 2: Comparison Between APM 08279 and M82

	[OIII] 88 μm Luminosity ($L_\odot$)	H_α Luminosity ($L_\odot$)	Far-IR Luminosity ($L_\odot$)	Molecular Gas Mass ($M_\odot$)	[OIII]/Far-IR	[OIII] 88 μm/ [NII] 205 μm
APM 08279	1.05E11[2]	1.26E13[4]	2.0E14[6]	5.3E11[8]	5.3E-4	> 17
M82	3.5E7[1]	1.8E7[3]	2.3 – 3.2 E10[5,1]	1.8E8[7]	1.1 – 1.5E-3	15.5[9]
APM/M82 ratio	3060	682000	6300 – 8700	3000	0.35 – 0.48	--

Notes: [1]Colbert et al. 1999, [2]Present work, [3]McLeod et al. 1993, [4]Oyabu et al. 2009, [5]Rice et al. 1988, [6]Beelen et al. 2006, Weiss et al. 2007, [7]Wild et al. 1992, [8]Riechers et al. 2009,
[9]Lord et al. 1996, Watson et al. 1984

4.1.3 *The AGN as the Energy Source*

It is difficult to quantify the importance of [OIII] line emission from NLR clouds, as these clouds may imitate star forming clouds both in line profile and ionized gas densities. However, by simple scaling arguments we show that emission from these regions of APM 08279 may be important. NLRs have typical gas densities ~ 100 – 10,000 cm^{-3}, with "average" values near 2000 cm^{-3} (Peterson 1997). In this density range the [OIII] 5007 Å/[OIII] 88 μm line intensity ratio varies from ~0.3 (3) to 65 (180) for "K" ("D") models (Rubin 1985). Observationally, the luminosity of the [OIII] 5007 Å line from AGN is related to the bolometric luminosity of the AGN by $L_{5007}=L_{bol}/3500$, where L_{5007} is the observed luminosity of the [OIII] 5007Å line, uncorrected for extinction (Kauffmann & Heckman, 2005). Since L_{bol} for APM is ~ $7 \times 10^{15}\ \mu^{-1}$ $L_{\odot}$, the scaling argument suggests $L_{5007} \sim 2 \times 10^{12}\ \mu^{-1}\ L_{\odot}$, so that the expected luminosity of the 88 μm line is between $1 \times 10^{10}\ \mu^{-1}$ and $6 \times 10^{12}\ \mu^{-1}\ L_{\odot}$, depending on gas density and abundances. The observed 88 μm line luminosity ($1.05 \times 10^{11}\ \mu^{-1}\ L_{\odot}$) may arise solely from the NLR of the AGN if this scaling law holds, and if the gas density is ~2000 (1000) cm^{-3}, for the "K" ("D") models. The 88 μm line is too weak to support smaller gas density models, and for higher gas densities, only a fraction of the 88 μm line arises from the NLR.

4.2 *SMM J02399*

Ivison et al. 2010 argue that most of the far-IR luminosity in SMM J02399 is due to a massive starburst centered on the source L2SW. Furthermore, since the 6.2 μm PAH flux (~5×10^{-18} W m^{-2}, Lutz et al. 2005), is roughly that of the [OIII] 88 μm line, as expected for star forming galaxies, we construct a model within a starburst paradigm. Ivison et al. (1998) detected the [OIII] 5007 Å line (blended with the [OIII] 4959 Å line) and the Hα line (blended with the [NII] 6548 Å line) from L1 and L2 in the SMM J02399 system. The 5007Å line is exceptionally

bright, especially from L2, where within the 1.5" beam, correcting for the expected 3:1 5007Å/4959Å line blending ratio, the 5007Å line flux is 1.5×10^{-17} W m^{-2} (2.7×10^{-11} μ^{-1} $L_{\odot}$). SMM J02399 was not mapped in these lines, but Ivison et al. (2010) mapped the system in Lyα. Assuming the [OIII] and Hα fluxes scale as the Lyα flux we estimate the total [OIII] 5007 Å and Hα line emission from the source is ~2.9 and ~1.9×10^{-17} W m^{-2} respectively. The [OIII] 5007 Å/Hα ratio (=1.5) is very sensitive to the relative fractions of photons capable of forming O^{++} and H^{+} (effective stellar temperature), while the [OIII] 5007 Å/88 μm line flux ratio (=4.8) is sensitive to gas density and the electron temperature within the HII region. Good fits to the observed line ratios and absolute fluxes are obtained for T_{eff} = 40,000 K (O7.5 stars), and gas densities of 100, or 1000 cm^{-3}, if one uses the low ("D") or Galactic ("K") metalicities in the Rubin (1985) models respectively. The metalicity and density solutions are degenerate since lower metalicity HII regions have higher electron temperatures, the effect of which is to increase the [OIII] 5007 Å/88 μm line flux ratio at a given density. Correction for extinction effects on the optical lines increases their flux, raising the requisite gas density by factors roughly equal to the extinction correction factor. The requisite ionized gas mass is ~ $3.3 – 30 \times 10^{9}$ μ^{-1} $M_{\odot}$, where the lower value is for "K" metalicities. For both cases, the ionizing flux is equivalent to that of 1.0×10^{8} μ^{-1} O7.5 stars. The absorption of the full luminosity of these stars by dust would account for ~75% of the observed far-IR luminosity of the system. The inferred star formation rate is ~5000 μ^{-1} $M_{\odot}$ yr^{-1} using the Kennicutt (1998) scaling law.

5 SUMMARY AND OUTLOOK

We have made the first detections of the [OIII] 88 μm line from galaxies in the early Universe. The line can trace either young stars or the NLR near AGN. The observed 88 μm line

emission from APM 08279 can arise from a starburst whose hottest stars have T_{eff} > 36,000 K, or from the NLR of the AGN. From SMM J02399 the 88 μm line is modeled as arising from a massive starburst dominated by very early type (T_{eff} > 40,000 K) stars most likely located near the extended source, L2SW. To further constrain the physical properties of the emitting gas requires additional extinction-free spectral line probes. For example, gas density is constrained with the detection of the [OIII] 52 μm line. The density-sensitive 52 μm/88 μm [OIII] line intensity ratio is ~0.7 for low density clouds rapidly growing to the saturation value of 10 at densities above 10,000 cm^{-3}. Unfortunately, for both sources, the 52 μm lines are redshifted into regions of the far-IR/submm bands that are totally blocked by Earth's atmosphere. However, the expected line fluxes (~2 to 60 × 10^{-18} W m^{-2}) are within reach of the Herschel SPIRE spectrometer in 1 to 40 hours of integration time, so that Herschel SPIRE observations should provide important density constraints on our models. It is also likely that the [OIV] 26 μm line will be detectable from these systems with the Herschel PACS spectrometer. The [OIV]/[OIII] line ratio is a sensitive near extinction-free indicator of the hardness of the ambient radiations fields, and will strongly distinguish a starburst from AGN origin for the extreme far-IR luminosity from these two systems.

This work was supported by NSF grants AST-0096881, AST-0352855, AST-0705256, and AST-0722220, and by NASA grants NGT5-50470 and NNG05GK70H. We thank our colleagues T.L. Herter and H. Spoon for useful discussion, and the CSO staff for their excellent support of ZEUS operations.

REFERENCES

Beelen, A., Cox, P., Benford, D. J., Dowell, C. D., Kovacs, A., Bertoldi, F., Omont, A., & Carilli, C. L. 2006, ApJ, 642, 694

Brauher, J. R., Dale, D. A., & Helou, G. 2008, ApJS, 178, 280

Colbert, J. W., et al. 1999, ApJ, 511, 721

Dunne, L., Eales, S., Edmunds, M., Ivison, R., Alexander, P., & Clements, D. L. 2000, MNRAS, 315, 115, L151

Egami, E., Neugebauer, G., Soifer, B. T., Matthews, K., Ressler, M., Becklin, E. E., Murphy, T. W., Jr., & Dale, D. A. 2000, ApJ, 535, 561

Frayer, D. T., Ivison, R. J., Scoville, N. Z., Yun, M., Evans, A. S., Smail, I., Blain, A. W., & Kneib, J.-P. 1998, ApJ, 506, L7

Genzel, R., Baker, A. J., Tacconi, L. J., Lutz, D., Cox, P., Guilloteau, S., & Omont, A. 2003, ApJ, 584, 633

Hailey-Dunsheath, S. 2009, PhD thesis, Cornell University

Hildebrand, R. H., Loewenstein, R. F., Harper, D. A., Orton, G. S., Keene, J., & Whitcomb, S. E. 1985, Icarus, 64, 64

Ivison, R. J., Smail, I., Le Borgne, J.-F., Blain, A. W., Kneib, J.-P., Bezecourt, J., Kerr, T. H., & Davies, J. K. 1998, MNRAS, 298, 583

Ivison, R. J., Smail, I., Papadopoulos, P. P., Wold, I., Richard, J., Swinbank, A. M., Kneib, J.-P., & Owen, F. N. 2010, MNRAS, 261

Kauffmann, G., & Heckman, T. M. 2005, Phil. Trans. R. Soc. A, 363, 621

Kennicutt, R. C., Jr. 1998, ARA&A, 36, 189

Krips, M., Peck, A. B., Sakamoto, K., Petitpas, G. B., Wilner, D. J., Matsushita, S., & Iono, D. 2007, ApJ, 671, L5

Lord, S. D., Hollenbach, D. J., Haas, M. R., Rubin, R. H., Colgan, S. W. J., & Erickson, E. F. 1996, ApJ, 465, 703

Luhman, M. L., Satyapal, S., Fischer, J., Wolfire, M. G., Sturm, E., Dudley, C. C., Lutz, D., & Genzel, R. 2003, ApJ, 594, 758

Lutz, D., Valiante, E., Sturm, E., Genzel, R., Tacconi, L. J., Lehnert, M. D., Sternberg, A., & Baker, A. J. 2005, ApJ, 625, L83

Malhotra, S., et al. 2001, ApJ, 561, 766

McLeod, K. K., Rieke, G. H., Rieke, M. J., & Kelly, D. M. 1993, ApJ, 412, 111

Negishi, T., Onaku, T., Chan, K.-W., & Roellig, T. L. 2001, A&A, 375, 566

Oyabu, S., Kawara, K., Tsuzuki, Y., Matsuoka, Y., Sameshima, H., Asami, N., & Ohyama, Y. 2009, ApJ, 697, 492

Peterson, B. M. 1997, An Introduction to Active Galactic Nuclei (Cambridge: Cambridge Univ. Press)

Rice, W., Lonsdale, C. J., Soifer, B. T., Neugebauer, G., Kopan, E. L., Lloyd, L. A., de Jong, T., & Habing, H. J. 1988, ApJS, 68, 91

Riechers, D. A., Walter, F., Carilli, C. L., & Lewis, G. F. 2009, ApJ, 690, 463

Rubin, R. H. 1985, ApJS, 57, 349

Savage, B. D., & Sembach, K. R. 1996, ARA&A, 34, 279

Soifer, B. T., et al. 2004, ApJS, 154, 151

Stacey, G. J., et al. 2007, in ASP Conf. Ser. 375, From Z-Machines to ALMA: (Sub)Millimeter Spectroscopy of Galaxies, ed. A. J. Baker et al. (San Francisco, CA: ASP), 52

Vacca, W. D., Garmany, C. D., & Shull, J. M. 1996, ApJ, 460, 914

Watson, D. M., Genzel, R., Townes, C. H., Werner, M. W., & Storey, J. W. V. 1984, ApJ, 279, L1

Weiß, A., et al. 2007, A&A, 467, 955

Wild, W., Harris, A. I., Eckart, A., Genzel, R., Graf, U. U., Jackson, J., Russell, A. P. G., & Stutzki, J. 1992, A&A, 265, 447

CHAPTER 2

FIRST DETECTIONS OF THE [NII] 122 μm LINE AT HIGH REDSHIFT: DEMONSTRATING THE UTILITY OF THE LINE FOR STUDYING GALAXIES IN THE EARLY UNIVERSE.

We report the first detections of the [NII] 122 μm line from a high redshift galaxy. The line was strongly (> 6σ) detected from SMMJ02399-0136, and H1413+117 (the Cloverleaf QSO) using the Redshift(z) and Early Universe Spectrometer (ZEUS) on the CSO. The lines from both sources are quite bright with line-to-FIR continuum luminosity ratios that are ~7.0×10^{-4} (Cloverleaf) and 2.1×10^{-3} (SMMJ02399). With ratios 2-10 times larger than the average value for nearby galaxies, neither source exhibits the line-to-continuum deficits seen in nearby sources. The line strengths also indicate large ionized gas fractions, ~8 to 17% of the molecular gas mass. The [OIII]/[NII] line ratio is very sensitive to the effective temperature of ionizing stars and the ionization parameter for emission arising in the narrow-line region (NLR) of an AGN. Using our previous detection of the [OIII] 88 μm line, the [OIII]/[NII] line ratio for SMMJ02399-0136 indicates the dominant source of the line emission is either stellar HII regions ionized by O9.5 stars, or the NLR of the AGN with ionization parameter log(U) = -3.3 to -4.0. A composite system, where 30 to 50% of the FIR lines arise in the NLR also matches the data. The Cloverleaf is best modeled by a superposition of ~200 M82 like starbursts accounting for all of the FIR emission and 43% of the [NII] line. The remainder may come from the NLR. This work demonstrates the utility of the [NII] and [OIII] lines in constraining properties of the ionized medium.

1 INTRODUCTION

The far-infrared (FIR) fine-structure lines from carbon, nitrogen, oxygen and their ions serve as important and in some cases dominant coolants of major phases of the interstellar medium (ISM). In the 80's, 90's, and first decade of the new century much work was done characterizing these lines in the Milky Way and nearby galaxies (e.g Stacey et al. 1991, Wright et al. 1991, Malhotra et al. 2001, Luhman et al. 2003, Brauher et al. 2008, and Fisher et al. 2010). The advent of a new generation of sensitive ground and spaced based submillimeter instruments (e.g. ZEUS, Z-Spec and Herschel-SPIRE) is now enabling the study of these lines to move beyond the local Universe. Lines like the [CII] 158 μm, [OIII] 88 and 52 μm, and now the [NII] 122 μm line, redshifted into the submillimeter bands, are providing important details on the physical conditions and excitation of gas in these early galaxies (e.g. Maiolino et al. 2005, Maiolino et al. 2009, Hailey-Dunsheath et al. 2010, Sturm et al. 2010, Ivison et al. 2010a, Stacey et al. 2010, Ferkinhoff et al. 2010, and Valtchanov et al. 2011), essential to our understanding of the star formation process during the peak epoch of star formation, z ~ 1 to 3 (Hopkins & Beacom 2006). Here we report the detection of the [NII] 122 μm line from SMMJ02399-0136 (hereafter SMMJ02399) at z = 2.81 and H1413+117(the Cloverleaf QSO) at z = 2.56. These detections are the first reported detection of this line from a galaxy at z > 0.09.

Nitrogen requires 14.5 eV photons for single ionization, so that N^+ resides predominantly in HII regions formed by late O or early B type stars. The ground state term of N^+ is split into three levels leading to the 122 μm ($^3P_2 - {}^3P_1$), and 205 μm ($^3P_1 - {}^3P_0$) fine structure lines. Because the lines are collisionally populated, optically thin, and insensitive to gas temperature their line intensity yields a minimum ionized-gas mass and the minimum numbers of photons capable of maintaining the ionization equilibrium for the species. For the [NII] lines this means photons

between $14.5 < h\nu < 30$ eV and spectral types between B2 and O8 stars[3].

Comparing the line flux of [NII] to [OIII] provides a very sensitive probe of UV field hardness since 35 eV photons are needed to form O^{++}. Furthermore, because the [OIII] 88 μm and [NII] 122 μm emitting levels have similar critical densities for thermalization (510 cm^{-3}, and 310 cm^{-3} respectively), the line ratio is very insensitive to gas density. This means that for stellar radiation fields the line ratio constrains the most luminous star on the main sequence and hence the age of the stellar population (Figure 1, bottom axis). These lines also arise from the narrow line region (NLR) of active galactic nuclei (AGN), in which case the ratio is a sensitive indicator of the ionization parameter, U, of the NLR—defined by the ratio of ionizing photons to number density of the gas (Abel et al. 2009).

SMMJ02399 was the first submillimeter-selected galaxy (Ivison et al 1998). Lensed by a factor $\mu \sim 2.38$ (Ivison et al 2010b, hereafter I10b), it still has a very large intrinsic FIR luminosity[4], $L_{FIR} \sim 1.22 \times 10^{13} L_{\odot}$ (Frayer et al 1998) and molecular gas content, $M(H_2) \sim 1 \times 10^{11} M_{\odot}$ (I10b). SMMJ02399 is a composite AGN/starburst system that contains 4 distinct components within ~ 3" radius in the sky-plane. Initial BVR imaging identified two components: L1, associated with the broad-absorption-line quasar (BAL); and L2, which exhibits very blue emission extending ~ 3" to the east of L1 (Ivison et al 1998). I10b identified 2 additional components—L1N and L2SW—in HST/ACS/NICMOS images and argue that the FIR luminosity arises from L2SW based on VLA 1.4 GHz continuum and EVLA CO(1-0) maps. While the FIR emission is dominated by L2SW, the combined SED of the entire system is dominated by the AGN in L1. Because L2SW has very red near/mid-infrared colors, and is

[3] Stellar-types from Vacca et al. 1996

coincident with the molecular gas and 1.3mm continuum emission peaks, it is likely the site of a massive young starburst reflected in its large FIR luminosity (I10b). It is suggested that the individual components may be independent galaxies at different stages of a merger process (I10b). With its 11" FWHM beam, the present observations using ZEUS/CSO enclose all of the components.

In Chapter 1, we describe our detection of the [OIII] 88 μm line from SMMJ02399 with $L_{[OIII]}/L_{FIR} \sim 3.6\times10^{-3}$. By comparing with the Hα and [OIII] 5007 lines, we argue that the system contains a massive starburst with a stellar mass-distribution topped by O7.5 stars and an ionized gas mass of $M_{HII} \sim (1 - 10) \times 10^9\ M_{\odot}$. Our present detection of the [NII] 122 μm line refines and constrains this estimate.

The Cloverleaf quasar (H1413+117) is also a lensed (μ~11) BAL quasar. First detected in an optical spectroscopic survey (Hazard et al. 1984), it is a composite system with a partially obscured AGN dominating the $\sim 7 \times 10^{13}\ L_{\odot}$ bolometric luminosity. Based on strong PAH emission, Lutz et al. (2007) conclude that an extreme starburst dominates the FIR, with $L_{FIR} \sim 5 - 10\%\ L_{Bol}$. The Cloverleaf is well studied in molecular gas tracers (e.g. CO, [CI], ^{13}CO; c.f., Weiß et al 2003, Barvainis et al 1997, Bradford et al. 2009, Henkel et al. 2010). Bradford et al. (2009) find that its molecular gas reservoir, $M(H_2) = 0.2 - 5 \times 10^{10}\ M_{\odot}$, fills a disk between 325 and 650 pc in radius and the hard X-ray flux from the AGN heats the molecular ISM, resulting in a top heavy stellar IMF.

---

[4] We assume a flat cosmology with $\Omega_{\Lambda}= 0.73$ and $H_0=71$ km s^{-1} Mpc^{-1}, and unless noted all values are the intrinsic, de-magnified values obtained using the magnification factors listed in Table 1.

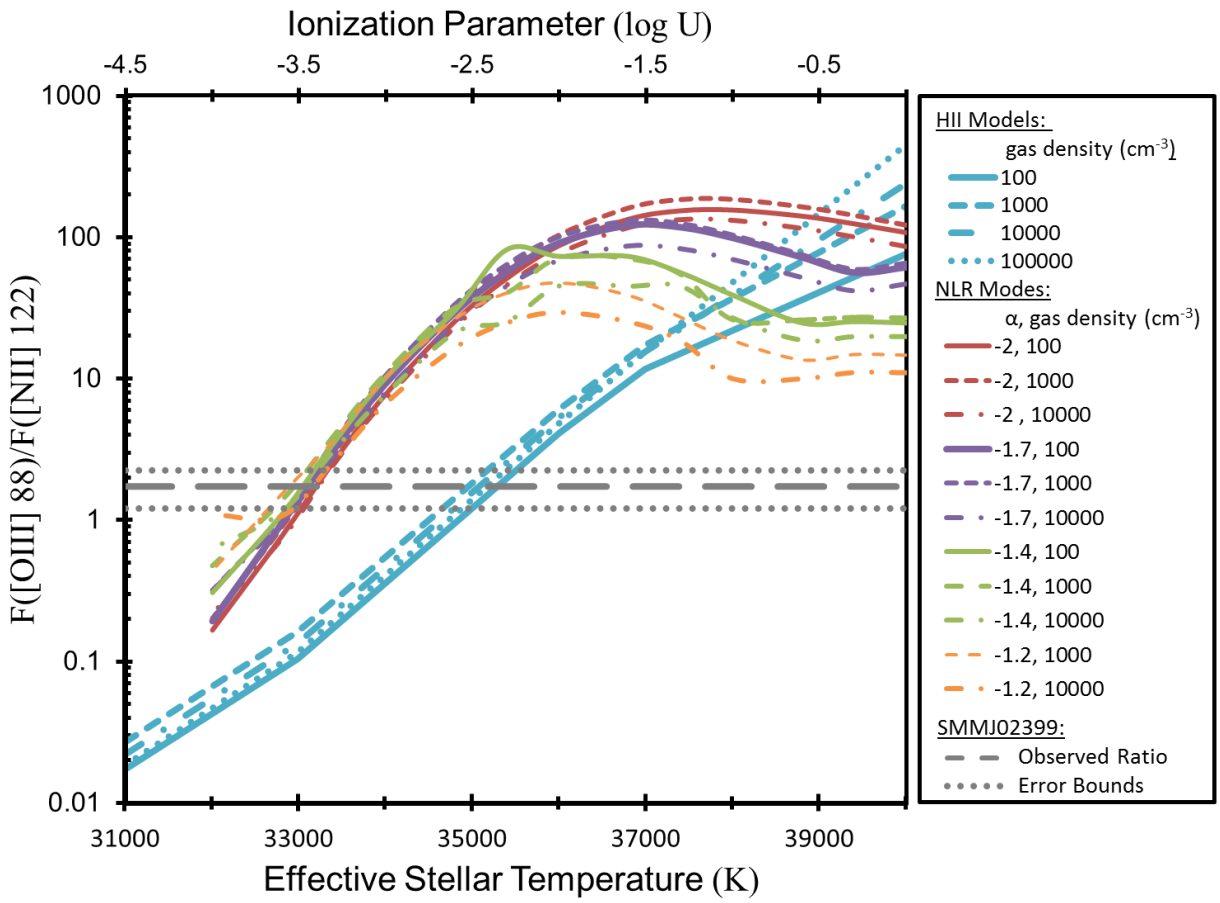

Figure 1. Observed [OIII]/[NII] line ratio from SMMJ02399 with error limits, and the expected line ratio as a function of the effective stellar temperature from the Rubin (1985) HII region models (lower axis) and ionization parameter of the NLR models from Groves et al. (2004; upper axis). The HII region models are plotted for several gas densities, while the NLR models are plotted for various power-law indices, α, and gas densities.

2 OBSERVATIONS

We used the Redshift(z) and Early Universe Spectrometer (ZEUS; Hailey-Dunsheath 2009, Stacey et al. 2007) at the 10.4 meter Caltech Submillimeter Observatory (CSO)[5] on Mauna Kea, Hawaii. ZEUS is a direct-detection echelle-grating spectrometer with R~1000 (see above references for details). Both sources were observed in January 2011 in a chopping and nodding mode with a chop rate of 2 Hz and azimuthal amplitude of 30". For SMMJ02399, the line was detected (6.4σ) in 1.9 hours integration time through a line of sight (LOS) transmission of 32%. For the Cloverleaf, the line was detected (5.7σ) in 1.5 hours with a LOS transmission of 42%. Spectral calibration was obtained using a CO-absorption gas cell while flux calibration and spectral response flats were obtained with a LN_2 cold load. Telescope coupling was measured with observations of Uranus. The final spectra are shown in Figure 2.

3 RESULTS

3.1 *Line Luminosity*

Table 1 lists the source and line parameters. The line is bright with $L_{[NII]}/L_{FIR} \sim 7.0 \times 10^{-4}$ and 2.1×10^{-3} for the Cloverleaf and SMMJ02399, respectively. For nearby systems the typical range is $L_{[NII]}/L_{FIR} \sim 3 \times 10^{-5}$ to 1×10^{-3} (Graciá-Carpio et al. 2010). While the Cloverleaf does lie within this range, it is ~2 times larger than the average ratio. SMMJ02399, on the other hand, is 10 times the average value. The lines from both sources are clearly narrow (< 400 – 600 km/s) suggesting the line arises from the NLR and/or from HII regions.

[5] The CSO telescope is operated by the California Institute of Technology, under funding from the NSF, grant AST-0838261.

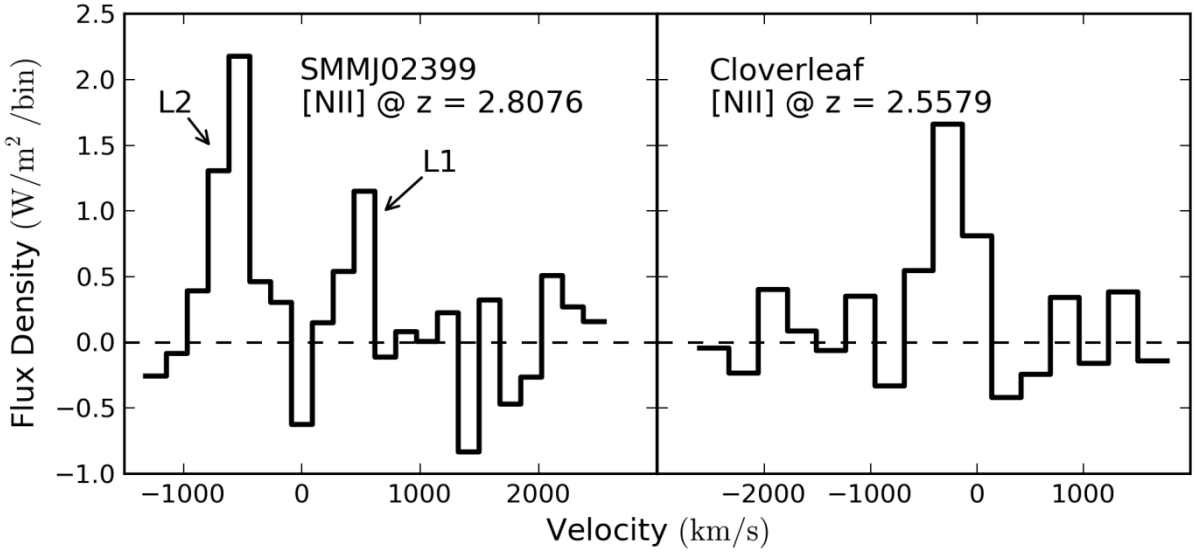

Figure 2. ZEUS/CSO detections of the [NII] 122 μm lines from SMMJ02399-0136 (left) and the Cloverleaf (right) plotted versus their rest-frame velocities. Spectral bins are ~ 1 resolution element, and equal to 200 km/s for SMMJ02399 and 300 km/sec for the Cloverleaf. The continuum emission has been subtracted.

Table 1: Source Parameters

Source Parameter	Units	SMMJ02399	Ref.	The Cloverleaf	Ref.
RA	…	$02^h39^m51.9^s$	…	$14^h15^m46.3^s$	…
DEC	…	-01°35’59”	…	11°29’44”	…
z		2.8076	Genzel et al. 2003	2.5579	Barvainis et al. 1997
D_L	Gpc	23.8	…	20.96	…
Lensing Magnification[a]	…	2.38	I10b	11	Venturini & Solomon (2003)
[NII]122μm Line Flux[b]	10^{-18} W m^{-2}	3.46 ± 0.54	this work	3.03 ± 0.29	this work
[OIII] 88μm Line Flux[b]	10^{-18} W m^{-2}	6.04 ± 1.46	Chapter 1	…	…
L_{FIR}	$L_\odot$	1.22E13	Weiß et al. 2007	5.58E12	Weiß et al. 2003

[a]All values are deboosted using the lensing-magnification factors indicated.
[b]Statistical uncertainties only. Flux calibration uncertainties are ~30%.

Genzel et al. (2003) detect two velocity components in the CO emission from SMMJ02399 at ~ 420 km/s to the red and blue of the nominal systemic redshift of z=2.8076 that are associated with the L1 and L2 components respectively. In chapter 1 we only detected one component in the [OIII] 88 μm line, which at low significance, is shifted ~ 400 km/s to the blue of z = 2.8076. Here we clearly detect the blue component in the [NII] 122 μm line with a hint (2.9σ) of the red component ($1.54 \pm 0.54 \times 10^{-18}$ W m^{-2}). All values and discussion are restricted to the blue, L2 associated component of the [NII] line. Subsequently, we strongly prefer the star-formation explanation of the line emission even though we will show (Section 4.2.1) that both the [NII] and [OIII] line fluxes are consistent with having arisen in the NLR.

3.2 *Minimum Mass of Ionized Gas*

A minimum ionized gas mass, $M_{min}(H^+)$, associated with the line emission occurs in the high-density, high-temperature limit assuming that all nitrogen in the HII regions is singly ionized (see Chapter 1.3.2). This occurs in regions ionized by B2 to O8 stars. $M_{min}(H^+)$ is then:

$$M_{min}(H^+) = F([NII]) \frac{4\pi\, {D_L}^2}{\frac{g_2}{g_t} A_{21} h\nu_{21}} \frac{m_H}{\chi(N^+)}, \qquad (1)$$

where A_{21} and g_2 are the Einstein A coefficient (7.5×10^{-6} s^{-1}) and statistical weight (5) of the $^3P_2$ emitting level, $g_t = \sum g_i \exp(-\Delta E_i/kT)$ is the partition function, h is Planck's constant, ν_{21} is the 122 μm line frequency, D_L is the luminosity distance, m_H is the hydrogen mass, and $\chi(N^+)$ is the N^+/H^+ abundance ratio. For the minimum mass case, $\chi(N^+) = \chi(N)$, the total N/H abundance ratio. We assume "HII region" gas-phase nitrogen abundance for both sources (9.3×10^{-5}, Savage & Sembach 1996), so that $M_{min}(H^+) = 4.0 \times 10^{10}\ M_\odot$ and $2.5 \times 10^9\ M_\odot$, and the minimum ionized-gas to molecular-gas mass ratio, $M_{min}(H^+)/M(H_2)$, is 0.17 and 0.08 for SMMJ02399 and the Cloverleaf, respectively. For SMMJ0299 this is ~10 times larger than the

ratio we obtained in Chapter 1 based on the [OIII] 88 μm line alone. However, if the HII regions are formed by cooler stars than the our model from Chapter 1, with effective temperatures of ~36,000 K for example, then only ~13% of the oxygen is doubly ionized and the minimum ionized-gas/molecular-gas mass ratio obtained using the [OIII] line is consistent with the value obtained using the [NII] line above.

4 DISCUSSION

4.1 *Ionized-Gas Mass*

It is clear that both SMMJ02399 and the Cloverleaf have a very significant amount of ionized gas. Figure 3 shows $M_{min}(H^+)/M(H_2)$ versus the [OIII] 88 μm/[NII] 122 μm line ratio for SMMJ02399, the high-z source SMMJ2135-0102 (Ivison et al. 2010a), and nearby sources observed by ISO (Brauher et al. 2008), all calculated using the method described above. The line ratio for our source is similar to that of the other sources, but the *minimum* ionized mass fractions for the Cloverleaf (8%) and SMMJ02399 (17%), are significantly larger than for the nearby sources. However, we estimate $M_{min}(H^+)/M(H_2)$ ~ 1% for M82, while Lord et al. (1996) determined $M_{min}(H^+)/M(H_2)$ ~ 12% for this nearby starburst galaxy. This suggests that $M_{min}(H^+)/M(H_2)$ for many local galaxies may be significantly larger than the minimum values in Figure 3, so that the high-z mass-fractions may not be unusual.

The very large star-formation rates observed for both SMMJ02399 and the Cloverleaf might naturally produce their large $M_{min}(H^+)/M(H_2)$ fractions. A higher SFR means more HII regions and more ionized gas to produce the bright [NII] emission we observe. To test this idea we plot (Fig. 3, right) the SFR surface density versus $M_{min}(H^+)/M(H_2)$ for the nearby sample (only the [NII] derived values are shown), SMMJ02399, the Cloverleaf, APM08279+5255

(based on [OIII] from chapter 1), and a set of high-z [CII] sources (Stacey et al. 2010), where Mmin(H+)/M(H_2) is estimated by assuming 30% of the observed [CII] line emission arises in HII regions (Oberst et al. 2006). There is indeed a strong trend of increasing $M_{min}(H^+)/M(H_2)$ with increasing star formation. Additionally, all of the high-z sources with SFR $\gtrsim$ 1000 $M_\odot$ yr^{-1} reside at the upper end of the star-formation/mass-fraction relation suggesting that the large ionized mass can be accounted for solely by their enhanced SFR.

Graciá-Carpio et al. (2011) find a FIR-line/FIR-continuum deficit for all FIR lines observed with Herschel/PACs with $L_{FIR}/M(H_2) \gtrsim 80\ L_\odot M_\odot^{-1}$. They argue that the deficit results from higher ionization parameters in these systems and the line deficits and the higher ionization parameters are signatures of merger driven star formation with an associated increase in star formation efficiency. Our observations here and in chapter 1, and the recent [OIII] 88 μm detection from H-ATLAS J090311.6+003906 (Valtchanov et al. 2011) show no such deficit. At present, there are few high-z observations available to test for a high-z deficit, but if future observations show similar ratios to those reported here, then the Garcia-Carpio et al. (2011) model does not describe the high-z population.

4.2 *Gas Excitation Mechanisms*

Both SMMJ02399 and the Cloverleaf are composite systems, so that [NII] emission may arise in the AGN's NLR and/or stellar HII regions. Unfortunately only a few UV, optical or IR lines are reported so that standard AGN/star-forming diagnostics are of limited utility (e.g. BPT diagram; Kewley et al. 2006). Here we analyze the [NII] 122 μm line in both star-forming and AGN paradigms using the HII region models from Rubin (1985) and the NLR models of Groves et al. (2004).

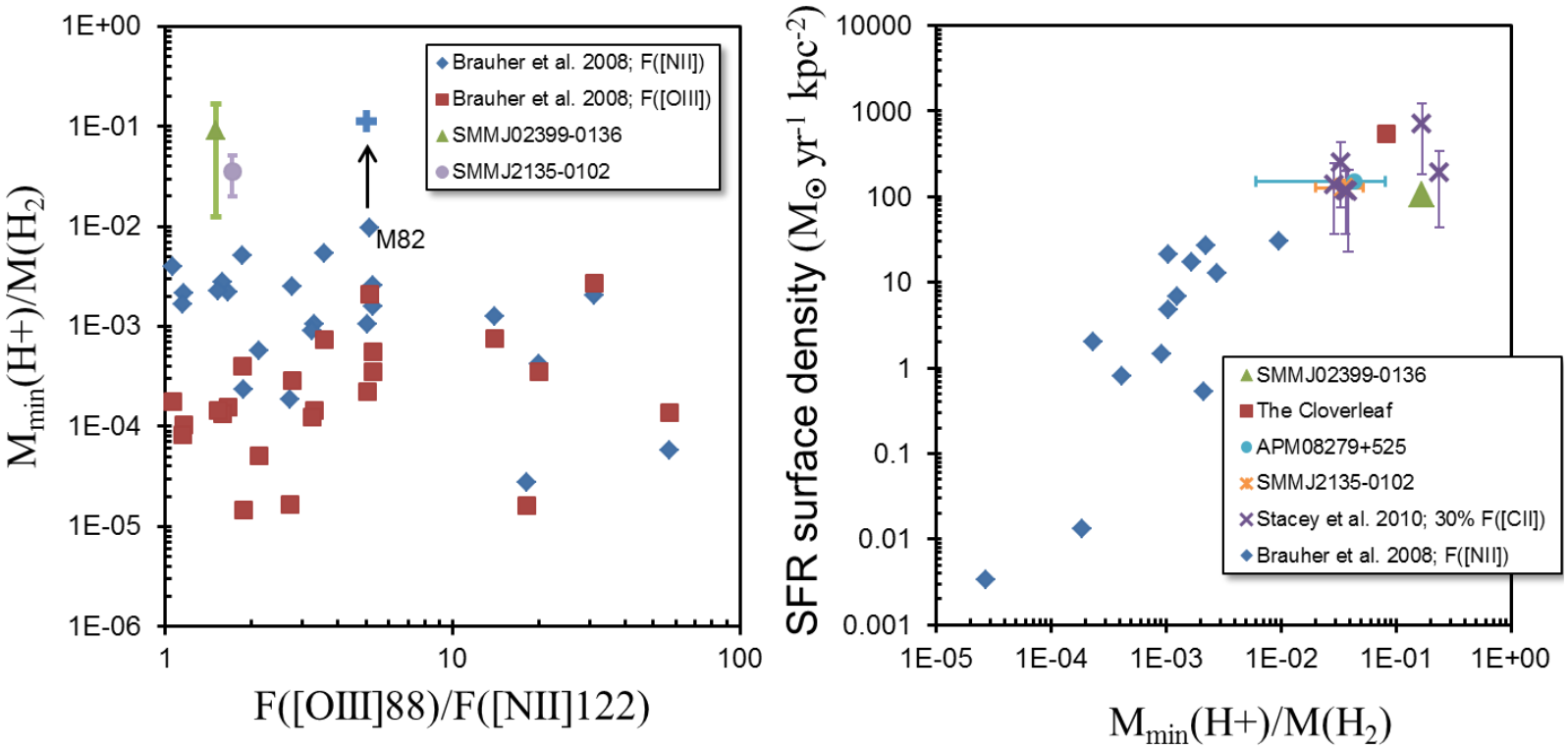

Figure 3. *(left)* $M_{min}(H^+)/M(H_2)$ fraction as determined using the [NII] and [OIII] lines versus the [OIII]/[NII] line ratio for local galaxies from Brauher et al. 2008, SMMJ02399, and line estimates for SMMJ2135-0102 from Ivison et al. 2010a. The error bars are the computed values and the symbols their average. We also label our derived mass fraction for M82 and indicate with an arrow the larger value from Lord et al. 1996 (blue cross). *(right)* SFR surface density versus the $M_{min}(H^+)/M(H_2)$ fraction for SMMJ02399, the Cloverleaf, APM08279+5255, SMMJ2135-0102, a sample of high-z sources with [CII] 158 μm detections (Stacey et al. 2010), and the local sample. The SFR surface densities are from the literature or from their FIR luminosity using the Kennicutt (1998) scaling law.

Rubin (1985) calculates the expected intensities of HII-region emission lines as functions of gas density, effective stellar temperature, T_{eff}, and metallicity. Here we use the "K" models with O/H = 6.76×10^{-4} and N/H = 1.15×10^{-4}. These abundances are near the "HII region" values of Savage & Sembach (1996). We also examine the lower metallicity "D" models with O/H = 1.27×10^{-4}, and N/H = 1.42×10^{-5}. In all cases we use the "49" models with stars producing 10^{49} Lyman continuum photons per second regardless of T_{eff}.

The Groves et al. (2004) models are radiation-pressure dominated and include dust. Their parameter space includes typical ranges for gas density ($n_H = 10^2$ to 10^4 cm^{-3}), power-law index of the ionizing source (α = -1.2 to -2.0), and ionization parameter, *log(U)* = 0 to -4.0. We restrict our analysis to the solar-metallicity, $1Z_{\odot}$, and 25% solar-metallicity, $0.25Z_{\odot}$, models with abundances similar to the "K" and "D" Rubin (1985) models.

4.2.1 *SMMJ02399*

For SMMJ02399 in chapter 1 we compared the [OIII] 88 μm line to sparsely sampled [OIII] 5007Å and Hα maps, and found the gas is ionized by O7.5 (T_{eff} = 40,000) stars and has n_e ~100-1000 cm^{-3}, depending on metallicity. Here, using only the [OIII] 88 μm/[NII] 122 μm line ratio, the best fit HII region models have similar densities: 100 ("K" model) or 1000 cm^{-3} ("D" model). The line ratio does strongly constrain the ionization source at O9.5 (T_{eff} = 35,000 K) stars ionizing a total of $(1 – 4) \times 10^8$ HII regions. These stars are significantly cooler than expected by our work in chapter 1 using just the [OIII] line, demonstrating the utility and importance of using both lines to tightly constrain the stellar populations.

The best fit "K" model suggests an ionized gas mass of 4.8×10^{10} $M_{\odot}$ or 16% of the molecular gas mass, in agreement with the estimate in Section 4.1. The lower-metallicity "D" models predict $M_{min}(H^+)/M(H_2)$ ~ 48%. The increase in $M_{min}(H^+)$ reflects the lowered N and O

abundance. The total luminosity of the stars from the "K" model solutions accounts for 100% of L_{FIR}, but is 28 times larger for the "D" model. This eliminates the "D" model solution since detailed studies of SMMJ02399 require that $L_{optical} \leq L_{FIR}$ (Ivison et al. 1998). Curiously, the optical line estimates from in chapter 1 do not fit the present models. For the best fit "K" HII region model, the [OIII] 5007 and Hα line predictions are respectively 10 times weaker, and 4 times stronger than observed. However, the discrepancy between the optical and FIR lines is not entirely unexpected since the optical lines are very susceptible to extinction effects and their strengths were scaling estimates (see Chapter 1).

For the NLR models the [NII] 122 μm/[OIII] 88 μm line ratio constrains the ionization parameter to between *log(U)* = -3.4 to -3.7 for the solar-metallicity model (see Figure 1) and *log(U)* = -3.3 to -4 for the low metallicity model (Groves et al. 2004). The power-law index is also slightly constrained for the low-metallicity model to between -2 and -1.7. The [OIII] 5007 Å/ 88 μm line ratio provides a constraint on gas density, yielding $n_e \sim 500$ cm^{-3} and $n_e \sim 500 - 1000$ cm^{-3} for the solar and quarter-solar metallicity models respectively. With the lines observed, we are unable to constrain the metallicity. The observed [OIII] 5007 Å /Hα ratio does not fit our NLR model as the Hα fluxes are 10 times weaker than the NLR model predicts.

The fact that the [OIII] 5007Å strength is inconsistent with our HII region model, but consistent with our NLR model solutions suggests a composite model is appropriate. Indeed the AGN is likely responsible for between 25 to 75% of the FIR luminosity (Frayer et al. 1998, Bautz et al. 2000). A composite solution has HII regions, with $n_e \sim 100$ cm^{-3}, formed by slightly coolers stars (O9.5, T_{eff} = 34,500 K) than the pure star-formation model. The NLRs can then account for half the line luminosity given a slightly higher ionization parameter, *log(U)* = -3.3 to -3.45, and $n_e \sim 500$ cm^{-3}. Alternatively, for an HII region with $n_e \sim 1000$ cm^{-3} and a NLR

ionization parameter, *log(U)* = -3.25 to -3.4, ~30% of the line emission is attributable to the AGN and ~70% to star-formation.

4.2.2 *The Cloverleaf (H1413+117)*

Besides our [NII] 122 μm detection, there are no other FIR lines detected from the Cloverleaf for constraining source properties. However, the 6.2 and 7.7 μm PAH features (Lutz et al 2007), and the Hα (1.3×10^{-16} W m^{-2}), Hβ (3.3×10^{-17} W m^{-2}), and the [OIII] 5007Å (1.0×10^{-17} W m^{-2}) lines are detected (Hill et al. 1993). Due to the moderate resolving power of the optical observations it is not clear if any emission arises from broad-line components. Here we assume that the optical lines are narrow and arise either in the NLR or stellar HII regions.

The [OIII] 5007Å/Hα and [NII] 122 μm/Hβ ratios and line strengths are best fit by Rubin (1985) "K" models with $(2 – 3) \times 10^7$ HII regions ionized by O9–O8.5 stars (T_{eff} = 36,000 – 37,000 K). These HII regions have $n_e \sim 100$ cm^{-3}, and $M_{HII} \sim (8–10) \times 10^9 M_\odot$ (the lower value for the O9 stars), so that $M_{HII}/M(H_2) \sim 30\%$. The line ratios are inconsistent with the low metallicity "D" models. The best fit HII region model can account for 50 to 80% of the observed L_{FIR}.

This HII region model is similar to that obtained for M82 (Lord et al. 1996, Colbert et al. 1999). However, Weiß et al. (2003) determine that the Cloverleaf contains both a 115K warm-dust component—likely heated by the AGN—and a 50K cool-dust component that Lutz et al. (2007) attribute to a massive starburst, which dominates the FIR luminosity of the system. The Cloverleaf's cool-dust component is well matched by the single dust component in M82 (48 K, Colbert et al 1999; 50K, Negishi et al. 2001) as are the Cloverleaf's 6.2 and 7.7 μm PAH feature to FIR continuum ratios (Table 2). Therefore we model the Cloverleaf starburst as a superposition of ~200 M82-like starbursts to account for the Cloverleaf's FIR luminosity and

molecular-gas mass being ~200 times larger than M82's. However, the Cloverleaf's [NII] line is ~470 times stronger than M82's, consequently this model can only attribute ~43% of the observed [NII] luminosity to star formation and the associated the cool-dust component of the Cloverleaf. The remaining [NII] line flux may arise, along with the warm-dust component, in the NLR of the Cloverleaf.

Table 2: Comparison between the Cloverleaf and M82

Property	Units	Cloverleaf[a]	Ref.	M82	Ref.	Cloverleaf/ M82 Ratio
[NII] 122 μm Luminosity	($L_\odot$)	3.89E09	this work	8.36E06	Colbert et al. 1999	470
PAH 6.2 μm Luminosity	($L_\odot$)	1.93E10	Lutz et al. 2007	1.72E08	Wild et al. 1992	110
PAH 7.7 μm Luminosity	($L_\odot$)	7.84E10	Lutz et al. 2007	4.60E08	Wild et al. 1992	165
FIR Luminosity	($L_\odot$)	5.58E12	Weiß et al. 2003	2.75E10	[b]	202
Molecular Gas mass	($M_\odot$)	3.00E10	Weiß et al. 2003	1.80E08	Wild et al. 1992.	170
[NII]/ FIR	…	0.0007	…	0.0003	…	2.3
6.2/ FIR	…	0.0035	…	0.0062	…	0.55
7.7/ FIR	…	0.014	…	0.017	…	0.84

[a]Cloverleaf values are intrinsic.
[b]Average of the values from Colbert et al.1999 ($3.2 \times 10^{10}\ L_\odot$); and Rice et al.1998 ($2.3 \times 10^{10}\ L_\odot$)

5 SUMMARY AND OUTLOOK

We have made the first detections of the [NII] 122 μm line at high-z. The line traces AGN and starburst activity providing constraints on stellar populations and AGN/NLR ionization parameters. Further constraints on source properties require additional FIR spectroscopy and the high spatial resolution that Herschel and/or ALMA may provide.

We find that high-z galaxies with high-SFR have large quantities of ionized gas resulting in strong line emission. At high redshifts, there is no the decline in $L_{FIR\text{-}Line}/L_{FIR}$ at high L_{FIR} as seen locally (Graciá-Carpio et al. 2011), so that the FIR lines may be easier to detect from other high-z sources than one would expect extrapolating from local samples. If the strong emission holds true for additional high-z sources, then we will have identified further evidence that galaxies in the past underwent star-formation in a significantly different manner than they do today.

This work was supported by NSF grants AST-00736289 and AST-0722220, and NASA grant NNX10AM09H. We thank the CSO staff for their support of ZEUS operations.

REFERENCES

Abel, N. P., Dudley, C., Fischer, J., et al. 2009, ApJ, 701, 1147
Barvainis, R., Maloney, P., Antonucci, R., & Alloin, D. 1997, ApJ, 484, 695
Bautz, M., Malm, M. R., Baganoff, F. K., et al. 2000, ApJ, 543, L119
Bradford, C. M., Aguirre, J. E., Aikin, R., et al. 2009, ApJ, 705, 112
Brauher, J. R., Dale, D. A., & Helou, G. 2008, ApJS, 178, 280
Colbert, J. W., Malkan, M. A., Clegg, P. E., et al. 1999, ApJ, 511, 721
Ferkinhoff, C., Hailey-Dunsheath, S., Nikola, T., et al. 2010, ApJ, 714, L147
Fischer, J., Sturm, E., Gonz´ lez-Alfonso, E., et al. 2010, A&A, 518, L41
Frayer, D., Ivison, R. J., Scoville, N. Z., et al. 1998, ApJ, 506, L7
Genzel, R., Baker, A. J., Tacconi, L. J., et al. 2003, ApJ, 584, 633
Graciá-Carpio, J., Sturm, E., Hailey-Dunsheath, S., et al. 2011, ApJ, 728, L7
Groves, B. A., Dopita, M. A., & Sutherland, R. S. 2004, ApJS, 153, 9
Hazard, C., Morton, D. C., Terlevich, R., & McMahon, R. 1984, ApJ, 282, 33
Hailey-Dunsheath, S. 2009, PhD thesis, Cornell Univ., AAT 3363492
Hailey-Dunsheath, S., Nikola, T., Stacey, G. J., et al. 2010, ApJ, 714, L162
Henkel, C., Downes, D., Weiß, A., Riechers, D., & Walter, F. 2010, A&A, 516, A111
Hill, G. J., Thompson, K. L., & Elston, R. 1993, ApJ, 414, L1
Hopkins, A. M., & Beacom, J. F. 2006, ApJ, 651, 142
Ivison, R. J., Smail, I., Le Borgne, J.-F., et al. 1998, MNRAS, 298, 583
Ivison, R. J., Smail, I., Papadopoulos, P. P., et al. 2010a, MNRAS, 404, 198
Ivison, R. J., Swinbank, A. M., Swinyard, B., et al. 2010b, A&A, 518, L35
Kauffmann, G., & Heckman, T. M. 2005, Phil. Trans. R. Soc. A, 363, 621
Kennicutt, R. 1998, ApJ, 498, 541
Kewley, L. J., Groves, B., Kauffmann, G., & Heckman, T. 2006, MNRAS, 372, 961
Lord, S. D., Hollenbach, D. J., Haas, M. R., et al. 1996, ApJ, 465, 703
Luhman, M., Satyapal, S., Fischer, J., et al. 2003, ApJ, 594, 758
Lutz, D., Sturm, E., Tacconi, L. J., et al. 2007, ApJL, 661, L25
Lutz, D., Valiante, E., Sturm, E., et al. 2005, ApJ, 625, L83
Maiolino, R., Caselli, P., Nagao, T., et al. 2009, A&A, 500, L1
Maiolino, R., Cox, P., Caselli, P., et al. 2005, A&A, 440, L51
Malhotra, S., Kaufman, M. J., Hollenbach, D., et al. 2001, ApJ, 561, 766

Negishi, T., Onaka, T., Chan, K.-W., & Roellig, T. L. 2001, A&A, 375, 566

Oberst, T., Parshley, S. C., Stacey, G. J., et al. 2006, ApJ, 652, L125

Rice, W., Lonsdale, Carol J., Soifer, B. T., et al. 1988, ApJS, 68, 91

Rubin, R. 1985, ApJS, 57, 349

Savage, B. D., & Sembach, K. R. 1996, ARA&A, 34, 279

Solomon, P., Vanden Bout, P., Carilli, C., & Guelin, M. 2003, Nature, 426, 636

Stacey, G. J., Charmandaris, V., Boulanger, F., et al. 2010, ApJ, 721, 59

Stacey, G. J., Geis, N., Genzel, R., et al. 1991, ApJ, 373, 423

Stacey, G. J., Hailey-Dunsheath, S., Nikola, T., et al. 2008, in ASP Conf. Ser. 375, From Z-Machines to ALMA: (Sub)Millimeter Spectroscopy of Galaxies, ed. A. J. Baker et al. (San Francisco, CA: ASP), 52

Sturm, E., Lutz, D., Tran, D., et al. 2000, A&A, 358, 481

Sturm, E., Verma, A., Graci´ -Carpio, J., et al. 2010, A&A, 518, L36

Vacca, W. D., Garmany, C. D., & Shull, J. M. 1996, ApJ, 460, 914

Valtchanov, I., Virdee, J., Ivison, R. J., et al. 2011, MNRAS, 415, 3473

Venturini, S., & Solomon, P. 2003, ApJ, 590, 740

Weiß, A., Downes, D., Neri, R., et al. 2007, A&A, 467, 955

Weiß, A., Henkel, C., Downes, D., & Walter, F. 2003, A&A, 409, L42

Wild, W., Harris, A. I., Eckart, A., et al. 1992, A&A, 265, 447

Wright, E. L., Mather, J. C., Bennett, C. L., et al. 1991, ApJ, 381, 200

CHAPTER 3

THE 2ND GENERATION z(REDSHIFT) AND EARLY UNIVERSE SPECTROMETER. I. FIRST-LIGHT OBSERVATION OF A HIGHLY LENSED LOCAL-ULIRG ANALOG AT HIGH-z

We recently commissioned our new spectrometer, the 2nd generation z(Redshift) and Early Universe Spectrometer (ZEUS-2) on the Atacama Pathfinder EXperiment telescope (APEX). ZEUS-2 is a submillimeter grating spectrometer optimized for detecting the faint and broad lines from distant galaxies that are redshifted into the telluric windows from 200 to 850 microns. It uses a focal plane array of transition-edge sensed bolometers, the first use of these arrays for astrophysical spectroscopy. ZEUS-2 promises to be an important tool for studying galaxies in the years to come due to its synergy with ALMA and its capabilities in the short submillimeter windows that are unique in the post Herschel era. Here we report on our first detection of the [CII] 158 μm line with ZEUS-2. We detect the line at z ~ 1.8 from H-ATLAS J091043.1-000322 with a line flux of $(6.44 \pm 0.42) \times 10^{-18}$ W m^{-2}. Combined with its far-infrared luminosity and a new Herschel-PACS detection of the [OI] 63 μm line we model the line emission as coming from a photo-dissociation region with far-ultraviolet radiation field, $G \sim 2 \times 10^4\ G_0$, gas density, $n \sim 1 \times 10^3$ cm^{-3} and size between ~ 0.4 and 1 kpc. On the basis of this model we conclude that H-ATLAS J091043.1-000322 is a high redshift analogue of a local ultra-luminous infrared galaxy, i.e. it is likely the site of a compact starburst due to a major merger. Further identification of these merging systems is important for constraining galaxy formation and evolution models.

1 INTRODUCTION

The submillimeter view of the early universe is rapidly evolving. Improvements in instrumentation capabilities over the past 15 years have revealed the submillimeter band (~200 to 850 μm) as a unique probe of star formation in the early universe. These studies were launched by small to modest-sized ground-based surveys, largely of one or two colors, and moderate angular resolution (~10") far exceeding the previous submillimeter surveys of cosmology experiments (e.g. Smail, Ivison & Blain 1997; Berger et al. 1998; Hughes et al. 1998; Weiss et al. 2009; Coppin et al. 2006). Herschel expanded these studies to include both larger scales and multiple colors. From the ground we began high-redshift spectroscopic surveys of far-infrared fine structure lines in the 350 and 450 μm telluric windows with our 1st generation z(Redshift) and Early Universe Spectrometer (ZEUS-1) on the Caltech Submillimeter Observatory ([CII] – Hailey-Dunsheath et al. 2010; Stacey et al. 2010; Brisbin et al. 2014, submitted.; [OIII] and [NII] are described in chapters 1& 2 of this dissertation). The Herschel-SPIRE Fourier transform spectrometer enabled similar submillimeter spectroscopy that was un-obscured by telluric absorption. With the advent of the Atacama Large Millimeter Array (ALMA), studies at wavelengths between 0.43 and 3 millimeters are now making great leaps forward in terms of sensitivity and spatial resolution. However, as Herschel is no longer operating and ALMA has yet to open the 350 μm (Band 10) window, there are limited opportunities to detect far-infrared lines from high redshift systems at wavelengths shorter than ~ 420 μm. For the [CII] 158 μm line, typically the bright FIR fine-structure line, this means ALMA can observe galaxies no closer than z ~1.7 until band 10 is deployed.

We have recently commissioned our new instrument, the 2nd generation z(Redshift) and Early Universe Spectrometer (ZEUS-2) on the Atacama Pathfinder Experiment (APEX) in

Chile[6]. When fully deployed, ZEUS-2 will have wavelength coverage between 200 and 850 microns. For its first run, reported here, ZEUS-2 only accessed the 350 and 450 μm telluric windows. With a spectral resolving power of ~1000 and background limited detectors, ZEUS-2 is optimized for detecting broad lines from galaxies (line-widths of ~200 – 300 km/s). Within these windows ZEUS-2 can rapidly survey high-redshift galaxies, detecting far-IR lines that are spatially unresolved in a typical ZEUS-2/APEX beam (~8 arcsec) yet suitable for follow-up at high spatial resolution with ALMA. In local systems ZEUS-2 can simultaneously map their emission in the ^{13}CO 6-5, CO 7-6, [NII] 205 μm, [CI] 370 μm and the [CI] 605 μm lines that provide important information about the ionized, atomic, and molecular phases of the ISM. Chapter 4 discusses the instrument design and performance in detail.

The star formation and ISM of high-z systems can be studied with ZEUS-2 through the FIR fine-structure lines of carbon, oxygen, nitrogen, and their various ions that are redshifted into the submillimeter atmospheric windows. These lines characterize both the physical conditions of the gas and the ambient radiation fields. They are especially useful for studying dusty galaxies in the early universe where the commonly used optical emission line tracers of the ISM (e.g. [OII] 3726, 3729 Å and [OIII] 4959, 5007 Å) undergo significant extinction, thereby limiting their use as astrophysical probes. The FIR fine structure lines have been extensively studied in nearby extragalactic systems with the Kuiper Airborne Observatory (KAO), the Infrared Space Observatory (ISO) and recently with Herschel (e.g. Crawford et al. 1986, Stacey et al. 1991, Lord et al. 1996, Luhman et al. 1998, Malhotra et al. 2001, Negishi et al. 2001, Brauher et al. 2008, Gracia-Carpio et al. 2011). These studies were extended to high redshift galaxies with

[6] This publication is based on data acquired with the Atacama Pathfinder Experiment (APEX). APEX is a collaboration between the Max-Planck-Institut fur Radioastronomie, the European Southern Observatory, and the Onsala Space Observatory.

Herschel (cf. Ivison et al. 2010, Sturm et al. 2010, Valtchanov et al. 2011, Coppin et al. 2012, Verma et al. 2014 in prep) and regularly detected from the ground with ZEUS-1, as mentioned above, as well as with telescopes like the IRAM 30 meter, the Plateau de Bure Interferometer (PdBI), and ALMA (e.g. Maiolino et al. 2005, 2009, Iono et al. 2006, Swinbank et al. 2012, DeBreuck et al. 2011, Cox et al. 2011, DeCarli et al. 2012, Carilli et al. 2013, Wang et al. 2013). Most recently, ALMA and the PdBI are enabling the spatially resolved studies of these important cooling lines (Wagg et al. 2012, Galhervani et al. 2012).

1.1 *Studies of Far-Infrared [CII] and [OI] Emission*

In nearby systems the [CII] 158 μm and [OI] 63 μm lines are typically the brightest of the FIR lines, with line luminosities between ~0.1 and 1 percent of the FIR luminosity (e.g., Crawford et al. 1986, Stacey et al. 1991, Malhotra et al. 2001). These lines arise in warm and dense photo-dissociation regions (PDRs) that are formed on the surfaces of molecular clouds (Tielens and Hollenbach, 1985) by far-ultraviolet radiation (FUV; 6 eV < $h\nu$ < 13.6 eV) from early-type stars. The gas in PDRs is heated by electrons photo-ejected off small dust-grains by the FUV field and cooled by the [CII] and [OI] lines. The relative strength of the lines depends on both the gas density and strength of the FUV field where the [OI] 63 μm line dominates the cooling at higher densities and FUV fields. Over the typical range of PDR gas densities for extra-galactic sources ($n \sim 10^3$ to 10^5 cm^{-3}), the [CII]/FIR ratio is inversely proportional to the strength of the FUV field, so that it indicates the strength of the FUV field and source size (Stacey et al. 2010).

ISO studies found a decline in the [CII]/FIR ratio for increasingly luminous, nearby galaxies (Mahotra et al. 2001, Luhman et al. 2003). The decline is attributed to dust grains acquiring greater positive charge due to photo-ejection of electrons in the extreme FUV

environment of the compact and intense star forming regions that are induced by major mergers. The accumulated grain charge reduces the gas heating efficiency of the ejected electron, limiting the collisional excitation rate of ionized carbon and tempering the rise in [CII] line emission. As a result, in clouds with densities near or above the critical density of the transition ($\sim 2 \times 10^3$ cm $^{-3}$) that are also exposed to high FUV fields, the excitation of the [CII] line emitting level effectively saturates and higher gas densities and temperatures do not lead to a larger population in the excited level. In such environments the column density of C^+ is determined by dust extinction of the UV photons capable of ionizing carbon, so that the C^+ column only grows logarithmically with FUV flux. Meanwhile the FIR emission continues to increase linearly for increasing FUV fields due to dust reprocessing UV photons so that for increasing FUV fields the [CII]/FIR ratio goes down (Stacey et al. 2010). This explanation is also supported by the suppression of all the FIR fine-structures lines in the FIR luminous systems seen in the study by Gracia-Carpio et al. (2011). In some ULIRGs, however, there may be a significant AGN contribution to the FIR luminosity significantly reducing the [CII]/FIR line ratio if the AGN contribution to the FIR luminosity is not accounted for (Sargsyan et al. 2012).

The first [CII] survey of high-z, FIR luminous systems ($L_{FIR} > 10^{12.5} L_{\odot}$) showed that star formation dominated galaxies in the early universe did not have the low [CII]/FIR ratios characteristic of the ultra-luminous systems nearby (Stacey et al. 2010). It is surprising that their ratios were similar to local moderate-luminosity systems indicating kpc-scale and moderate-intensity star formation – not the concentrated and merger-induced starbursts seen in local ULIRGs. The high-z systems with low [CII]/FIR ratios that are similar to the ratios of local ULIRGs, have buried AGN that dominate their energetics (Stacey et al. 2010). In this chapter we report on observations of a lensed ULIRG that we conclude is a high-z analogue of local

ULIRGs: a system with strong FUV fields and compact, sub-kiloparsec, star formation induced by a major merger.

1.2 *This Chapter: First ZEUS-2 Detection of a Spectral Line from a High Redshift Galaxy*

In this chapter we report the first light spectra of ZEUS-2 on APEX obtained in November 2012. We strongly (~ 12σ) detect the [CII] 158 micron line from H-ATLAS J091043.1-000322 in ~ 66 minutes of integration time. For our analysis we combine our [CII] detection with a recent Herschel detection of the [OI] 63 μm line (Verma et al. 2013, in prep), previous CO (Lupu et al. 2012), and archival Hubble Space Telescope (HST) images. This work is the first spectroscopic use of a transition edged sensed bolometer array, the state of the art in submillimeter detector technology, and demonstrates the scientific potential of ZEUS-2.

In Section 2 of this chapter we describe the source, the ZEUS-2 observations, data reduction and a gravitational lensing model based on archival HST Images. Section 3 presents a combined analysis of the new spectroscopic measurements. The implications of this analysis are discussed in Section 4. Lastly we give our concluding remarks in Section 5. Throughout this paper we have adopted the cosmological parameters of $\Omega_\Lambda = 0.73$, $\Omega_m = 0.27$ and $H_0 = 71$ km s^{-1} Mpc^{-1} (Spergel et al. 2003). We define the far-infrared luminosities to be from 42.5 to 122.5 μm (covering the IRAS 60 and 100 μm bands) following the prescription of Helou et al. (1986). Some authors extend the FIR luminosity to include wavelengths up to 500 microns; these values are typically ~1.5 times larger than the luminosities we report here. The total infrared luminosity, L_{IR}, is the integrated luminosity between 8 and 1000 microns and is ~2 times larger than the FIR luminosity as we define above.

2 THE SOURCE, OBSERVATIONS, AND LENSING MODEL

2.1 *H-ATLAS J091043.1-000322*

First reported by Negrello et al. (2010), H-ATLAS J091043.1-000322 (hereafter SDP11) was identified in the Herschel guaranteed time program Herschel Astrophysical Terahertz Large Area Survey (H-ATLAS, Eales et al. 2010). Subsequent spectroscopic follow-up with Z-spec on the CSO identified several mid-J CO transitions at z = 1.786 (Lupu et al. 2012). Based on its exceptionally bright line fluxes, its very large apparent FIR luminosity[7] ($L_{FIR} = 3.88 \times 10^{13}\ L_{\odot}$) and the identification of a foreground lensing galaxy at z = 0.793, Negrello et al. conclude that SDP11 is a strongly gravitationally lensed, with more moderate intrinsic luminosity. Negrello et al. do not however, constrain the magnification. Using archival HST observations and a simple lensing model we confirm that SDP11 is indeed a lensed galaxy with magnification, μ, between 7 and 29, (see Section 2.3), so that the intrinsic molecular-gas mass and far-IR luminosity are ~ $(0.8 – 3.4) \times 10^{10}\ M_{\odot}$ and $L_{FIR} = (1.3 – 5.4) \times 10^{12}\ L_{\odot}$, respectively. Table 1 lists the observed source properties from this work and the literature.

[7] Negrello et al. 2010 and Lupu et al. 2012 report different values for the FIR luminosities of SDP11 likely due to different definitions of the FIR luminosities. To ensure what we are consistent with our ZEUS-1 sample in Brisbin et al. (2014) we have taken the photometry reported in Negrello et al. and performed our own fit of the spectral energy distribution (SED) using the SED templates of Siebenmorgen & Krugel (2007) and integrating the SED according to our definition of the FIR luminosity in Section 1.2.

Table 1: H-ATLAS J091043.1-000322 Source Parameters

Parameter	Unit	Value	Source
RA	hh:mm:ss.s	9:10:43.1	Lupu et al. 2012
DEC	dd:mm:ss	-00:03:22	“
z	…	1.786	Negrello et al. 2010
μ	…	18 ± 11	this work
L_{FIR}	$\mu \cdot 10^{13} L_{\odot}$	3.88 ± 0.47	this work
M_{H2}	$\mu \cdot 10^{11} M_{\odot}$	2.0	Lupu et al. 2012
$\mu \cdot \Omega_d$	$arcsec^2$	0.43	Lupu et al. 2012
F([CII] 158)	$\mu \cdot 10^{-18}$ W m^{-2}	6.44 ± 0.42	this work
F([OI] 63)	“	7.5 ± 2.3	A. Verma et al., in prep.
CO(2-1)	“	0.0234 ± 0.00257	D. A.Riechers et al., in prep
CO(5-4)	“	0.159 ± 0.053	Lupu et al. 2012
CO(6-4)	“	0.241 ± 0.083	“
CO(7-6)	“	0.174 ± 0.136	“
[CI] 370	“	0.301 ± 0.136	“

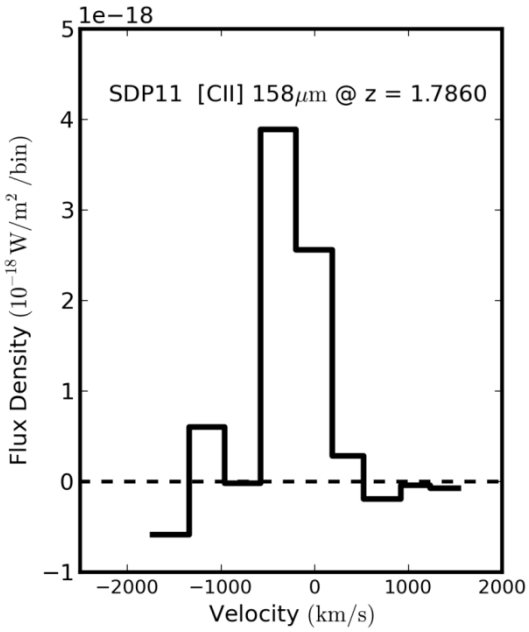

Figure 1: ZEUS-2/APEX detection of the [CII] 158 micron line from H-ATLAS J091043.1-000322 plotted versus the source rest-frame velocity. Spectral bins are ~ 1 resolution element and equal to ~350 km/s. The continuum emission has been removed.

2.2 *Observations*

Using ZEUS-2 on APEX we observed SDP11 on 2012 November 17 under very good observing conditions (0.48 mm of precipitable water vapor). Spectra were obtained in standard chopping and beam switching mode with a chopper throw of 60". We obtained five, 13.2 minute integrations for a total integration time of 66 minutes. The ZEUS-2 velocity resolution at the observed wavelength (439.6 μm) is ~ 340 km/s. The ZEUS-2/APEX beam is 8" (~68 kpc at z = 1.78), as measured on Uranus, which fully contains SDP11. Uranus also served as our flux calibrator using a brightness temperature of 68 K at 450 microns as reported by Hildebrand et al. (1985). Figure 1 shows the detected [CII] 158 micron line with a flux of $(6.44 \pm 0.42) \times 10^{-18}$ W m^{-2}.

2.3 *Lensing Model*

Figure 2 shows a Hubble Wide Field Camera 3 (WFC3) near-IR image (F110W) of SDP11, centered on the lensing galaxy SDSS J091043-000323 (hereafter SDSSJ0910) at z = 0.793 (central elliptical at position 0", 0"). The contours show the HST/WFC3 F160W image divided by the F110W image, i.e. the 1.5 micron/1.1 micron image[8]. On the basis of the spectral energy-distribution (SED) modeling of Negrello et al. (2010) who separately fit an SED to SDP11 and the lensing galaxy SDSSJ0910, we expect both SDSSJ0910 and SDP11 to be brighter in the 1.5 micron band. However the 1.5/1.1 micron ratio for SDP11 is ~4 times larger than that of SDSSJ0910 so we expect the divided image to show a lensed imaged of SDP11. Indeed, the divided image (i.e. the contours if Figure 2) clearly shows an Einstein ring centered on SDSSJ0910.

[8] These images were obtained from the Hubble Legacy Archive and where part of HST Cycle 18 proposal 12194 and are described in detail in Negrello et al. (2013) and Dye et al. (2013).

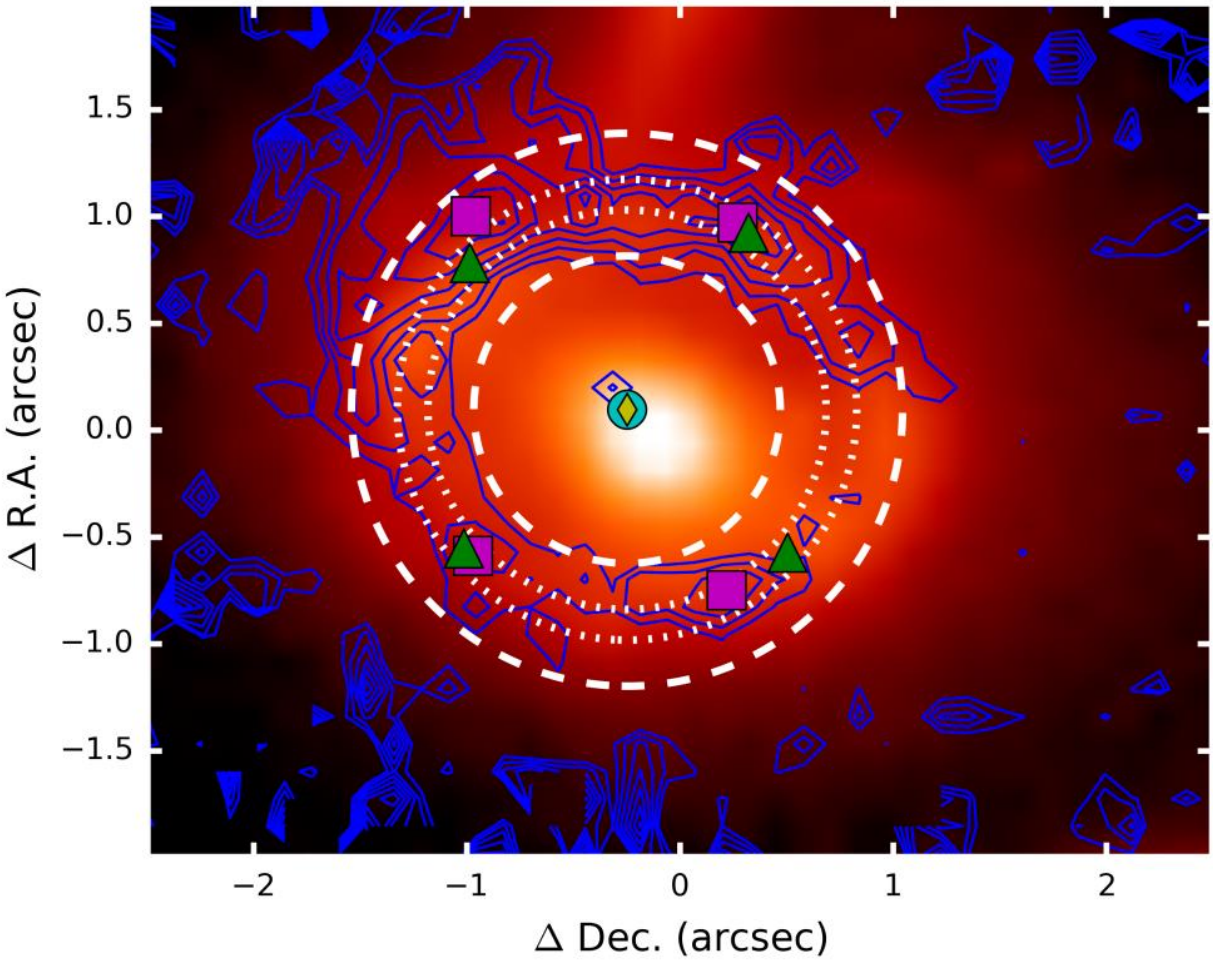

Figure 2: HST/WFC3 F110W image with F160W/ F110W divided image overlaid in blue contours. The squares denote the positions of the peaks in the divided image used for the gravitational lens model described in Section 2.3. The triangles show the best-fit positions of the emission peaks while the diamond locates the best-fit lens and source positions. The white contours are the 70% of the peak-flux limits for Einstein rings produced by our best-fit lens model and an extended source with Gaussian light profile and half-light diameters of 0.7 kpc (dotted) and 3.4 kpc (dashed).

To create a lens model we take the positions of the ring's peak values relative to the centroid of SDSSJ0910 to correspond to lensed images of SDP11 assuming it is a point source. We input the position and values of the peaks in the divided image into LENSMODEL (Keeton 2001) in order to model the gravitational lens system and reproduce the peaks of the Einstein ring. The squares indicate the peak positions while the triangles indicate the predicted image locations based on our model solution. While we obtain an excellent model fit to the image positions and fluxes ($\tilde{\chi}^2 \sim 1$), to determine the magnification and reproduce the observed Einstein ring we use the point-source derived model of the lens, but replace the point source with an extended source.

Replacing the point-source with an extended source adds uncertainty to the magnification factor since we do not know how well the width of the ring in the divided image represents the true source size. With that caveat in mind, a source with a Gaussian light profile and half-light radius of 2.1 ± 1.3 kpc is able to reproduce the observed width of the Einstein ring in Figure 2 and results in a flux magnification, μ, of 18 ± 11. This is of course the magnification of the NIR emission in SDP11. The magnification of SDP11's submillimeter emission could be different if the distribution of the submillimeter emitting region relative to the position of the lens is different. Given the lack of high resolution submillimeter images we adopt the NIR magnification above throughout this paper, with of course the caveat in mind that the submillimeter magnification may in fact be different.

3 ANALYSIS

3.1 *The [CII] 158 μm to FIR Luminosity Ratio: Intense FUV Fields*

SDP11 has an apparent FIR luminosity of $3.88 \times 10^{13}\,L_{\odot}$, placing it firmly in the hyper-luminous infrared galaxy class (HyLIRG, $L_{FIR} \geq 10^{3}\,L_{\odot}$). Figure 3 shows a plot of $L_{[CII]}/L_{FIR}$ ratio, R, for SDP11 versus its apparent FIR luminosity along with samples of local galaxies—normal star forming galaxies and local ULIRGs—and high-z galaxies including the sources from Stacey et al. (2010), Hailey-Dunsheath et al. (2010) and Brisbin et al. (2014). The ratio $R\sim(1.0 \pm 0.3) \times 10^{-3}$ for SDP11 falls between the average line ratios observed for star formation dominated systems ($L_{[CII]}/L_{FIR}\sim3 \times 10^{-3}$) and AGN dominated systems ($L_{[CII]}/L_{FIR}\sim4 \times 10^{-4}$) at high-z. Stacey et al. (2010) and Haley-Dunsheath et al. (2010) show that stronger UV fields may lower the value of R and for a given value of R, i.e. for a given FUV field, the FIR luminosity indicates the spatial scale of the emission. The ratio of SDP11, when compared to the Stacey et al. sample of sources with similar ratios, suggests a FUV field, G, of ~ 10000 G_0, where G_0 is the Habing field—the strength of the local interstellar radiation field corresponding to a flux of 1.6×10^{-3} erg cm^{-2} s^{-1}. Given the value of R from SDP11, its FIR luminosity suggests a source size greater than a kilo-parsec. However, once we account for the magnification of SDP11 its intrinsic FIR luminosity becomes similar to local ULIRGS as well. Magnification does not affect the estimate of the FUV field ($G\sim10000\ G_o$), which is more intense than local normal galaxies or high-z star formation dominated systems, but the lower FIR luminosity now suggests sub-kiloparsec size emission like that found in nearby ULIRGs.

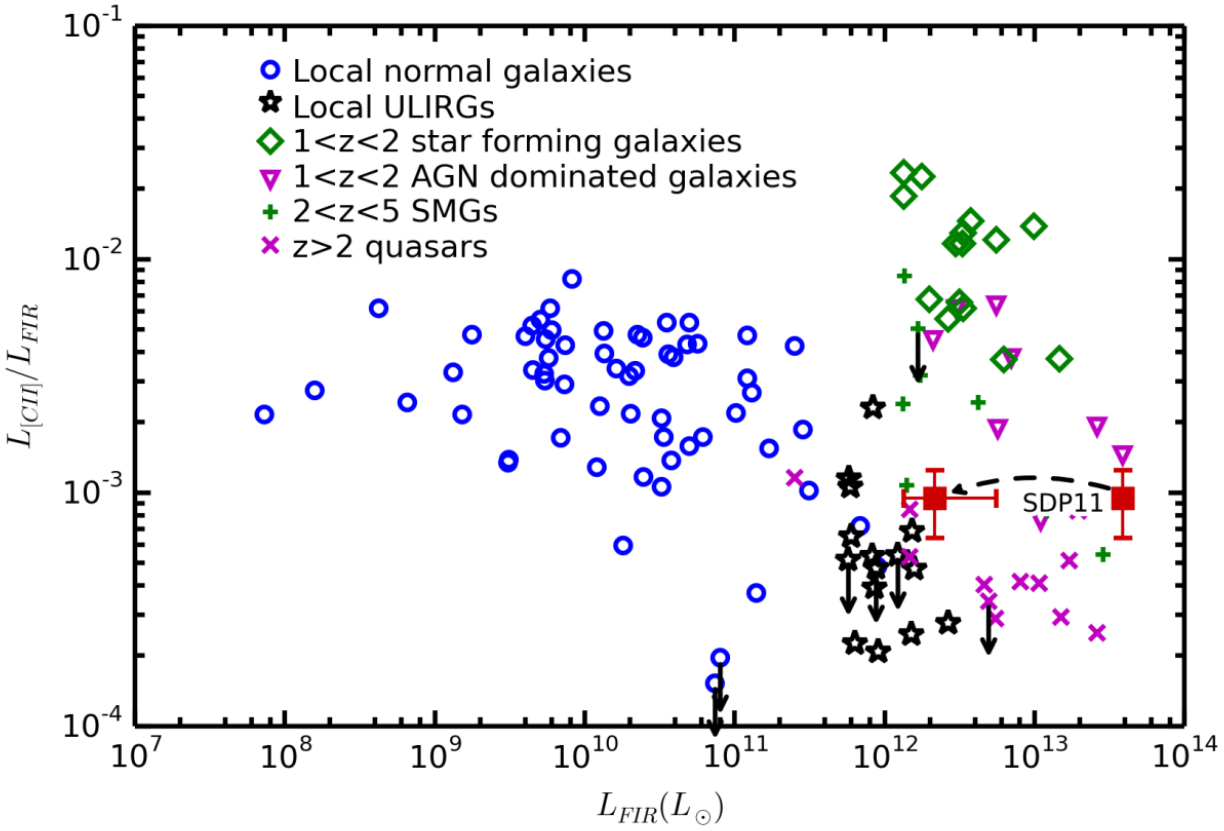

Figure 3: $L_{[CII]}/L_{FIR}$ ratio as a function of the L_{FIR} for local and high redshift galaxies. The ratio from SDP11 (square) is plotted versus both its apparent and intrinsic FIR luminosity. The effect of delensing SDP11 is noted with an arrow while the horizontal error bars indicated the effects of the allowed magnification factors. For comparison we have also included ratios for local normal star forming galaxies (Malhotra et al. 2001), local ULIRGs (Luhman et al. 2003), the ZEUS-1 star forming and AGN samples (Stacey et al. 2010, Brisbin et al. 2014.; Hailey-Dunsheath et al. 2010), z > 2 submillimeter galaxies (SMG: Maiolino et al. 2009; Ivison et al. 2010; De Breuck et al. 2011; Swinbank et al. 2012; Wagg et al. 2012; Valtchanov et al. 2011; Riechers et al. 2013), and z>2 quasars (Pety et al. 2004; Maiolino et al. 2005, 2009; Gallerani et al. 2012; Wagg et al. 2012; Carilli et al. 2013; Maiolino et al. 2005; Leipski et al. 2013; Willott et al. 2013; Venemans et al. 2012)

3.2 *Modeling the Line and Continuum Emission*

Comparisons between our [CII] line, the [OI] line, and the FIR continuum will provide tighter constraints on the ambient FUV fields and gas density in SDP11 as well as the nature of the source. Using the Herschel-PACS spectrometer on the Herschel Space Telescope, Verma et al. (2013, in prep) report a [OI] 63 μm line flux of $(7.5 \pm 2.3) \times 10^{-18}$ W/m^2. Typically the [CII] and [OI] lines are produced in PDRs associated with star forming regions. However, it is possible that both of these lines arise within the x-ray dominated regions (XDRs) produced in molecular clouds enveloping an AGN. Meijerink, Spaans, and Israel (2006) produce grids of observed flux for various FIR fine structure lines, including [CII] and [OI], across typical densities and x-ray fluxes of XDRs. The observed [OI]/[CII] ratio is 1.2 ± 0.5. This is only consistent with the lowest x-ray fluxes and densities ($F_x \sim 0.1$-0.3 erg cm^{-2} s^{-1} and n ~ 100 – 1000), so we expect that the line emission from SDP11 is likely not dominated by an XDR region associated with an AGN. Furthermore, since the currently available photometry of SDP11 can be fit solely by a star formation dominated spectral energy distribution (see Lupu et al. 2012), we proceed with an analysis of the observed [CII] and [OI] lines and far-IR continuum emission within a star formation dominated, PDR paradigm.

Kaufman et al. (2006) produce models grids of PDR regions over a range of densities and FUV fields which we use for our modeling. In performing the PDR modeling we assumed ~ 70% of the observed [CII] flux arise in the PDR, with most of the remaining 30% arising from the warm ionized medium (Oberst et al. 2008). The models of Kaufman et al. assume a single face-on cloud. In reality the PDRs in SDP11 are more complex than used in Kaufman et al., and if we assume they are spherical then we will detect [CII] and FIR emission from both the front and the back of the cloud, while we only see [OI] from the front because it is optically thick. To

make use of the Kaufman et al. models we must then multiply our observed [OI] line flux by two to account for the emission that can be self-absorbed along the line of sight by intervening atomic oxygen. Both of these corrections are appropriate for analysis within a star formation paradigm (Kaufman et al. 1999). In figure 4 we plot the corrected [CII]/FIR and ([CII] + [OI])/FIR flux ratios for SDP11. This gives a PDR model solution of G = 20,000 G_0 and a gas density n = 2500 cm^{-3}. In principle, CO observations are also useful in constraining the PDR model. The observed CO lines are in agreement with our [CII], [OI], and FIR-constrained model, however due to the low signal-to-noise detection of these lines from SDP11, their inclusion does not help to constrain it further as is evident by Figure 4.

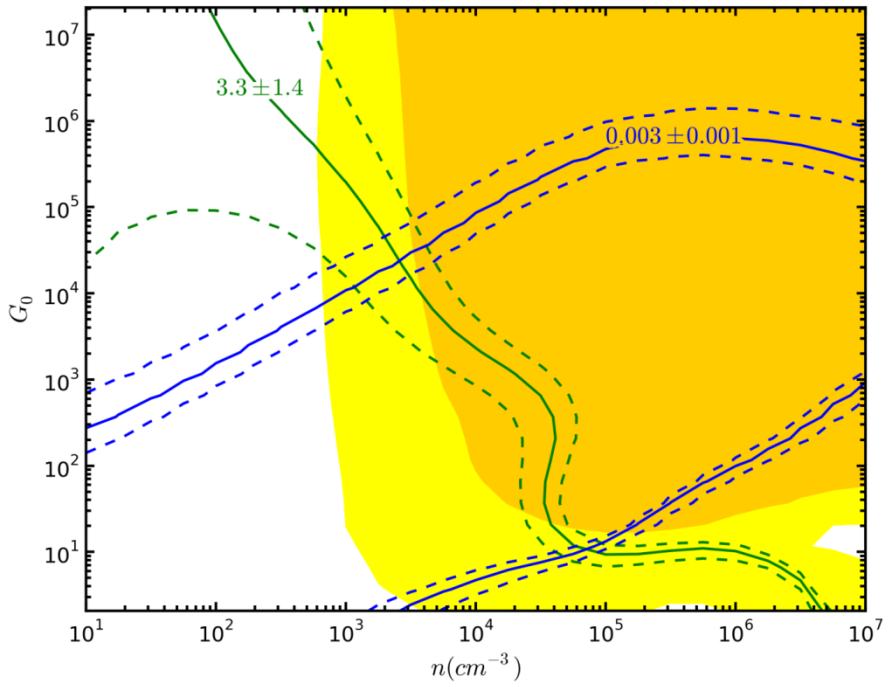

Figure 4: PDR modeling using the online PDR Toolkit (Pound & Woolfire 2008, Kaufman et al 2006) of the corrected [OI]/[CII] ratio (green), ([OI]+[CII])/FIR ratio (blue) from SDP11. The shaded regions show the allowed G_0 and *n* phase space of the mid-J CO observations of Lupu et al. 2012 where yellow is the ratio of [CI] 370 μm + CO(7-6) to CO(5-4) and orange is the CO(6-5)/CO(5-4) ratio. The dash lines indicate ±1σ error bounds of the ratios listed above. For all lines we have corrected for ionized gas and optical depth effects as described in the text.

Our derived FUV field and gas density are consistent with values observed in both local ULIRGS (e.g. Luhman et al. 2003) and high-z sources dominated by AGN (e.g. Stacey et al. 2010) agreeing with our conclusions above that were drawn from the [CII] to continuum ratio alone. While these observations of the [CII], [OI], and FIR alone are not enough to unambiguously identify the nature of the source, being able to account for their strength entirely within a star formation paradigm suggests that SDP11 most likely features a compact starburst similar to those in local ULIRGs. While this does not exclude the presence of an AGN, if one is present in SDP11 it likely does not contribute significantly to our observations or conclusions.

Having constrained the FUV field within SDP11 we estimate the size of the emission region, i.e. the size of the starburst, following the method from Stacey et al. (2010). This will provide additional clues to the nature of the source. Since the FIR emission arises from processing of the FUV radiation by dust, the ratio of the FIR luminosity to the FUV radiation field determines the size of the emitting regions. From Wolfire et al. (1990) the source diameter, D, is proportional to $(\lambda L_{FIR}/G)^{1/3}$ if the mean-free path (λ) of a FUV photon is small. If instead the mean-free path of a FUV photon is large then $D \propto (L_{FIR}/G)^{1/2}$. The constant of proportionality of these relations is determined by assuming that the mean-free path in SDP11 is the same as for M82, which has D ~ 300 pc (Joy et al. 1987), G ~ 1000 G_0 (Lord et al. 1996), and $L_{FIR} \sim 2.8 \times 10^{10}$ $L_\odot$ (the average of the values reported in Colbert et al. 1999 and Rice et al. 1988). The source diameter is then between 0.4 and 0.9 kpc if we assume that SDP11 is lensed a factor between 7 and 29, and we account for the extremes in mean-free path as described above. This agrees with the size of the dust emission determined in Lupu et al. (2012) who estimate the solid angle, $\mu\Omega_d$, of the dust emission region in SDP11 to be 0.43 arcsec^2. Accounting for the

magnification by gravitational lensing, this corresponds to a circular area with diameter between 0.6 and 1.36 kpc, albeit with significant caveats as described in Lupu et al. At the same time our PDR region size is significantly smaller than the intrinsic source size obtained from our lensing model. This disagreement is not a big concern however, and may even be expected. Because the lensing model is based on a 1.5 micron image, i.e. ~397 nm rest frame, it is sensitive to the total stellar component in SDP11. Our PDR analysis is sensitive only to the massive and young O and B stars necessary for the ionization and excitation of [CII]. As such we expect the PDR derived size to be smaller than our lensing model. This also implies that we cannot use our PDR source size to better constrain the results of our lensing model.

4 DISCUSSION

Our analysis suggests that SDP11 is a highly-lensed analog of a local ULIRG system containing a compact star formation region and concomitant high FUV fields, albeit in the early universe. Unfortunately, the true intrinsic source luminosity depends on our adopted magnification factor, which is not well constrained. A useful diagnostic plot that can help confirm our conclusion on the nature of SDP11 is the plot of $L_{[CII]}/L_{FIR}$ versus $L_{CO(1-0)}/L_{FIR}$ as described in Stacey et al. 2010 and shown in Figure 5. Because in the star forming paradigm these lines and the FIR continuum arise in the same regions, these ratios should be insensitive to variations in magnification caused by slight difference in location of the source relative to the critical curve of the lens. In Figure 5 we identify typical regions occupied by nearby sources as well as FUV radiation and density contours from the PDR models of Kaufman et al. (2006). If a source falls in the lower-right section of the plot with $[CII]/CO \leq 4100$, then the observed flux to continuum ratios can be explained fully in a star-forming paradigm. Sources that fall in the upper-left half of the plot may have significant [CII] emission from non-PDR sources such as

XDRs within AGN (Stacey et al. 2010), low density ionized gas, or low metallicity molecular clouds (Stacey et al. 1991).

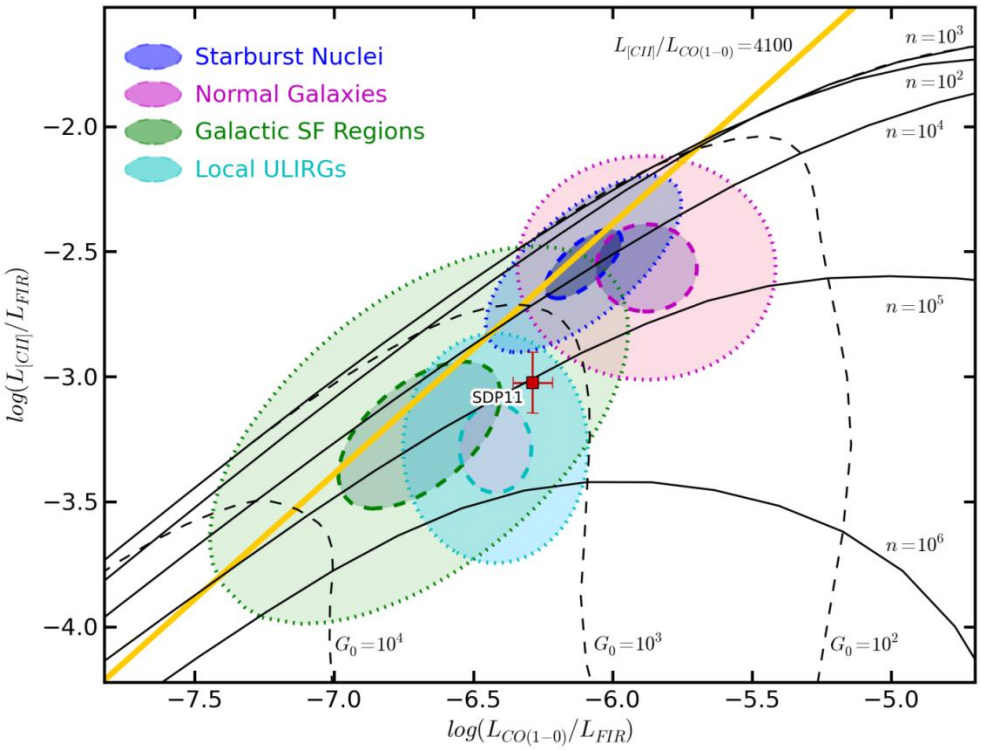

Figure 5: The $\log(L_{[CII]}/L_{FIR})$ versus $\log(L_{CO(1-0)}/L_{FIR})$ for SDP11 adapted from Stacey et al. 2010. Overlaid are the FUV radiation field and gas density contours from Kauffmann et al 2006. The typical $L_{[CII]}/L_{CO(1-0)}$ ratio for star-forming galaxies (~4100) is shown by the thick line. Regions occupied by galactic star forming regions, starburst galaxies, normal galaxies and local ULIRGs are illustrated with 90% (dashed) and 50% (dotted) maximum contours of 2D Gaussians fit to the various source samples from literature (e.g. Stacey et al. 1991, Malhotra et al. 2001, Luhman et al. 2003)

The lowest CO rotational transition detected from SDP11 is the CO 2-1 line from Riechers et al. (2014, in prep). Based on the PDR model solution from Section 6 above we can estimate the ratio of CO(2-1) to CO(1-0) and hence the strength of the CO(1-0) line. For our

model derived FUV field strength and gas density the expected CO(2-1)/CO(1-0) line-integrated flux ratio is 7:1, agreeing with observations of both local and high-z systems (Downes & Solomon 1998; Bradford et al. 2003; Weiss et al. 2005a, 2005b; Ward et al. 2003; Israel 2009; Aravena et al. 2008). Using this estimate along with the observed [CII] and FIR luminosity we place SDP11 on the plot of $L_{[CII]}/L_{FIR}$ versus $L_{CO(1-0)}/L_{FIR}$. The location of SDP11 clearly places it in the ULIRG region of the plot. More generally, because it falls in the allowed region of the plot, we have further support that our analysis in the PDR paradigm and PDR derived source size are indeed correct. As such, SDP 11 does indeed appear analogous to local ULIRGs in terms of luminosity, FUV field strength, and source size, and may contain a starburst produced through the interaction between two Milky Way sized galaxies.

To further confirm the nature of SDP11 we can ask where it falls in the gas mass–star formation relation. Genzel et al. 2010 study the relations between the star formation rate and the molecular gas in galaxies from z ~ 0 to ~3. They find that quiescent star-forming galaxies at all epochs follow a similar relationship between their FIR luminosity and their CO luminosity, tracers of star formation and molecular gas respectively. However, merging systems—both local ULIRGs and high-z mergers—lie above the sequence of quiescently star-forming galaxies suggesting a higher star formation efficiency in merging systems. Where is SDP11? The FIR luminosity and CO(2-1) luminosity scaled to the expected CO(1-0) luminosity as above, places SDP11 among the merging systems suggesting a merger-induced star formation efficiency for SDP11 higher than "normal" galaxies. Over the range of allowed magnification factors, SDP11 falls among the samples of local ULIRGS (μ =29) or high-z mergers (μ = 7) in the L_{FIR}–L_{CO} plane of Genzel et al. (2010). Both of these samples lie on a L_{FIR}–L_{CO} relation that is ~ 4 times higher than normal galaxies.

Studies over the past decade have shown ULIRGs in the early universe to be a very diverse population. Evidence for different modes powering high-z ULIRGs, including AGN, mergers, and the accretion of gas from the IGM, have all been observed. The discovery of the latter mode, however, was very surprising (c.f. Biggs & Ivison 2008; Tacconi et al. 2010; Iono et al. 2009, Hailey-Dunsheath et al. 2010; Stacey et al. 2010). In local ULIRGs star formation is triggered by mergers of massive galaxies (Sanders & Mirabel 1996), and it was long thought that only an AGN or similar major-merger event could produce of the extreme luminosities in high-z systems. We now know the star formation process in some z ~ 1 - 3 systems can also be stimulated through the accretion of cold gas (Tacconi et al. 2013, Genzel et al. 2010, Daddi et al. 2007). The large-scale of these starbursts are best understood as Schmidt-Kennicutt law star formation, with star-forming efficiencies similar to local "normal" galaxies, but with starburst-like star formation rates arising from the large molecular-gas reservoirs accreted from the cosmic web. Studies revealing the accretion mode in high-z galaxies have created a paradigm shift in our thinking about galaxy evolution and formation in the early universe. Recent models have even demonstrated that cold accretion and typical Kennicutt-type star formation efficiencies can fully account for observed black hole growth and stellar mass assembly in the early universe (Di Matteo et al. 2012, Kenes et al. 2005, Genel et al. 2012, Agetz et al. 2011, Kitzbichler & White 2007).

This is not so say that the mergers are uncommon or unimportant in the early universe. For one, observational and theoretical evidence suggests a higher merger rate in the past (Lotz et al. 2011, Hopkins et al. 2010, Bertone & Conselice 2009). Furthermore, the relative importance and prevalence of merger driven versus accretion driven star formation in the early universe is still highly contested because of the observational challenges in identifying merger events at high-z

as well as measuring the full extent and size of gas disks. With the advent of high spatial-resolution submillimeter/millimeter observatories (e.g. PdBI, SMA, and ALMA) we are just now beginning to adequately address this question.

Recently Bothwell et al. (2013) examine the CO and FIR emission of 40 luminous ($L_{FIR} \gtrsim 10^{12}\ L_{\odot}$) galaxies at z ~ 1.2 – 4.1 using the PdBI and selected for in the submillimeter (i.e. submillimeter galaxies, SMG). The authors conclude that 20 – 28% of their sources show signs of an ongoing merger. Yet within the observational constraints there is no evidence suggesting increased star formation efficiencies as one might expect for a merger and as seen in other works (e.g. Genzel et al. 2010). Another indicator of the star formation efficiency in a galaxy is where it falls in the SFR and stellar mass relation (SFR–M_*), which has shown a tight relation between the SFR and stellar-mass in normal galaxies (i.e. accretion mode) with them falling along a "main sequence" (Brinchmann et al. 2004; Noeske et al. 2007; Elbaz et al. 2007). Merging systems lie above the main sequence (Elbaz et al. 2011). Hung et al. (2013) examine the SFR–M_* relation and morphology of the $0.2 < z < 1.5$ Herschel-selected galaxies. Based on morphological classification Hung et al. find that the fraction classified as "irregular" (indicating a merger) increases with IR luminosity at all values of M_*. Furthermore, they find that the fraction of interacting or merging systems increases with L_{IR} as well as distance above the main sequence, with nearly 50% of galaxies showing evidence of a merger at $L_{IR} > 10^{11.5}\ L_{\odot}$. Perhaps most interestingly however is Hung et al.'s finding that ≳18% of IR-luminous galaxies on the main-sequence show evidence of interactions and mergers suggesting that evolution of galaxies on the MS may not be explained by gas accretion and exhaustion alone.

It is clear that there is much work yet to be done in understanding the various modes of star formation and their impact in the early universe. For example one might ask, what is the product

of a major merger at early times? One possibility is that mergers, while not responsible for the bulk of star formation in the universe, are responsible for the formation of modern-day giant ellipticals. Fu et al. (2013) report on the discovery of a system, HXMM01, featuring two submillimeter galaxies in the early stages of a merger. On the basis of the gas depletion time scales and SFRs these authors conclude that HXMM01 may indeed be the progenitor of a modern day elliptical. The merging galaxies in HXMM01 feature star-forming regions of ~1.4 kpc in diameter, similar to the size of the star forming regions we estimate for SDP11. Perhaps then SDP11 represents a later stage in the merger process than HXMM01, in which the galaxies have already coalesced.

To test the various models of galaxy formation and constrain galaxy evolution scenarios we need to look for signs of different modes of star formation, i.e. accretion versus merger driven. Yet, identifying merging systems has proven to be a challenge at high-z. Morphological determinations like those in Hung et al. (2013) require both high sensitivity and high spatial resolutions. Until recently this was easiest to do at visible wavelengths, which of course is compromised by the large dust content of many IR luminous systems at high-z. Now however ALMA allows us to probe the morphologies of early galaxies in their rest frame IR emission, like the work in Fu et al. (2013) mentioned earlier, reducing the challenges of morphological classification. Using ZEUS-2 we can perform a census of the high-z analogues to local ULIRGs by observing their fine structure line emission. By then combining ZEUS-2 and ALMA observations we can morphologically calibrate various FIR fine-structure line ratios in high-z systems to either merger or accretion driven modes of star formation instead of relying on extrapolations from local systems. This will allow us to classify the mode of star formation in systems that are spatially unresolved by ALMA. Lastly, in addition to assessing their total

numbers, we can hope to identify the numbers of high-z ULIRG analogues in their various stages of merger to provide detailed constraints on the peak of the major merger rate in the universe and the effects of mergers on galaxy properties.

5 SUMMARY

We have built a new submillimeter spectrometer, ZEUS-2, and recently commissioned it on the APEX telescope detecting the [CII] 158 micron line from SDP11 at z~1.8. Combining our ZEUS-2 observations with a new Herschel detection of the [OI] 63 micron line, archival HST images, and data from the literature we determine the following.

1) SDP11 is strongly gravitationally lensed with magnification factor $\mu \sim 7$—29.
2) An analysis of the [CII], [OI], and FIR emission within a PDR paradigm yields FUV fields of G~20,000 G_0, gas densities of ~2300 cm^{-3}, and a source size between 0.4 and 0.9 kpc in diameter for SDP11, all of which are similar to values seen in local ULIRGs.
3) We conclude that SDP11 is likely a high-z analog of local ULIRGs featuring a compact and intense starburst confined to sub-kiloparsec scales and induced by a merger of two or more galaxies.

This work demonstrates the science that ZEUS-2 is capable of providing. Due to its synergy with ALMA and it being the only spectrometer capable of observing between 200 and 300 microns in the post Herschel era, we expect ZEUS-2 will be an important tool for studying galaxies in the years to come.

Part of this work is based on observations made with the NASA/ESA Hubble Space Telescope, and obtained from the Hubble Legacy Archive, which is collaboration between the Space Telescope Science Institute (STScI/NASA), the Space Telescope European Coordinating Facility (ST-ECF/ESA) and the Canadian Astronomy Data Centre (CADC/NRC/CSA). ZEUS-2 development and observations are supported by NSF grants AST-0705256, AST-0722220, AST-1105874 and AST-1109476, and NASA grant NNX10AM09H, and a grant from Georgia Southern University. C. F. would like to thank R. Wang for sharing her list of high-z [CII] detections from the literature and in Wang et al. 2013. Lastly we acknowledge the APEX staff whose excellent support helped to make this work possible.

REFERENCES

Agertz, O., Teyssier, R., & Moore, B. 2011, MNRAS, 410, 1391
Aravena, M., Bertoldi, F., Schinnerer, E., et al. 2008, A&A, 491, 173
Barger, A. J., Cowie, L. L., & Sanders, D. B. 1999, ApJL, 518, L5
Bertone, S., & Conselice, C. J. 2009, MNRAS, 396, 2345
Bothwell, M. S., Smail, I., Chapman, S., et al. 2013, MNRAS, 429, 3047
Biggs, A. D., & Ivison, R. J. 2008, MNRAS, 385, 893
Bradford, C. M., Nikola, T., Stacey, G. J., et al. 2003, ApJ, 586, 891
Brauher, J. R., Dale, D. A., & Helou, G. 2008, ApJS, 178, 280
Brinchmann, J., Charlot, S., White, S. D. M., et al. 2004, MNRAS, 351, 1151
Brisbin, D., Ferkinnoff, C., Nikola, T., et al. 2014, ApJ, in press
Carilli, C. L., Riechers, D., Walter, F., et al. 2013, ApJ, 763, 120
Colbert, J. W., Malkan, M. A., Clegg, P. E., et al. 1999, ApJ, 511, 721
Coppin, K., Chapin, E. L., Mortier, A. M. J., et al. 2006, MNRAS, 372, 1621
Coppin, K. E. K., Danielson, A. L. R., Geach, J. E., et al. 2012, MNRAS, 427, 520
Cox, P., Krips, M., Neri, R., et al. 2011, ApJ, 740, 63
Crawford, M. K., Lugten, J. B., Fitelson, W., Genzel, R., & Melnick, G. 1986, ApJL, 303, L57
Daddi, E., Dickinson, M., Morrison, G., et al. 2007, ApJ, 670, 156
De Breuck, C., Maiolino, R., Caselli, P., et al. 2011, A&A, 530, L8
Decarli, R., Walter, F., Neri, R., et al. 2012, ApJ, 752, 2
Di Matteo, T., Khandai, N., DeGraf, C., et al. 2012, ApJL, 745, L29
Downes, D., & Solomon, P. M. 1998, ApJ, 507, 615
Dye, S., Negrello, M., Hopwood, R., et al. 2013, MNRAS, submitted (arXiv:1311.5893)
Eales, S., Dunne, L., Clements, D., et al. 2010, PASP, 122, 499
Elbaz, D., Daddi, E., Le Borgne, D., et al. 2007, A&A, 468, 33
Elbaz, D., Dickinson, M., Hwang, H. S., et al. 2011, A&A, 533, A119
Ferkinhoff, C., Brisbin, D., Nikola, T., et al. 2011, ApJL, 740, L29
Ferkinhoff, C., Hailey-Dunsheath, S., Nikola, T., et al. 2010, ApJL, 714, L147
Fu, H., Cooray, A., Feruglio, C., et al. 2013, Natur, 498, 329
Gallerani, S., Neri, R., Maiolino, R., et al. 2012, A&A, 543, A114
Genel, S., Naab, T., Genzel, R., et al. 2012, ApJ, 745, 11
Genzel, R., Tacconi, L. J., Gracia-Carpio, J., et al. 2010, MNRAS, 407, 2091

Gracia-Carpio, J., Sturm, E., Hailey-Dunsheath, S., et al. 2011, ApJL, 728, L7
Hailey-Dunsheath, S., Nikola, T., Stacey, G. J., et al. 2010, ApJL, 714, L162
Helou, G., Khan, I. T., Malek, L., & Boehmer, L. 1988, ApJS, 68, 151
Hildebrand, R. H., Loewenstein, R. F., Harper, D. A., et al. 1985,Icarus, 64, 64
Hopkins, P. F., Croton, D., Bundy, K., et al. 2010, ApJ, 724, 915
Hughes, D. H., Serjeant, S., Dunlop, J., et al. 1998, Nature, 394, 241
Hung, C.-L., Sanders, D. B., Casey, C. M., et al. 2013, ApJ, 778, 129
Iono, D., Wilson, C. D., Yun, M. S., et al. 2009, ApJ, 695, 1537
Iono, D., Yun, M. S., Elvis, M., et al. 2006, ApJL, 645, L97
Israel, F. P. 2009, A&A, 493, 525
Ivison, R. J., Swinbank, A. M., Swinyard, B., et al. 2010, A&A, 518, L35
Joy, M., Lester, D. F., & Harvey, P. M. 1987, ApJ, 319, 314
Kaufman, M. J., Wolfire, M. G., & Hollenbach, D. J. 2006, ApJ, 644, 283
Kaufman, M. J., Wolfire, M. G., Hollenbach, D. J., & Luhman, M. L. 1999,ApJ, 527, 795
Keeton, C. R. 2001, arXiv:0102340
Keres, D., Katz, N., Weinberg, D. H., & Dave, R. 2005, MNRAS, 363, 2
Kitzbichler, M. G., & White, S. D. M. 2007, MNRAS, 376, 2
Leipski, C., Meisenheimer, K., Walter, F., et al. 2013, ApJ, 772, 103
Lord, S. D., Hollenbach, D. J., Haas, M. R., et al. 1996, ApJ, 465, 703
Lotz, J. M., Jonsson, P., Cox, T. J., et al. 2011, ApJ, 742, 103
Luhman, M. L., Satyapal, S., Fischer, J., et al. 1998, ApJL, 504, L11
Luhman, M., Satyapal, S., Fischer, J., et al. 2003, ApJ, 594, 758
Lupu, R. E., Scott, K. S., Aguirre, J. E., et al. 2012, ApJ, 757, 135
Maiolino, R., Caselli, P., Nagao, T., et al. 2009, A&A, 500, L1
Maiolino, R., Cox, P., Caselli, P., et al. 2005, A&A, 440, L51
Maiolino, R., Gallerani, S., Neri, R., et al. 2012, MNRAS, 425, L66
Malhotra, S., Kaufman, M. J., Hollenbach, D., et al. 2001, ApJ, 561, 766
Meijerink, R., Spaans, M., & Israel, F. P. 2006, ApJL, 650, L103
Negishi, T., Onaka, T., Chan, K.-W., & Roellig, T. L. 2001, A&A, 375, 566
Negrello, M., Hopwood, R., De Zotti, G., et al. 2010, Sci, 330, 800
Negrello, M., Hopwood, R., Dye, S., et al. 2013, MNRAS, submitted (arXiv:1311.5898)
Noeske, K. G., Faber, S. M., Weiner, B. J., et al. 2007, ApJL, 660, L43
Oberst, T. E., Parshley, S. C., Stacey, G. J., et al. 2006, ApJL, 652, L125

Pety, J., Beelen, A., Cox, P., et al. 2004, A&A, 428, L21

Pound, M. W., & Wolfire, M. G. 2008, in ASP Conf. Ser. 394, Astronomical Data Analysis Software and Systems (San Francisco, CA: ASP), 654

Rice, W., Lonsdale, C. J., Soifer, B. T., et al. 1988, ApJS, 68, 91

Riechers, D. A., Bradford, C. M., Clements, D. L., et al. 2013, Nature ,496, 329

Sanders, D. B., & Mirabel, I. F. 1996, ARA&A, 34, 749

Sargsyan, L., Lebouteiller, V., Weedman, D., et al. 2012, ApJ, 755, 171

Siebenmorgen, R., & Krugel, E. 2007, ¨ A&A, 461, 445

Smail, I., Ivison, R. J., & Blain, A. W. 1997, ApJL, 490, L5

Spergel, D. N., Verde, L., Peiris, H. V., et al. 2003, ApJS, 148, 175

Stacey, G. J., Geis, N., Genzel, R., et al. 1991, ApJ, 373, 423

Stacey, G. J., Hailey-Dunsheath, S., Ferkinhoff, C., et al. 2010, ApJ, 724, 957

Sturm, E., Verma, A., Gracia-Carpio, J., et al. 2010, A&A, 518, L36

Swinbank, A. M., Karim, A., Smail, I., et al. 2012, MNRAS, 427, 1066

Tacconi, L. J., Genzel, R., Neri, R., et al. 2010, Nature, 463, 781

Tacconi, L. J., Neri, R., Genzel, R., et al. 2013, ApJ, 768, 74

Tielens, A. G. G. M., & Hollenbach, D. 1985, ApJ, 291, 722

Valtchanov, I., Virdee, J., Ivison, R. J., et al. 2011, MNRAS, 415, 3473

Venemans, B. P., McMahon, R. G., Walter, F., et al. 2012, ApJL, 751, L25

Wagg, J., Wiklind, T., Carilli, C. L., et al. 2012, ApJL, 752, L30

Wang, R., Wagg, J., Carilli, C. L., et al. 2013, ApJ, 773, 44

Ward, J. S., Zmuidzinas, J., Harris, A. I., & Isaak, K. G. 2003, ApJ, 587, 171

Weiß, A., Downes, D., Walter, F., & Henkel, C. 2005b, A&A, 440, L45

Weiß, A., Kovacs, A., Coppin, K., et al. 2009, ApJ, 707, 1201

Weiß, A., Walter, F., & Scoville, N. Z. 2005a, A&A, 438, 533

Willott, C. J., Omont, A., & Bergeron, J. 2013, ApJ, 770, 13

Wolfire, M. G., Tielens, A. G. G. M., & Hollenbach, D. 1990, ApJ, 358, 116

CHAPTER 4

THE 2ND GENERATION z(REDSHIFT) AND EARLY UNIVERSE SPECTROMETER. II. INSTRUMENT DESIGN AND PERFORMANCE

ZEUS-2 is the 2nd generation z (Redshift) and Early Universe Spectrometer. It is a moderate resolution (R~1000) long-slit, echelle grating spectrometer optimized for the detection of faint and broad lines making it well suited for studying galaxies across cosmic time. ZEUS-2 utilizes three transition-edge sensed bolometer arrays enabling simultaneous, multi-beam spectra in up to 4 submillimeter windows. The NIST-Boulder built arrays operate at 120 mK and are read-out via superconducting quantum interference device (SQUID) multiplexers and the Multi-Channel Electronics from the University of British Columbia. Cooling is provided by a pulse-tube cryocooler and two-stage adiabatic demagnitization refrigerator. Bandpass filters perform the grating order selection giving ZEUS-2 access to 7 different telluric windows from 200 to 850 micron. This enables simultaneous mapping of five important submillimeter lines from extended sources. From point sources, like galaxies in the early universe, ZEUS-2 can detect up-to two far-IR fine structure lines simultaneously. ZEUS-2 is designed for deployment to the Caltech Submillimeter Observatory, Atacama Pathfinder EXperiment, and the James Clerk Maxwell Telescope. This flexibility combined with it broad wavelength coverage, access to the telluric windows shorter than 300 microns, and its exquisite sensitivity for broad -line (~300 km/s) detections makes it the most sensitive single dish spectrometer at 350 and 450 microns for and a key tool for studying galaxies in the years to come. Here we detail the design and performance of ZEUS-2.

1 INTRODUCTION

In the submillimeter regime there are many important spectral probes. From nearby systems the far-IR (FIR) fine-structure lines of neutral carbon and ionized nitrogen, and the mid-J rotational lines of CO are observable in the submillimeter windows. From high-z systems the FIR fine-structure lines of carbon, nitrogen, oxygen and their various ions are observable as they are redshifted into the those same telluric windows. Many of these lines are important if not dominate coolants of the ionized, neutral or molecular phases of the interstellar medium (ISM) in galaxies. As such their line strengths and line ratios provide important details on the source of heating (i.e. radiation-field strength and hardness) in their various phases as well as properties of the ISM itself (i.e. gas density & temperature).

We have built the 2nd generation z(Redshift) and Early Universe spectrometer (ZEUS-2) to leverage the power of these various spectral probes in order to studies galaxies both near and far. Specifically we seek to better understand star formation over cosmic time in the following ways.

1) Investigate star formation in the early universe through detections of redshifted far-IR fine-structure lines like the [CII] 158 μm, [OI] 63 & 146 μm, [NII] 122 & 205 μm, and [OIII] 52 & 88 μm lines from distant galaxies. ZEUS-2 is capable, for example, of detecting the [CII] 158 μm line from hundreds of SCUBA and Spitzer sources and thousands of sources that have been detected in more recent surveys by Herschel, the Wide-Field Satellite Explorer, the South Pole Telescope, and the Atacama Cosmology Telescope. As discussed in Chapter 3, the [CII] line is an extremely powerful spectral probe as it traces the physical extent of a starburst as well as its intensity. ZEUS-2 can detect the [CII] line in galaxies over a large redshift range from z ~ 0.25 to 5, and at certain redshifts ZEUS-2 will

simultaneously detect a 2nd fine-structure line such as the [NII] 122 or 205 μm lines for z ~ 1 to 2 galaxies.

2) Measure redshifts of optically obscured distant sources using the [CII] 158 μm line. While there is a wealth of sources detectable with ZEUS-2 that already have spectroscopic redshifts, several recent and ongoing photometric surveys have produced catalogs containing many infrared bright galaxies with only photometric redshifts. These sources, especially those with coarsely determined redshifts based on tracers like PAH emission (e.g. the SWIRE sources in Brisbin et al. 2014), are prime targets for ZEUS-2. They are likely enshrouded by dust making optical spectroscopic follow-up difficult if not impossible, yet ZEUS-2 is well suited for this task due to its large instantaneous bandwidth (up to ~5% of a band, i.e. ~15,000 km s^{-1}) and large redshift range accessible across its seven bands.

3) Investigate star formation and molecular gas excitation in nearby galaxies by simultaneously mapping CO(7-6), ^{13}CO(6-5), [CI] 370 and 609 micron, and [NII] 205 micron lines to produce maps of the physical conditions of major components of the ISM. These maps will allow us to study how conditions in galaxies stimulate star formation. Additional high-J CO and ^{13}CO observations will distinguish between cosmic rays, turbulence, and/or X-rays as the dominate source of heating of molecular clouds in ULIRGS.

Based on the design and scientific success of the 1st generation instrument (ZEUS-1; Hailey-Dunsheath 2009), ZEUS-2 is also a direct-detection echelle-grating spectrometer for submillimeter wavelengths. However, in the development of ZEUS-2 we implemented several design goals ensuring we maximized its scientific potential as compared to ZEUS-1. Namely we

sought to maximize ZEUS-2's sensitivity, spatial and spectral coverage, and accessibility to sources. The last is achieved by designing ZEUS-2 from the outset to be compatible with the several telescopes so that ZEUS-2 can undertake observations of both the northern and southern skies. The other goals were met by leveraging recent technological advances. For example, ZEUS-2 uses closed-cycle refrigerators, significantly reducing its operating costs and allowing the instrument to be used at sites with restricted access to liquid cryogens, such as APEX. In addition, the ZEUS-2 focal plane allows for simultaneous observations at 5 to 10 spatial positions in a total of seven different telluric windows—205, 230, 295, 350, 450, 625 and 850 μm. Finally, the ZEUS-2 focal-plane incorporates three state-of-the-art transition-edge sensed (TES) bolometer arrays with tuned back-shorts allowing for ~90% quantum efficiencies at 215, 400, and 645 microns. These key improvements make ZEUS-2 more sensitive than its predecessor by factors of 1.35 and 1.6 at 350 and 450 microns respectively (reducing integration times required to achieve the same signal to noise by ~45% and 61% respectively), increase the accessible redshifts by more than a factor of 2, and producing a 10x improvement in mapping speed. For broad spectral lines, ZEUS-2 is the most sensitive broad-band submillimeter spectrometer currently available. In its primary bands ZEUS-2 is 3 to 5 times more sensitive than the best heterodyne receivers and 10 times more sensitive than the spectrometers that were deployed on Herschel even with the absorption due to atmospheric water vapor. Perhaps most surprisingly ZEUS-2 is only 30 to 40 times less sensitive the entire 50-antenna ALMA 12-meter array and compared to the ALMA Total Power array, ZEUS-2 has the same and twice the sensitivity at 450 and 350 microns respectively (see Section 3.2).

Currently ZEUS-2 is complete and operational in its primary 350 and 450 μm bands. In 2012 ZEUS-2 underwent an engineering run at the CSO in the spring and a first science run at APEX

in the fall. The later resulted in the first light detection of a high-z galaxy as described in Chapter 3, which serves to illustrate the science enabled by ZEUS-2 observations. For further examples see the scientific results of ZEUS-1 (e.g. Hailey-Dunsheath et al. 2008, 2010; Ferkinhoff et al. 2010; Stacey et al. 2010; Ferkinhoff et al. 2011; Nikola et al. 2011; & Brisbin et al. 2014, submitted) including the work discussed in chapters 1 and 2 of this dissertation. In this chapter we discuss the complete instrument design in Section 2 and the system performance in Section 3. In the later we give specific attention to the performance of the 400 micron array that was installed for the fall 2012 observing run to APEX. Future publications will discuss the performance of the 215/645 micron arrays once fully deployed in ZEUS-2. Lastly in Section 4 we summarize the key details of ZEUS-2.

2 INSTRUMENT DESIGN

ZEUS-2 is depicted in Figure 1 with vacuum-shell closed and in Figure 2 open revealing its internal structure. Key components of the instrument like the Multi-Channel Electronics (MCE), pulse-tube cryocooler, ADR, and grating are noted. The design and selection of these components are described in the subsections on Mechanical Design; Thermal Design, Cryogenics, and Thermometry; Optical Design; Detector Design; Magnetic Shielding; and Detector Readout Electronics.

2.1 *Mechanical Design*

The size of the cryostat (Figure 1) is limited by the instrument envelopes of the observatories considered for the deployment of ZEUS-2; APEX, CSO and the James Clerk Maxwell Telescope (JCMT). Each of these observatories has competing space constraints (Figure 3). The best compromise resulted in a cryostat that is 0.55 meters in diameter and 0.66 meters high. Including the readout electronics (the MCE) mounted directly to the top of the cryostat, ZEUS-2 stands 1.10 meters high.

Weight constraints imposed by the observatories required light-weighting of components wherever possible, especially in the vacuum vessel and temperature stages. The instrument mass totals 130 kg (280 lbs) including the vacuum vessel, magnetic shielding, optics, temperature stages, electronics, cryo-cooler, ADR and detector package. Of this, the off-the-shelf components (ADR, vacuum valve, cryo-cooler, MCE, and stepper motors) account for 50% of the total instrument mass 65 kg (140 lbs). The mounting and alignment structure necessary for mounting ZEUS-2 on a telescope and the fore-optics needed for coupling ZEUS-2 to the telescope beam add an additionally 25 kg (60 lbs) to the total mass of the system. In the subsections below we describe the design of the different components in the mechanical systems including vibration isolators, the vacuum vessel, and G-10 support structures.

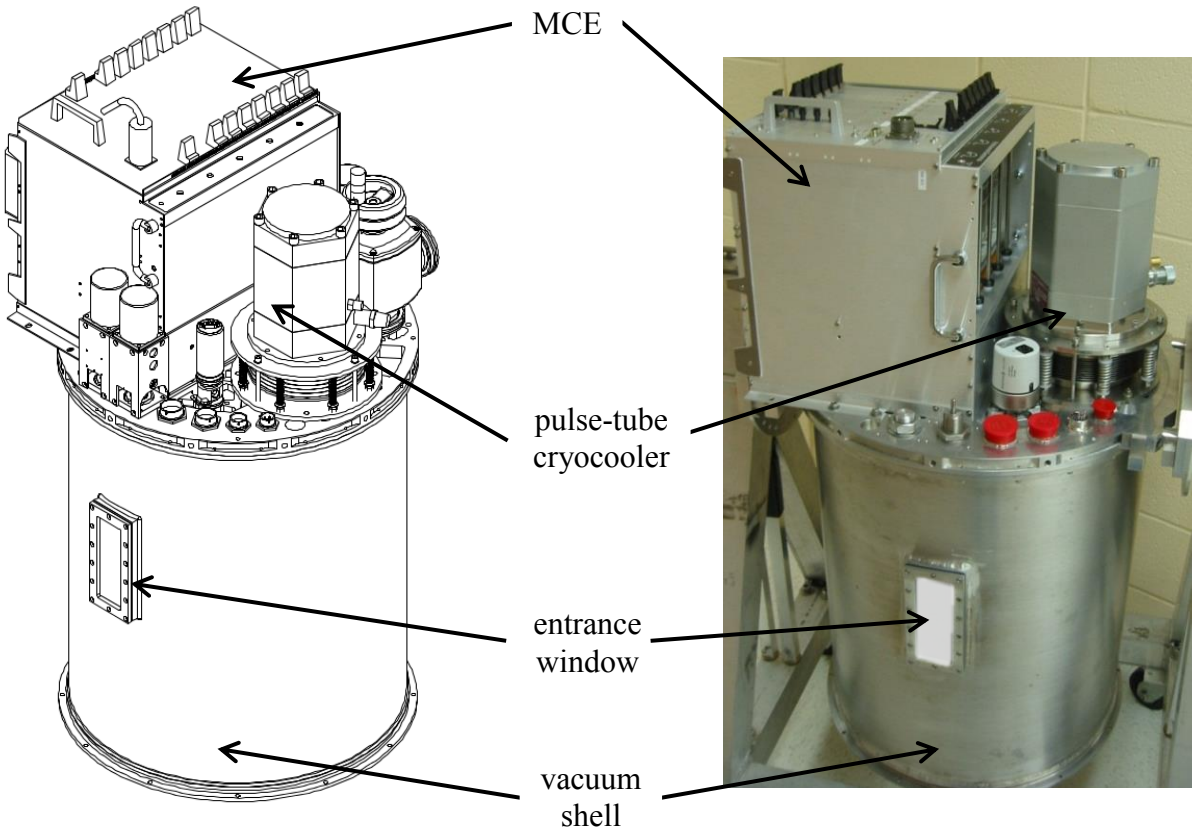

Figure 1: A line drawing of ZEUS-2 (left) and picture of ZEUS-2 mounted on its cart (right) with several key components labeled. ZEUS-2 mounted in its cart.

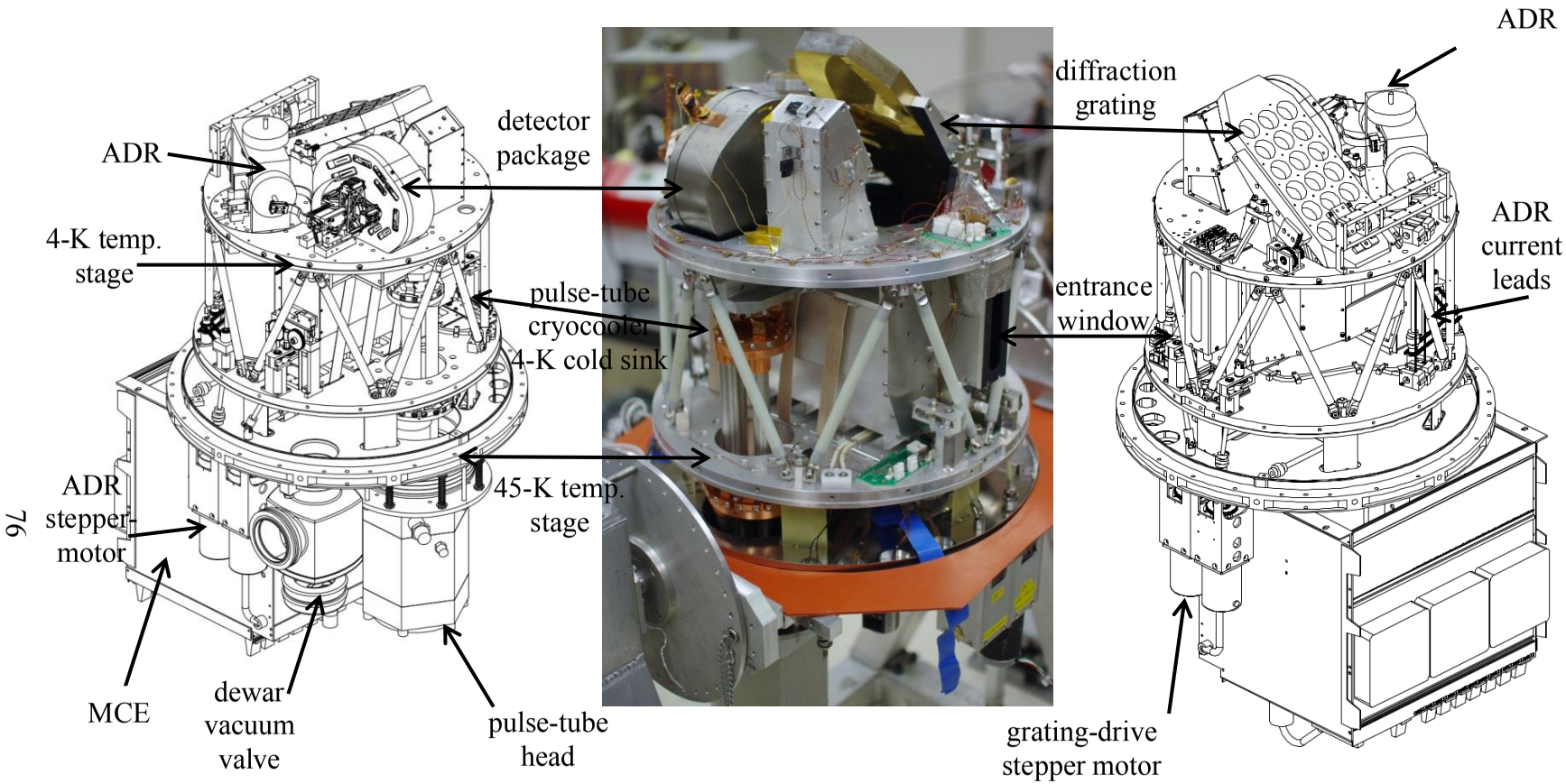

Figure 2: Line drawing of ZEUS-2 (left and right) with 45-K and 4-K heat shield removed and photo of ZEUS-2 open in the lab (center). The instrument is upside down compared to Figure 1, its operational position.

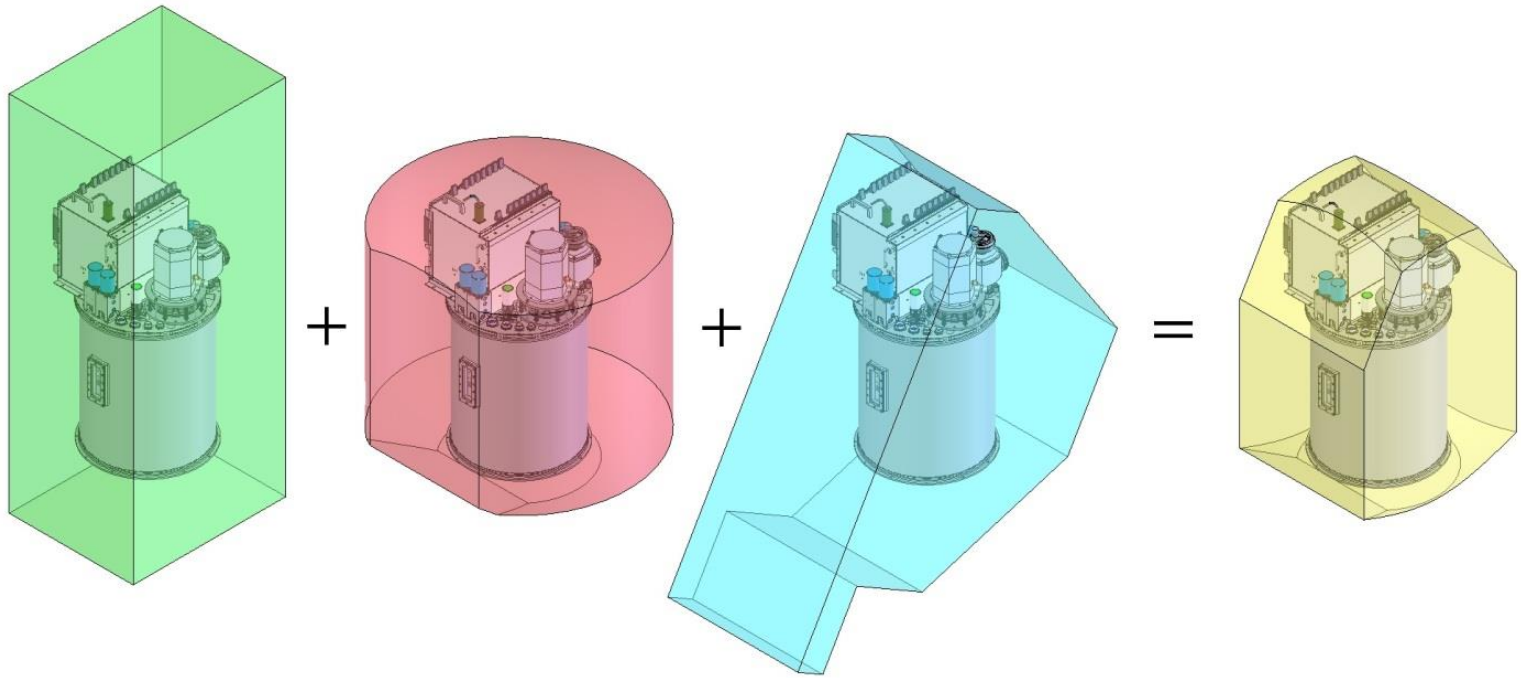

Figure 3: From left the APEX, CSO, and JCMT instrument envelopes and the volume not excluded by any telescope.

2.1.1 *Vibration isolators*

Minimizing mechanical vibrations transmitted into the instrument is important since they can be a source of detector noise and can contribute significantly to total heat loads at milliKelvin temperatures. ZEUS-2 mitigates conduction of external vibrations into the instrument by using flexible and spring interfaces (Figure 4). The instrument, via the vacuum vessel, is mounted to the telescope on vibration isolators minimize vibrations translated into ZEUS-2 from the telescope. The cold head of the pulse-tube cryocooler is mechanically isolated on a spring-bellows and the cryocooler remote-motor is mounted separately to minimize vibrations transmitted to the cryostat from the pulse-tube cryocooler. Inside the cryostat, flexible thermal links connect the cryocooler heat sinks to their respective temperature stage base-plates. This ensures a high degree of vibration isolation and allows for relative motion of the temperature stages due to differential thermal contraction.

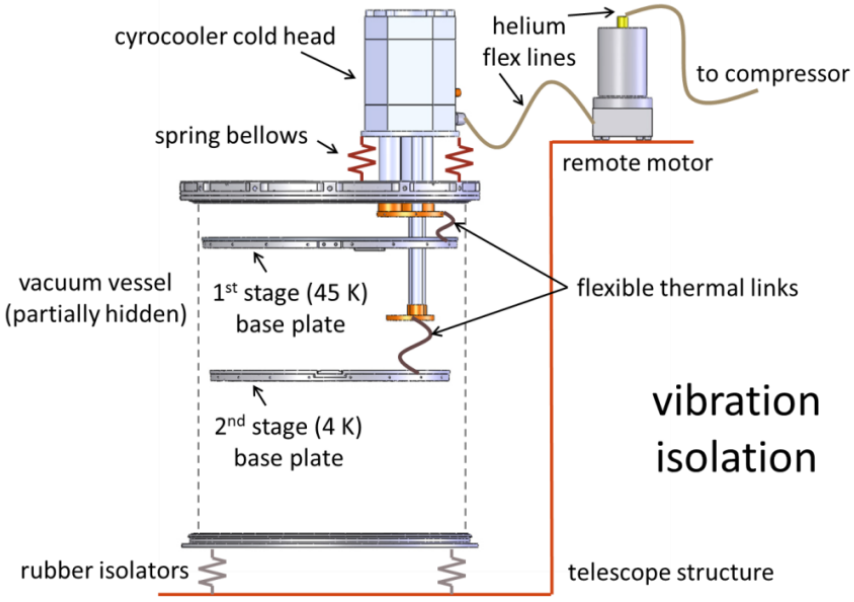

Figure 4: Mounting schematic for the pulse-tube cryocooler, cryostat and telescope. Springs and flexible links isolate the cryostat from the telescope and cryocooler vibrations.

2.1.2 *Vacuum vessel*

The vacuum vessel is the single largest component in ZEUS-2 and was extensively light-weighted to reduce overall instrument weight. Its mass is only 14 kg (31 lbs) making it easily handled by one person. Individual vacuum-shell parts were machined to size and then welded together to form a cylinder with one end closed (Figure 5). Material strength was recovered by heat treating. To avoid excessive distortions during heat treating the cylinder was heat treated in a vacuum chamber and then quenched using high pressure helium gas. Test pieces of different thicknesses were processed at the same time and pulled to failure confirming that we reclaimed the required yield strength.

Figure 5: A picture of the assembled vacuum vessel (pictured upside down) with the extensive light weighting of the bottom plate visible (left), and an exploded view of the vacuum vessel components (right) showing the end plate, rolled cylinder, mounting ring, and window mount prior to being welded together.

In designing the vacuum shell we sought to maximize the vacuum performance. Quickly obtaining a high vacuum inside the dewar is necessary for a quick turn-around between cool-down cycles while maintaining the high vacuum is important to ensure gas-conductive heat loads are negligible. To maximize the vacuum performance the O-ring lengths on the vacuum vessel are kept to a minimum and the turbo molecular pump (TMP) is mounted directly to the main dewar valve. In this configuration the vessel volume of 120 liters can be evacuated from atmospheric pressure to less than 10^{-3} mbar in about two hours, at which point the cryocooler is started. When the TMP is separated from the vessel by a one meter long hose a significantly longer pump-down time (8 hours) is required to reach the same pressure. Once the cryostat is cold the TMP is closed off and removed. With the TMP and cryo-pumping the vacuum vessel achieves a vacuum of $< 1 \times 10^{-8}$ mbar (the maximum range of our pressure gauge) and can maintain this vacuum for at least one month (the longest time the instrument has been continuously cold) without any apparent degradation.

2.1.3 *G-10 Structures*

G-10CR glass epoxy laminate (G-10) support structures are used between the first two temperature stages to provide a rigid support structure while minimizing conductive heat load. G-10 tabs isolate the 45 K stage from room temperature while dodecapod rods provide isolation between the 4 K and 45 K stages (Figure 6). Computer simulations show that the bulk of the stress in the material of these load-carrying members comes from differential thermal contraction between the G-10 and the metal end-fitting which is adhesively bonded to the G-10. The super-alloy Inconel 718 is nearly an optimal match to the coefficient of thermal expansion of G-10 for planar movement and is used in the tabs (Hartwig & Knaak 1984). Selection of materials for the rods however is slightly more complicated because G10 has different thermal expansion parallel-

to than normal-to the plane of the material. This means that a cylinder of G-10 will tend to fight itself, trying to expand more in the radial dimension than in the circumferential dimension. Simulations of G-10 show that for this geometry the inside cylinder diameter has a lower effective expansion (~10%) than a planar geometry. In this case Nitronic 60 (nickel steel) or Inconel 718 show approximately the same stress in the assembly, but being easier to fabricate, Nitronic 60 is used for the rod assemblies. The tabs and rods are glued in precision jigs to keep their lengths consistent. The assemblies resilience to being cooled to cryogenic temperatures was confirmed by repeatedly plunging the parts into liquid nitrogen from room temperature. To date the units installed in ZEUS-2 have operated without fail for more than fifty cool-down cycles and have survived shipments to and from both Hawaii and Chile.

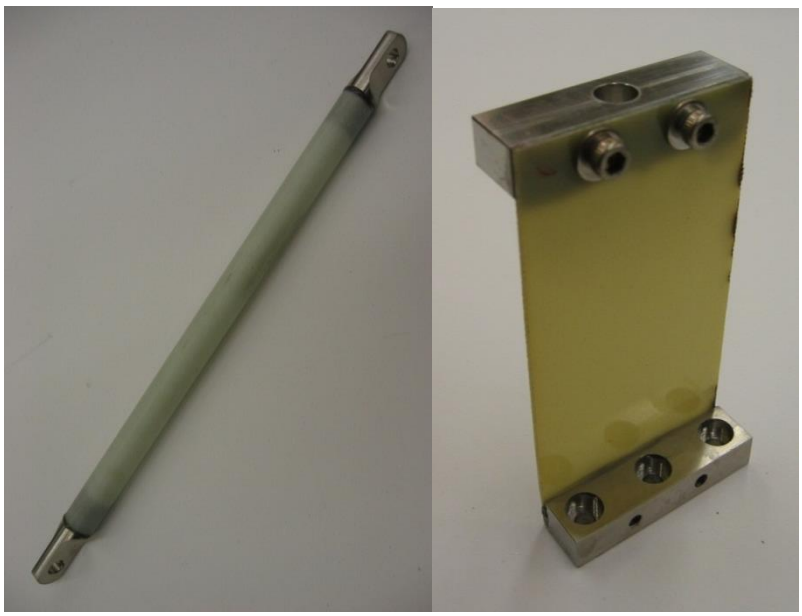

Figure 6: A picture of a rod for the 1st to 2nd temperature-stage dodecapod (left) and a tab for the room temperature to 1st stage (right).

2.2 *Thermal Design, Cryogenics, and Thermometry*

The TES bolometer arrays designed for ZEUS-2 require bath temperatures below ~ 170 mK, the transition temperature of the TES. These temperatures are beyond the range of the closed-cycle helium-3 refrigerator used in ZEUS-1, and necessitate an adiabatic demagnetization refrigerator (ADR). The ZEUS-2 ADR is a two stage unit from Janis Research Company, LLC, containing two pills, gadolinium gallium garnet (GGG) and ferric ammonium alum (FAA). The pills provide a 1.5 K thermal guard (3rd temperature stage) and a milliKelvin bath for the detectors (4th temperature stage), respectively. A two-stage pulse-tube cryocooler (Cryomech, Inc. model PT407-RM) provides a 45 K thermal guard and 4 K bath for the optics and ADR, the 1st and 2nd temperature stages respectively. The combination of ADR and cryocooler enables remote control of system temperatures and extended operations with minimal support from personnel.

From first starting the cryocooler it takes 32 hours until the system has cooled to 4K and the ADR can be cycled. When warming up using external heaters (e.g. an electric blanket and heat gun) and backfilling with nitrogen gas it takes ZEUS-2 about 36 hours to warm up to room temperature. The detector package can reach a minimum temperature of ~85 mK, but we actively control the ADR to hold the detector package at 120 mK for ~ 7 hours, requiring two cycles per day with an ADR cycle lasting 5 hours. We are currently working to improve this hold time to our target of 12-14 hours via several modifications. One is improving the thermal link between the 2nd stage pulse-tube heat sink and the ADR so that the starting temperature of the ADR cycle is closer to the 3 K temperature at the heat sink instead of ~4.5 K, its current initial temperature. A second is to reduce the power scattered into the space between the 45 and 4-K heat shields, which will also lower the start temperature of the ADR.

2.2.1 *MilliKelvin Structure*

The milliKelvin structure for the detector-package is based off a NASA design (Roach 1998), though heavily modified for ZEUS-2. The basic design is composed of two structural beams at different temperatures, arranged in a cross and separated by eight Kevlar threads that fully constraining the two pieces. We chose to make individual thread assemblies that allow a single unit to be replaced in the event of thread failure rather than a continuous length for the whole structure as was done by NASA. The original NASA design would require reworking of the entire mount if a thread broke. The individual thread assemblies can be tightened to remove creep and stretch in the threads as well as to apply a pre-tension. The full milliKelvin structure uses two pairs of beams (Figure 7). One provides thermal isolation between the 2nd and 3rd stages, while the second isolates the 3rd and 4th temperature stages.

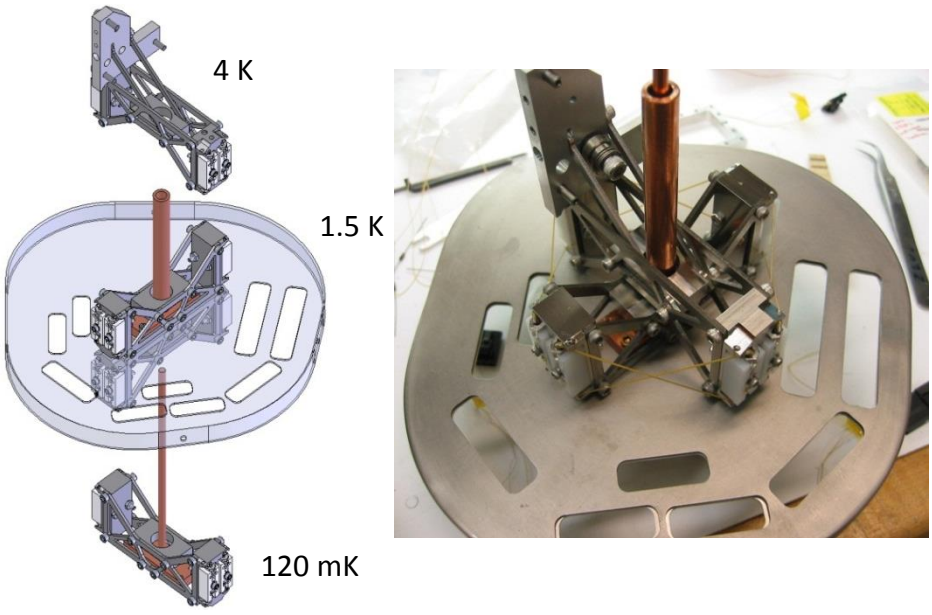

Figure 7: A picture of the assembled milliKelvin mount (right) and an exploded drawing of the assembly (left) showing the temperature stages. The same titanium beam and Kevlar thread assemblies are used for all stages with the temperature buses run coaxially through the center of the mount.

A Kevlar based structure was used to minimize the heat-load from the support structure on the 1.5 K and milliKelvin temperature stages. This is necessary due to the relatively high heat-load from the detector readout cabling compared the limited cooling power of the ADR. The calculated total heat load is 9.5 μW and 430 nW for the 3rd and 4th temperature stages, respectively. Of this, the Kevlar structure only contributes ~10% to the 3rd stage and ~20% to the 4th stage, compared to the ~80% and ~70% contributed respectively to each stages heat load by the wiring.

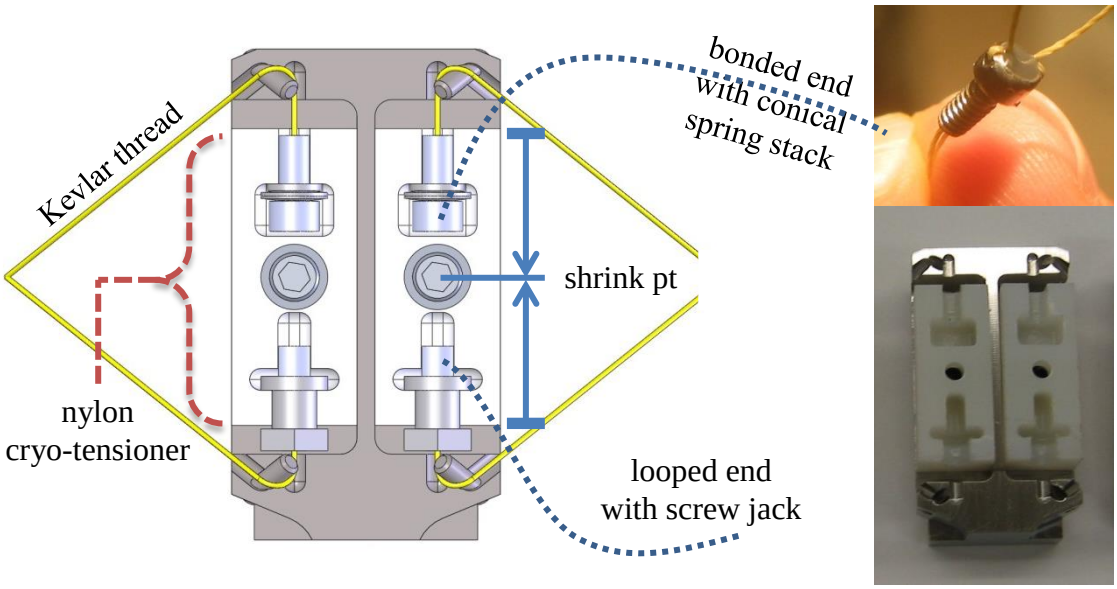

Figure 8: A drawing of the end of a beam assembly (left) and pictures of the bonded end of a thread assembly (right, top) and two empty cryo-tensioners (right, bottom). The cryo-tensioners compensate for the expansion of the Kevlar and the contraction of the titanium when cold, maintaining the preloaded tension on the threads and ensuring a stiff structure regardless of temperature.

The thread assemblies are double threaded, looping over a pin in a vented screw head and terminated on the other side by looping through holes in another vented screw head and bonding in place with Epoxy 2216 (Figure 8). Thread assemblies were made in batches using a jig to minimize variation in lengths. All finished assemblies were proof tested to 150 N (34 lbs) ensuring adequate strength as a single thread has a breaking strength of 125 N (28 lbs).

While Kevlar is an excellent choice for limiting thermal conduction between temperature stages, it is unfortunately known to expand when cooled to cryogenic temperatures (Hartwig & Knaak 1984). To maintain tension in the threads when the Kevlar is cold it is necessary to take-up this expansion. Given that the mount is titanium with a small coefficient of thermal expansion (CTE), the addition of a polymer to the mount is required to produce the necessary change in position of the Kevlar anchor points and maintain tension in the threads when the system is cold. As such we made nylon cryo-tensioner blocks that are able to deliver, in the limited space of the mount, the necessary displacement to maintain the tension in the Kevlar. The thread assemblies are mounted in the cryo-tensioner with a stack of conical springs on one end and a screw-jack for pre-tensioning and adjustment on the other. The nylon is also sufficiently stiff so that the cryo-tensioner blocks are able to withstand the force of the Kevlar thread assemblies without deformation.

2.2.2 *Flexible thermal links*

Flexible thermal links are used to connect a single temperature stage to its heat sink for each of the four temperature stages in ZEUS-2. Mechanical flexibility in the links is required to minimize transmitted vibration (as discussed in Section 2.1.1) and to minimize stresses caused by differential thermal contraction of materials. The links are made from oxygen free, high conductivity (OFHC) copper, which has a high thermal conductivity and therefore minimizes the

mass needed to provide the necessary heat conduction while keeping the links thin and flexible as possible.

All the links (Figure 9) are fabricated in house and share a common design philosophy. Because one would like to limit the number of serial mechanical joints in the design to avoid excessive contact resistance in the thermal link, the design exploits parallel heat transport via multiple layers of copper foil for flexibility that are clamped between copper blocks for mounting purposes. In all cases the copper foil and parts are machined as one unit. This provides a mounting surface that is free of oxide, maximizing the conductivity of the joint. Measured temperature drops across the thermal links are low, ~2 K and ~0.1 K for the 1st and 2nd stage links, respectively.

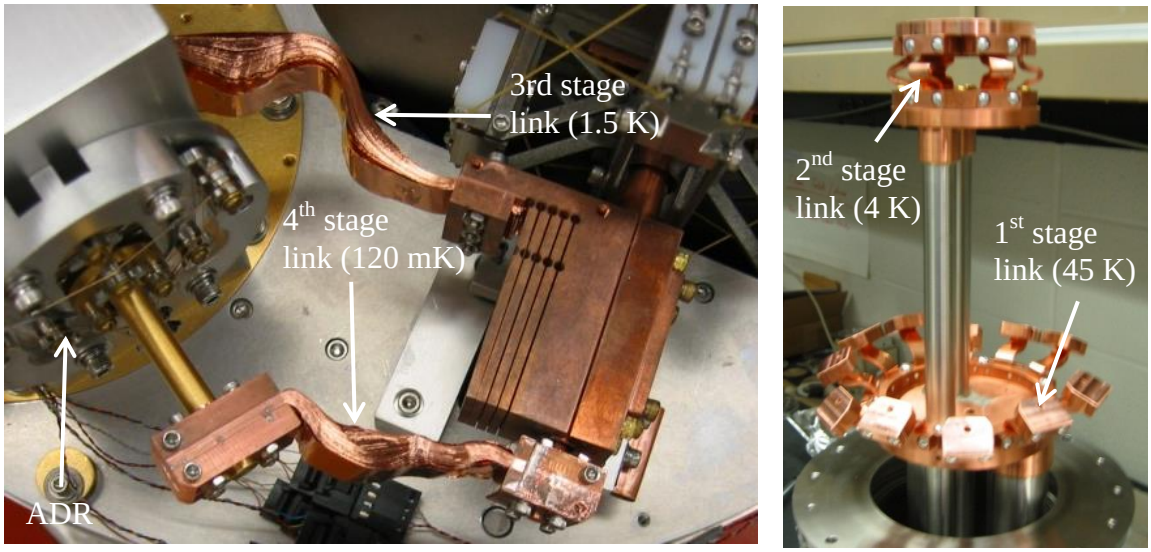

Figure 9: Pictures of all four thermal links, assembled in-house, using copper foil to provide flexibility. The foil layers act in parallel to transport heat.

2.2.3 *ADR current leads*

The ADR requires approximately 10 amps of current to produce the 4 Tesla field needed to fully magnetize the salt pills during an ADR cycle. This current must be kept in mind in order to minimize the heat load from both conduction and Joule heating in the various current leads and connections. The diameter of the conductive leads is set so that the total heat load is minimized. The heat load from conduction is minimized by using a small diameter conductor, while minimizing the contribution from Joule heating requires a large diameter conductor. This means for a given conductor, carrying a specific current between two temperature stages, there is a minimum conductor diameter that minimizes both conductive and dissipative loads (Weisend 1998). Such optimally sized copper wires are used for carrying the ADR current from the ZEUS-2 vacuum plate to the 1st temperature stage. Large diameter (2.6 mm) copper bus wires then make the run across the 1st stage base plate. This large diameter keeps the Joule heating in this run small. The heat produced in the bus wires is calculated to be only ~ 0.1% of the total load for the stage. High temperature superconducting (HTS) leads are used between the 1st and 2nd stages (Figure 10) to minimize both conductive load between the stages as well has dissipative heating. The HTS leads obtained by SuperPower, Inc. use a Yttrium Barium Copper Oxide superconductor, deposited on Hastelloy® ribbon with a copper overcoat. Their conducted heat load is about one quarter that of an ideal copper-only current lead.

Electrical joints for the ADR current leads are detailed in Figure 10. Both ends of the HTS leads are sandwiched between copper blocks and screwed together with brass screws, to provide a low electrical-resistance in the joint. A custom connector based off of Muething, Ihas & Landau (1997) is used on the 1st stage, to provide a demountable connection to the copper bus wires, and a similar joint is used on the 2nd stage, to allow the ADR to be removed for shipping.

The connector makes use of a cryo-clamp made of nylon that shrinks onto the fingers of a copper collet when cooled, which in turn presses on a copper ferrule thus ensuring good electrical contact for the joint.

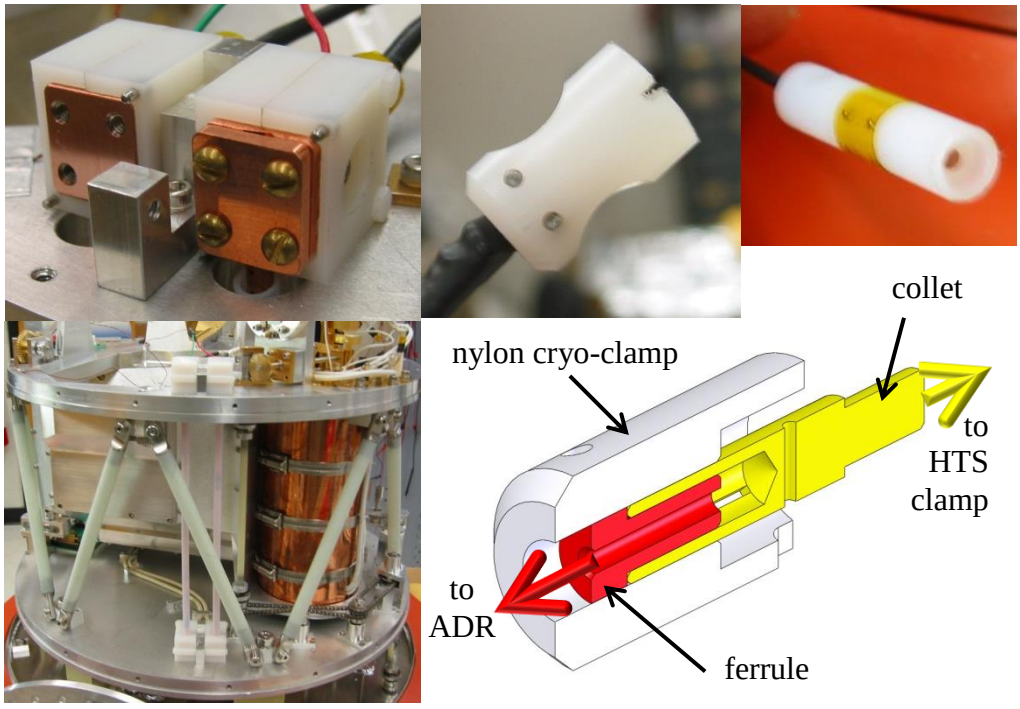

Figure 10: (clockwise from lower left) HTS leads carry ADR current from 1st stage base plate to the 2nd stage; close up of HTS copper clamps; 2nd stage custom connector; 1st stage custom connector; and section drawing of mated connector – when cold, the nylon clamps the collet fingers to the ferrule, reducing contact resistance.

2.2.4 *1st to 2nd heat switch*

During the initial cool-down it is useful to tie together the 1st & 2nd temperature stages to let both heat sinks of the cryocooler work in parallel. Given that the mass distribution of ZEUS-2 is biased towards the 2nd stage while the cooling power is biased towards the 1st heat sink, the option to temporarily connect the 1st and 2nd thermal stages improves cool-down and warm-up times, thus reducing overall turn-around time between cool-downs. When using the 1st/2nd

heat-switch cool-down time improves to 32 hours compared to 36 hours when left open. The 1st/2nd heat-switch is primarily made of aluminum to match the material of the 1st & 2nd stages and minimize strains due to differential contraction. High purity 1145 aluminum is used for the flex-vanes to provide high thermal conductivity at cryogenic temperatures. The switch is purely mechanical so that in the "off" position the stages are completely isolated and there is no heat leak from the 1st to the 2nd stage through the switch. A room temperature stepper motor drives the heat switch with the final set of gears providing a high clamping force of the 2nd stage cold finger via cam actuated clamps (Figure 11).

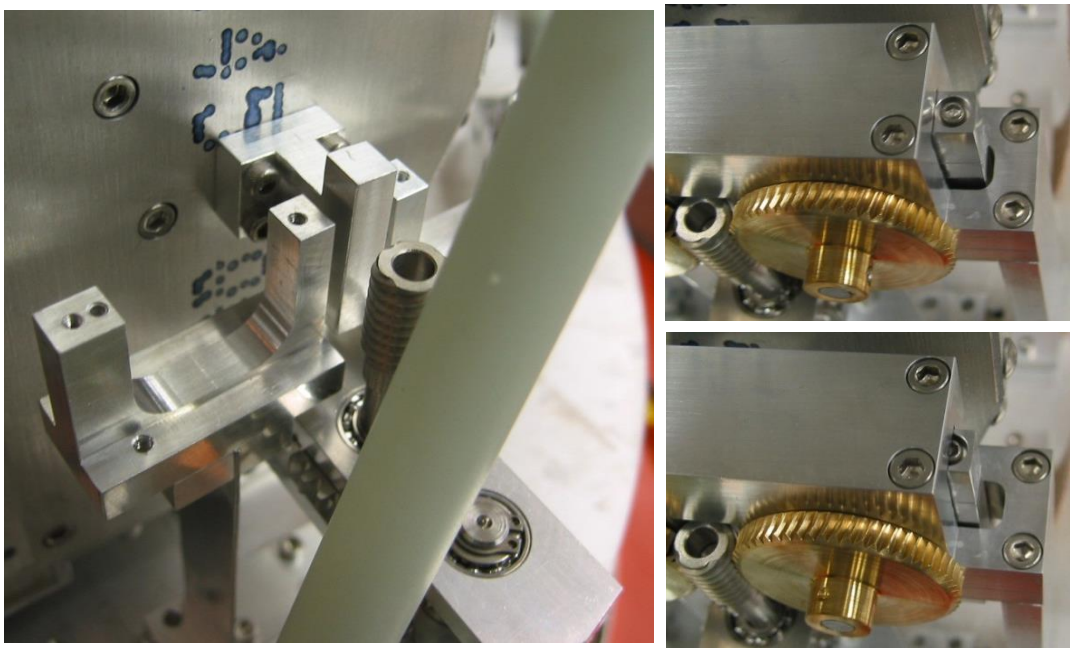

Figure 11: The 1st/2nd heat switch is only partially assembled (left) showing the cold finger sticking out from the 2nd stage baffling and the 1st stage clamps on top of the aluminum flex vanes sticking up from the base plate. When full assembled (right) the clamps ride on cams driven by worm gears to clamp (bottom) or unclamp the cold finger (top).

2.2.5 *Thermometry and Temperature Control*

Maintaining a constant bath temperature at the detector requires active temperature control of the ADR. Several temperature sensors come preinstalled on the ADR, including diode and

carbon resistor based sensors for monitoring the temperature of the magnet, and ruthenium oxide sensors to monitor the temperatures of the 3rd and 4th-stage salt-pills. Additionally, we have installed ruthenium oxide sensors from Lakeshore Cryogenics directly to the 3rd-stage thermal shield and detector-package allowing us to directly monitor the temperature of the detector-package. The sensors are readout using a custom thermometry box featuring 4-wire AC bridges for reading sensors on the 3rd and 4th stages, and 4-wire or 2-wire DC bridges for sensors on the 1st and 2nd stage. In all cases the measurement circuits produce a resistance proportional voltage that is digitized by a LabJack USB analog-to-digital converter. The LabJack also provides the digital-logic and analog-outputs necessary for full remote operation of the thermometry box as well as remote control of the ADR-magnet power supply. The latter is necessary for both remotely cycling the ADR as well as the active temperature control.

A LabView program interfaces with the LabJack for monitoring and logging of the temperatures and ADR magnet current. The program also applies the calibrations to convert the voltage of the thermometry box to temperatures. After completing an ADR cycle, the LabView programing provides a PID-servo control-loop for temperature control of the detector package. In the servo, the measured temperature of the detector is differenced with the desired temperature set-point, typically 120 mK, to determine the error signal. A proportional and integral gain is then applied to this error signal to determine the appropriate current necessary for a maintaining the set point-temperature of 120 mK at the detector. Performance is very good, with temperature stability better than the read-out noise of the thermometry system, ΔT_{noise} = 0.050 mK, over the entire seven hour hold time of the system.

2.3 *Optical Design*

The overall optical design of ZEUS-2 is very similar to ZEUS-1; however slight

modifications are made to accommodate the larger spatial and spectral footprint of the ZEUS-2 focal-plane arrays while maintaining image quality across the entire focal plane. The ZEUS-2 design also eliminates one mirror and enables the grating to tilt to a larger angle. The only optical element transferred from ZEUS-1 to ZEUS-2 is the grating, which is an R2 echelle blazed for 355 μm in 5th order (63.43º blaze angle, 992 μm groove spacing) providing a moderate resolving power ($R \equiv \lambda/\Delta\lambda \sim 1000$) that is matched to the broad lines ($\gtrsim 300$ km s^{-1}) of extragalactic sources. ZEUS-1 utilized only the 5th and 4th orders of the grating to access the 350 μm and 450 μm telluric windows respectively. ZEUS-2 will also employ the gratings 9th, 8th, 6th, 3rd, and 2nd orders to respectively access the 205, 230, 295, 625, and 850 μm windows once the 215/645 micron arrays are installed.

Figure 12 illustrates the ZEUS-2 optical design. From the telescope fore-optics an f/12 beam enters the dewar window (made of high density polyethylene, HDPE) and reaches a focus just inside the 4 K stage. It is then reflected off of flat mirror M1 onto collimating mirror M2 and through a Lyot stop to M3. The M2/M3 pair change the f/# of the beam from f/12—closely matching the telescope beams of APEX, CSO and JCMT—to an f/2.7 beam that matches our pixel size. M3 focuses the light onto the entrance slit of the spectrometer, from which it expands to fill the right half of the collimating mirror, M4, that creates a 10 cm collimated beam illuminating the 38 cm long grating. The dispersed light from the grating returns to the left side of M4 and then is reflected up to the flat pick-off mirror, M5, sending the beam to the focal plane. The mirrors and grating are gold-coated aluminum, all cooled to 4K. The optics are optimized to provide the largest field of view (~150 arcseconds) that the grating and instrument volume will allow.

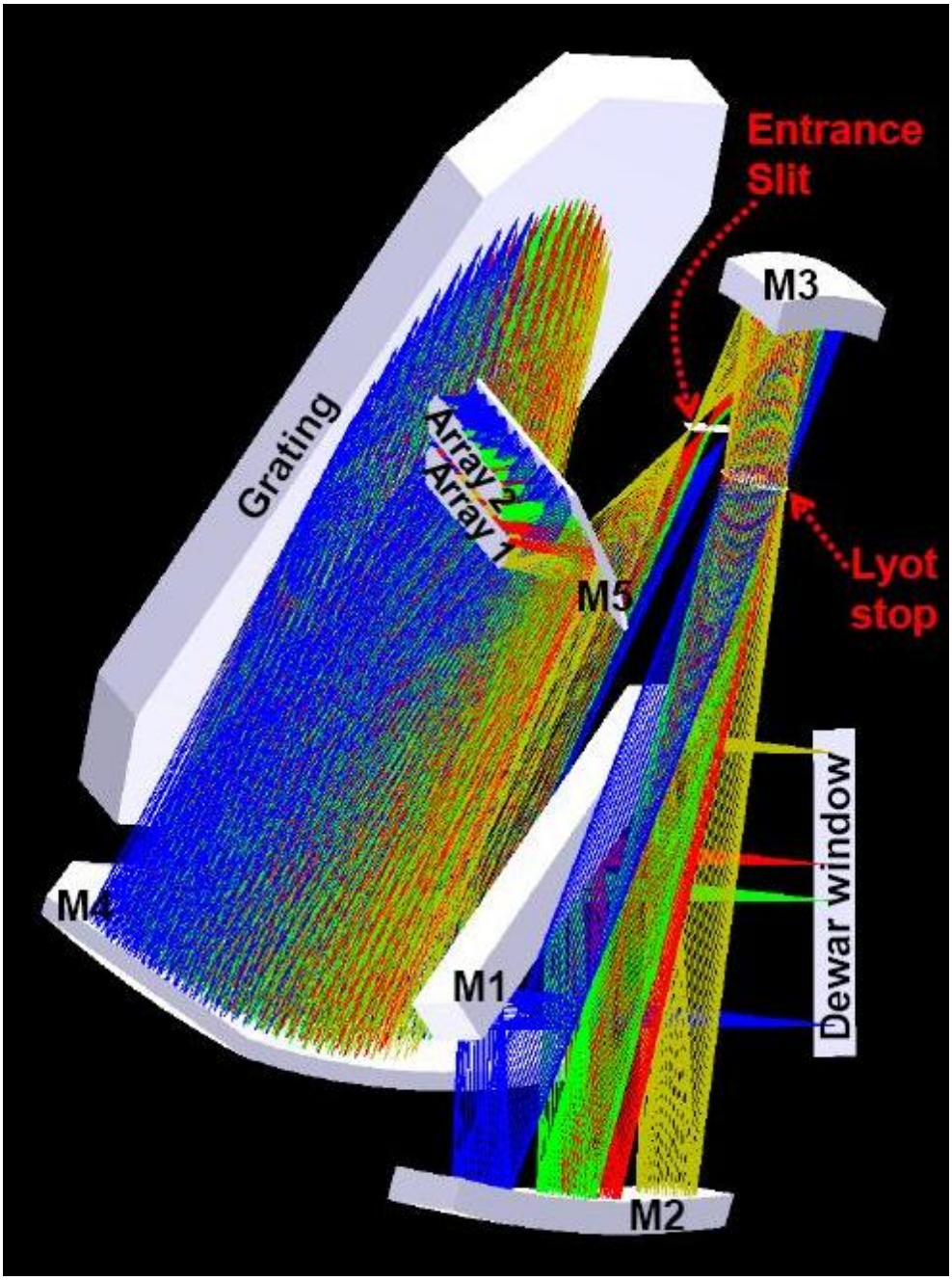

Figure 12: The ZEUS-2 optics ray-trace with 4 beams showing the spatial limits of the 400 μm (blue, green) and 215/645 μm (red, yellow) arrays.

Because photon backgrounds in a submillimeter spectrometer are quite small—only about 1 pW—great care is taken to both prevent out of band leaks and to intercept unwanted background radiation from within the instrument. This is primarily done using filters. A optical/near-IR scatter filter at 45 K is placed in front of the telescope focus, while a blocking filter (Zitex; Benford, Gaidis & Kooi 2003) and submm long plass filter are placed after the focus at 4 K. A second long pass filter is placed at the Lyot stop also at 4 K. Lastly, bandpass filters are mounted directly to the entrance of the detector package just above the focal plane on the milliKelvin-stage provide sorting of the grating orders. We typically split the 400 μm array with the filters so half of the detector operates in the 350 μm and the other in the 450 μm telluric windows. While splitting the 400 μm array lessens the instantaneous bandwidth by a factor of two, it enables simultaneous observations in both bands with still considerable bandwidth, ~2.5%, in both windows. Similarly, appropriate bandpass filters will allow operation in the 205, 230, 295, 625 or 850 micron telluric windows with ~2% instantaneous spectral bandwidth in each window when the 215/645 micron arrays are installed. The full telluric window is accessed by changing the grating angle, and hence the wavelengths falling on the detector, while observing. All of the longpass and bandpass filters are from Peter Ade's group at Cardiff University.

Besides filters, a submillimeter absorbing coating—in the form of black polyurethane paint (Aeroglaze Z306)—covers all baffles and mirror mounts to limit specular reflections that may hit the detector as well as absorb shorter wavelength radiation that can be scattered out of the beam by filters. The paint is mixed with carbon black to improve near and mid-IR absorption and silicon carbide beads are added to the surface to reduce specular reflection in the far-IR and submm bands (Smith & Howitt 1986). After priming, a coat of paint is applied to the surface.

While wet the surface is sprinkled with a layer of silicon carbide beads from a salt shaker, completely covering the surface. We found the above method provides a uniform, repeatable distribution of beads. Once the paint is set, a second layer of paint is applied, completely covering the beads. The second layer is allowed to cure before applying a thin over layer of Teflon spray as an anti-reflection coating (Smith 1986).

2.3.1 *Kinematic mounts*

The grating and detector-package are mounted kinematically for ease of assembly and reproducibility in optical alignment. Given that the instrument is assembled upside down from its operating orientation, both mounts utilize springs to ensure proper seating and to prevent displacement when the instrument is rotated. Variability in the optical alignment due to removal of the grating or detector is well below our pixel size (~ 1 mm) even after shipping to and from a telescope. Both mounts feature a small copper thermal-link between the mount and the 4 K base plate to improve the cool down characteristics since the line or point contact through the stainless steel joints we use in the mounts result in very high contact resistance.

2.3.1.1 Grating mount

To allow the desired wavelength of observation to fall on the detector we must change the tilt of the grating. This requires a grating mount that allows the grating to pivot at its center—corresponding to the center of the collimated beam—while constraining motion of the other axes. To achieve this ball sockets attached to the grating side arms, which are in turn bolted to the grating, are captured in cone-and-V or V-and-V pockets (Figure 13). Shoulder screws are used with wave-washers to preload the joint and to guard against over tightening. The shoulder screws bottom out before the top V-block clamps on the ball. PTFE tape is inserted between the socket and pocket to reduce friction.

This mounting allows for one-degree of freedom, i.e. the grating tilt, while constraining the remaining five degrees of freedom without stressing or over constraining the grating. The ball-cone connection fixes one side of the rotation axis while the ball-V connection, on the other side, sets its direction and allows for thermal contraction along the axis. The rotation axis is allowed to turn on the ball-PTFE-pocket joints. The mount also allows differential movement along the rotation axis between the grating and the base plate preventing the buildup of stress in the grating during cool-down or warm-up due to temperature gradients across parts. A constant-force spring is attached the back of the grating to reduce backlash in the grating rotator drive system, which is remotely driven by a stepper motor.

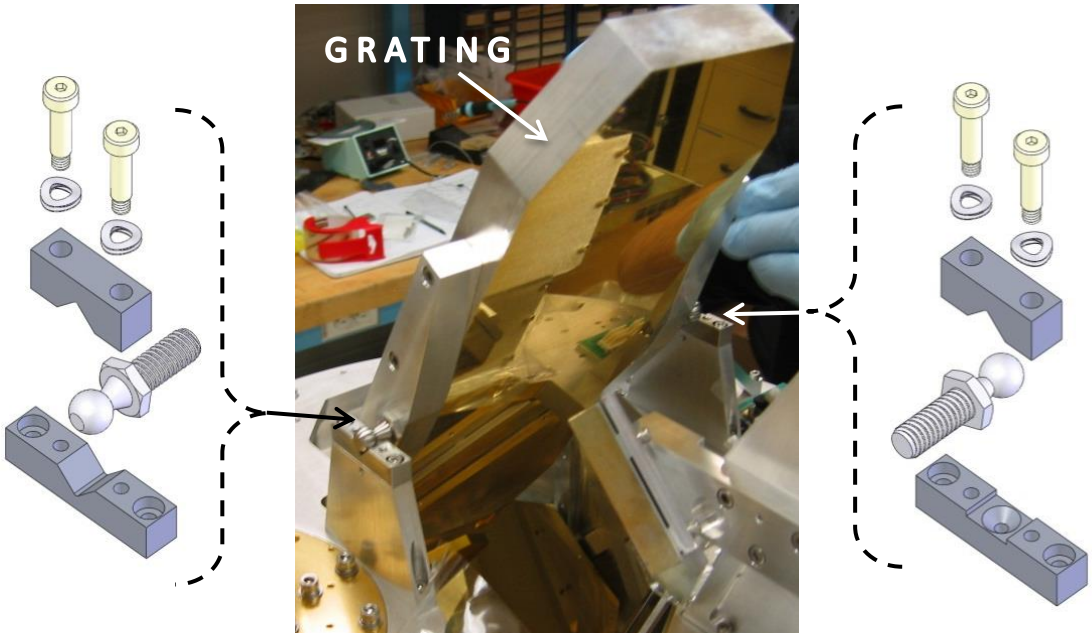

Figure 13: A picture of the grating mounted in ZEUS-2 with V blocks removed (center). An exploded diagram of the left and right mounting structures showing the V-ball-V joint (left) and the cone-ball-V joint (right), respectively, allowing grating rotation.

2.3.1.2 Detector-package mount

Unlike the grating mount, the detector-package mount requires all degrees of freedom to be constrained. To protect the Kevlar in the milliKevlin structure and focal plan arrays we remove the detector-package assembly for shipping. We also need to be able to remove detector-package for testing, upgrades, and filter changes. All of which benefit from a simple, reliable, and repeatable mounting scheme.

The full detector-package assembly (see Figure 7) is simplified to a flat plate with the center of mass located beyond the plate's footprint. The plate uses ball sockets to mate with a cone, V-slot, and plane in the classic 3-point kinematic mounting scheme (Figure 14). To counteract the center-of-mass torque and to retain the mount when it is in its operational orientation (i.e. upside down from assembly), a screw and conical spring stack are used to provide a preload and maintain contact on all three balls. The fixed plate can be shimmed to obtain a good optical alignment and then locked down ensuring alignment is maintained over repeated installations of the detector-package.

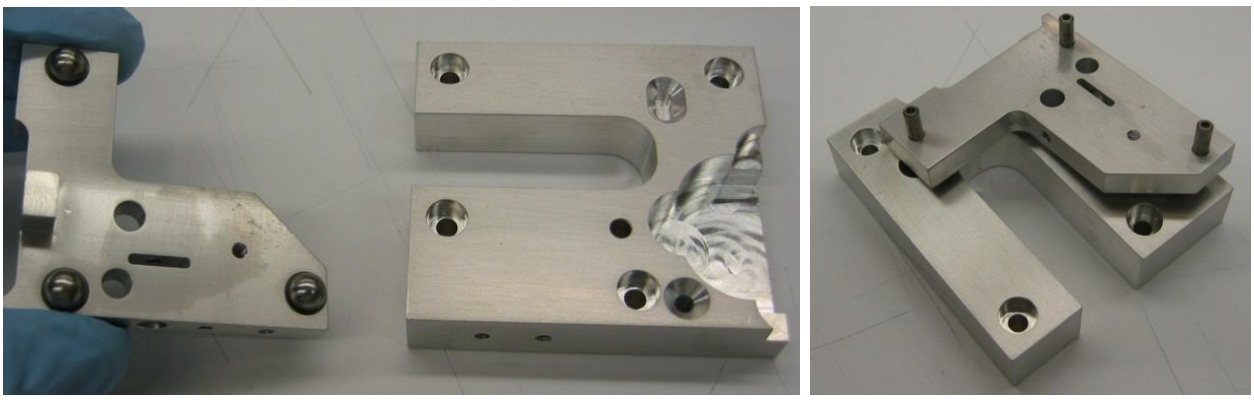

Figure 14: The two halves of the kinematic mount for the detector package showing the three ball sockets, the mating surfaces on the fixed-plate (left), and the assembled mount (right) where one can see there is access to the fixed plate counter-bore holes for shimming.

2.4 *Detector*

The focal plane of the ZEUS-2 detector is segmented into three arrays with optical back-shorts optimized for 215, 400 and 645 μm wavelengths. The arrays are read out using superconducting quantum interference device (SQUID) multiplexors paired with the room temperature Multi-Channel Electronics (MCE). Figure 15 shows the detector layout and how it enables the simultaneous observation of five important submillimeter emission lines from extended, nearby sources. Below we describe the physical, optical, and thermal designs of the arrays.

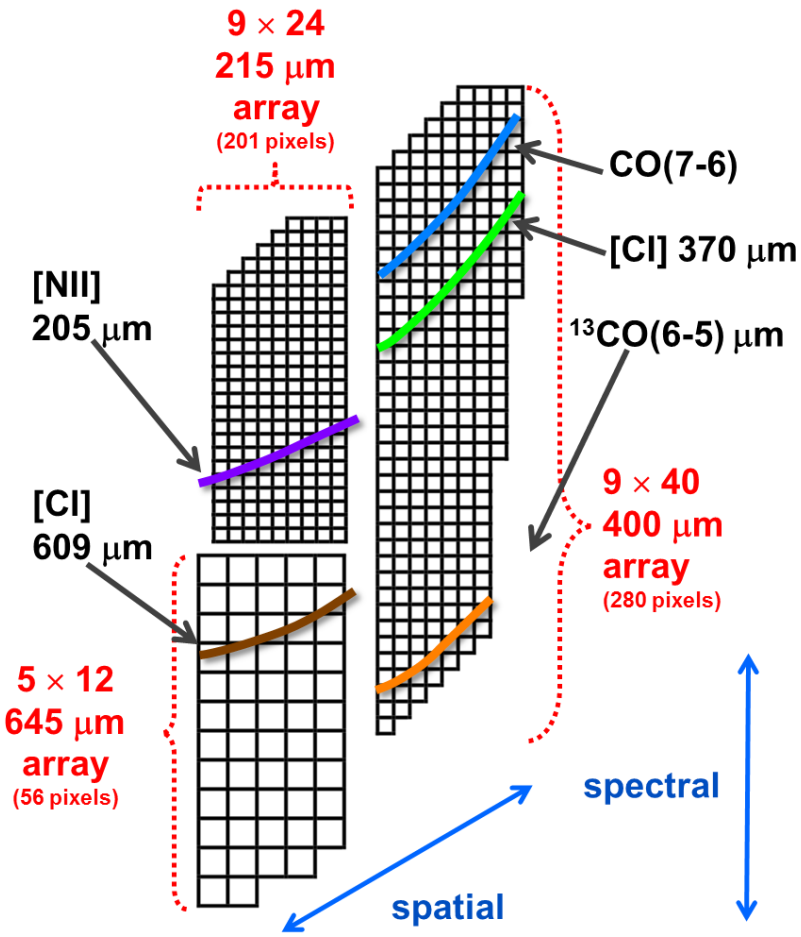

Figure 15: Schematic of ZEUS-2 arrays showing simultaneous detection of 5 important spectral probes.

2.4.1 *Array Design*

The ZEUS-2 arrays are transition-edge-sensed bolometers from the Quantum Sensors groups at NIST Boulder. The arrays are manufactured on two silicon wafers with the 400 μm array on one, and the 215 and 645 μm arrays sharing a second. The usable field-of-view in the focal-plane is ~26 mm (spatial) x 57 mm (spectral), which is split roughly equally between the 400 μm and 215/645 μm arrays. The pixel sizes of each array are respectively 1.26, 1.06, and 2.06 mm square for the 400, 215, and 645 μm arrays. The two shortest wavelength arrays feature a 0.14 mm structural/optical gap between each pixel while the longest has a 0.2 mm gap. Given that the final f/# = 2.75, the pixel sizes correspond to 1.15 λ/D pixels for the 400 μm and 645 μm arrays. The 215 μm array pixels, however, are slightly oversized (1.8 λ/D) to compensate for point source flux that would be lost with diffraction limited pixels on the Atacama Pathfinder Experiment (APEX) due to the surface roughness (18 μm rms) of the primary dish. The larger pixels also make pointing easier than it would be if we used a 4.4" diffraction limited beam.

The array format (spatial x spectral) of the 400, 215, and 645 μm arrays are 9 × 40, 9 × 24, and 5 × 12 pixels respectively. The actual array designs have the corner pixels cut-out (as can be seen in Figure 15) so that the total pixel count is 537. These cut-outs provide space for handling the arrays, improved structural stability, and bond-pad placement. We have minimized the impact of the cut-outs by having them follow the angle of the spatial field with respect the spectral direction. Additonally the poor image quality in these areas would have significantly reduced their performance so that little science is lost by eliminating these pixels.

The best sensitivity in a detector is achieved by detecting the highest fraction of the incident photons, quantified by the detective quantum efficiency (DQE). To achieve an high DQE all of the ZEUS-2 arrays feature a tuned backshort and palladium-gold mesh absorber. The

use of the mesh absorber is important as it allows for a high absorptive efficiency while adding very little to the heat capacity of the pixel. This is important if one wants to reach a low noise-equivalent-power (NEP) while still maintaining a reasonable detector time-constant (< 10 msec).

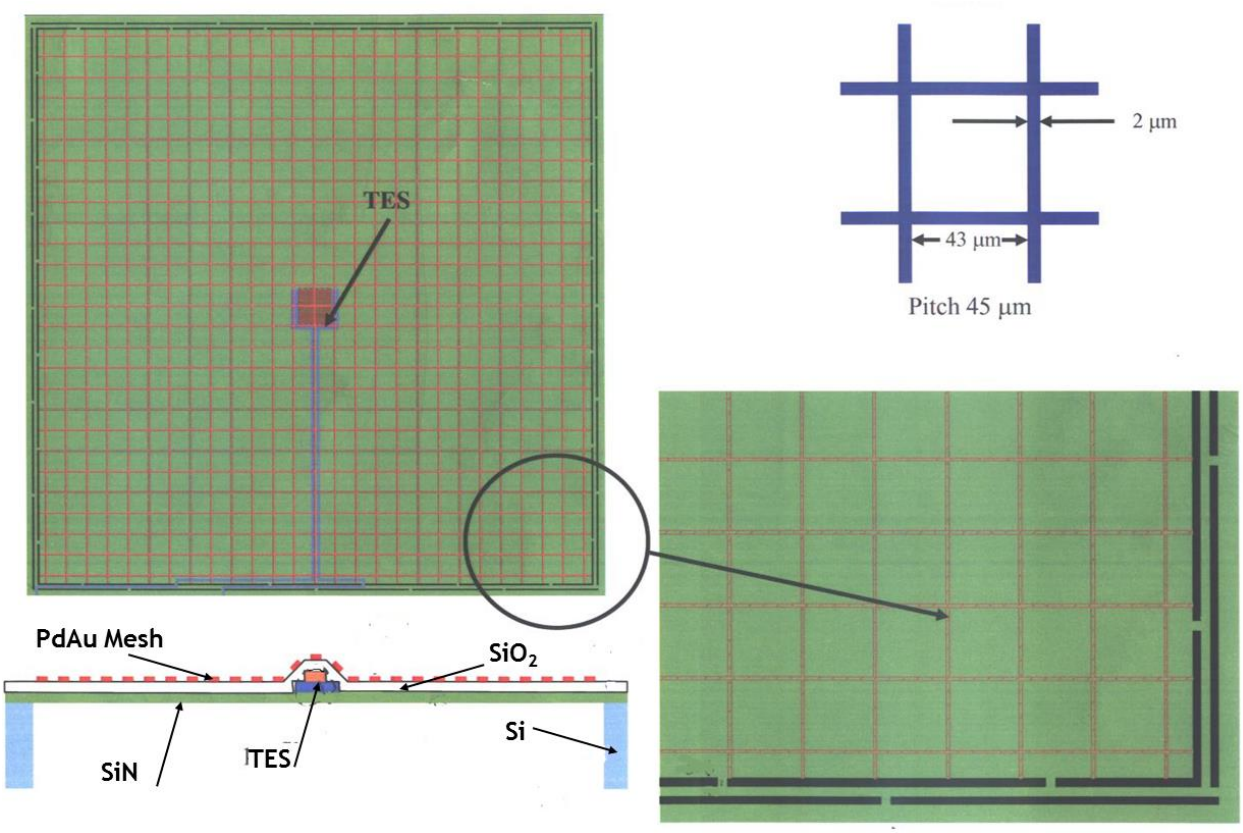

Figure 16: Bolometer design for the 400 micron array. From the upper-left moving clockwise; 1.4 mm x 1.4 mm pixel with TES and mesh, PdAu mesh design, close-up of leg structure, and profile view of the bolometer.

2.4.1.1 400 µm Array Design

With a quarter-wavelength backshort the 400 µm array operates with better than 90% DQE in both the 350 and 450 µm bands. Modeling of the absorber at NIST Boulder provided straight forward mesh designs for this array as seen in Figure 16. As the 350 and 450 µm bands are

ZEUS-2's primary bands, we have implemented the 400 μm array first and successfully made a first light observation of a high-z galaxy on APEX in November 2012 (see Chapter 3). Section 3 below compares our predicted performance to the on-sky performance of our first light observation.

2.4.1.2 215/645 μm Array Design

The backshort on the 215/645 μm arrays is a quarter-wavelength at 645 μm. The 215 μm uses this same backshort, since it shares same wafer as the 645 μm array, and is equivalent to three-quarters of a wavelength at 215 μm. We expect that both arrays will see DQE > 90% at their band centers (i.e. 215 and 645 μm) while the long wavelength array has an expected DQE of only ~78% at 850 μm. Modeling of the absorber at NIST Boulder has provided straight forward mesh designs for the longer wavelength array, but the 215 μm array required a more complex design. The final design features a mesh with 2 μm lines on a 42 μm pitch made of 12 Ω/square PdAu film giving an effective sheet impedance of 264 Ω/square—close to the ideal impedance of free space, 377 Ω/square. By adding a capacitively coupled square ring to each hole in the mesh, the sheet impedance better matches free space as well as removes parasitic reactance. The result is a device with less than 3.2% reflection losses (Figure 17). Production of the 215/645 μm arrays is occurring now and we expect integration of the arrays into ZEUS-2 to be complete during the first half of 2014. Details of the performance and first light observations with the 215/645 μm arrays will appear in a future publication.

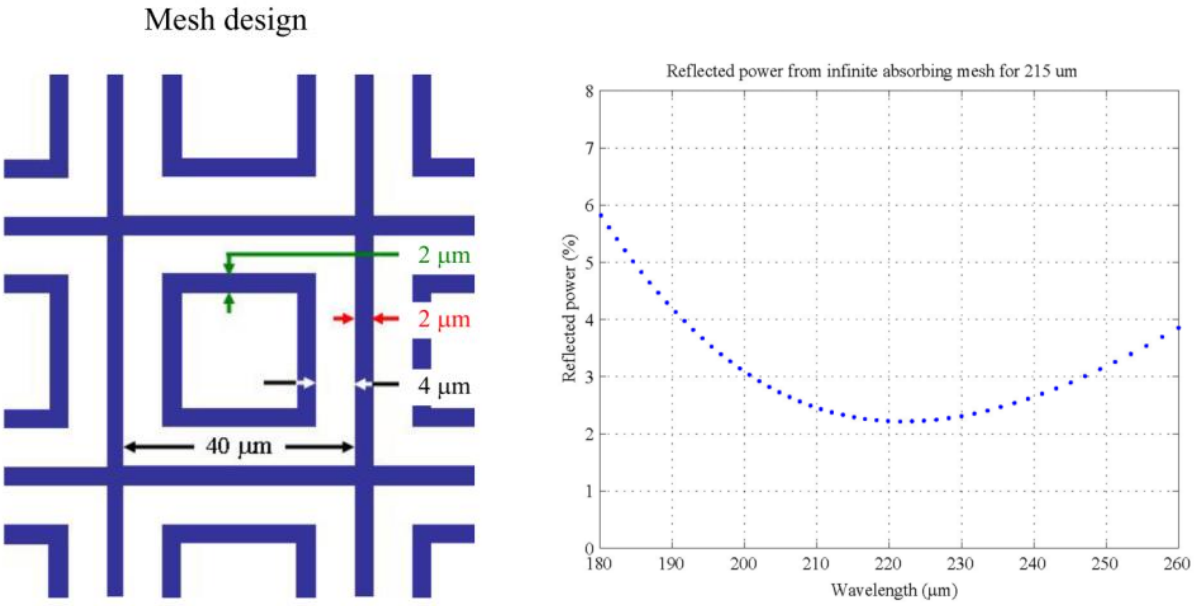

Figure 17: The PdAu mesh absorber design (left) and expected reflected power (right) for the 215 µm array.

2.4.2 *Detector Package Design*

Developing a detector package that fits within the ZEUS-2's detector-package envelope yet fulfills the electronics requirements of the detector technology proved to be quite challenging. In addition to the three bolometer arrays, the detector package must house the terminating connectors for the readout electronics, twenty multiplexing chips, twenty interface chips for voltage biasing the pixels, and a superconducting interconnect between the arrays and interface chips. Typically aluminum wirebonds are made directly between TES arrays and their interface chips, however the density of the ZEUS-2 bondpads on the arrays necessitated a fan-out. Further complicating the detector package design was the travel of the grating rotation, which limited the distance the detector-package could extend towards the grating.

A novel solution presented itself however; separate the arrays and mount the 400 µm array and 215/645 µm arrays on separate halves of the detector package. We mount the 400 µm array

to front half of the package so that the array is back-illuminated while the 215/645 μm arrays are front illuminated and mounted to the back half. This creates separate front and back focal planes that are then sandwiched together as in show in Figure 18. This design has the added benefit of enabling ZEUS-2 to be easily operated with only one array installed or with two of the same type. With two of the 400 μm arrays installed, ZEUS-2 could observe ~20 spatial positions on the sky in the 350 and 450 μm bands. The arrays can also be easily swapped in and out for troubleshooting and upgrading of the bolometers. Even with the detector sandwich design, space was still tight; as such the detector package is designed to fully utilize the available space envelope, resulting in a very irregular shaped package.

The arrays and detector electronics are housed in a copper box for good thermal sinking. Each half of the copper box features a PCB board that providers interconnects between the MUX chips and the cabling that goes to electronics at 4-K as well as ten MUX and interface chips, and a silicon fan-out board. That last provides a superconducting connection over niobium traces between the array and the interface chips. The arrays, with gold-coated back shorts, are mounted to the copper box with spring clips. A gold coated silicon frame between the 400 μm array and box ensures that the array does not experience excessive thermal stress. The backshort of the 215/645 μm array fulfills a similar purpose since the array is front illuminated and rests ontop of its backshort unlike the 400 μm array where the backshort rests ontop of the array. Good thermal conduction to the arrays is provided by gold wire bonds between the copper box and the gold bond pads on the arrays. Aluminum wirebonds proved all of the electrical connections between the various components.

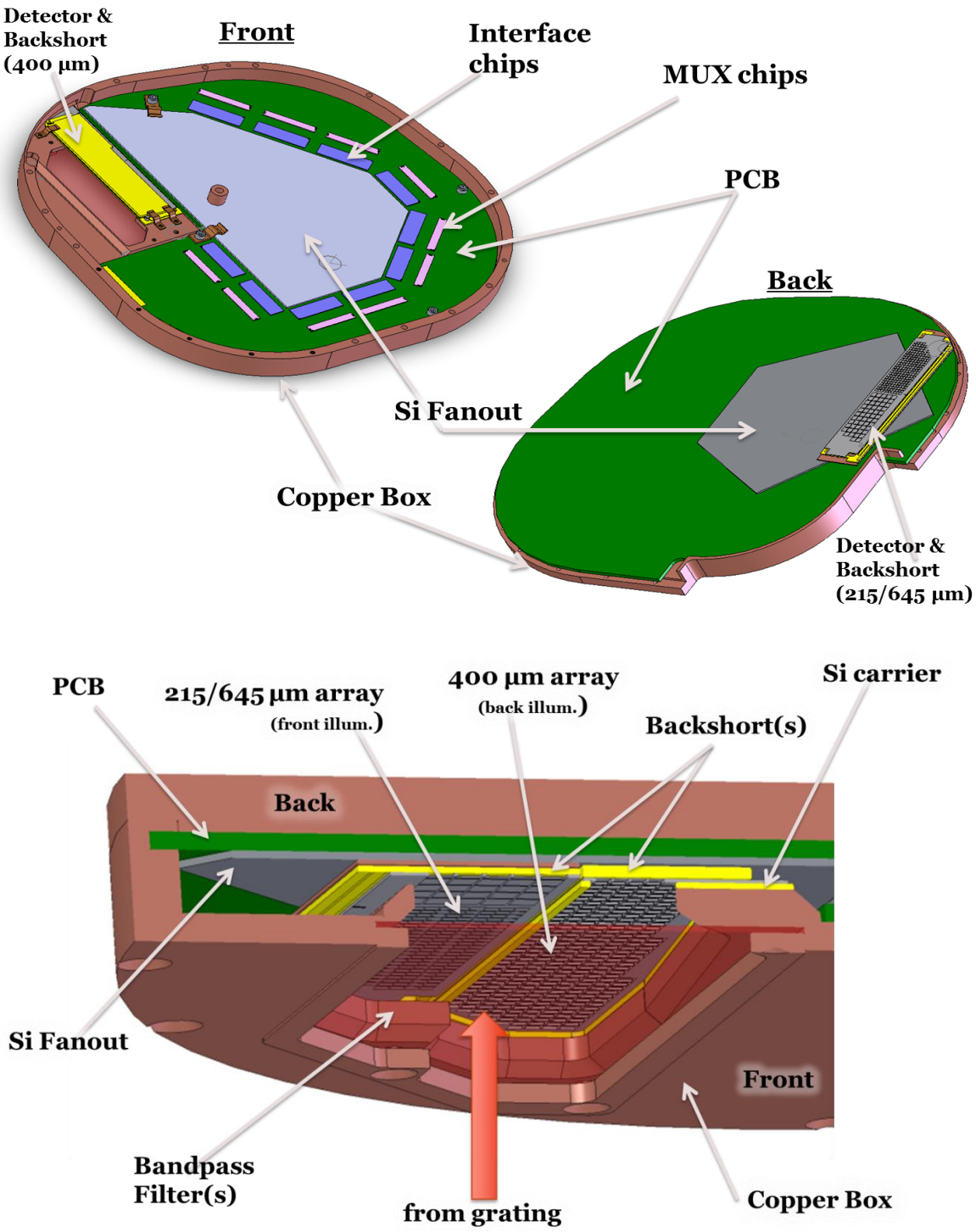

Figure 18: (top left) Front-half of the detector package for the 400 micron array. (top right) The back-half of the detector package for the 215/645 micron array. (bottom) A cut-away view of the assembled detector package. In all images: brown is the copper box, light-blue is the silicon fan-out board, dark blue are the interface chips, light purple are the MUX chips, and yellow are the gold coated backshorts and silicon carriers.

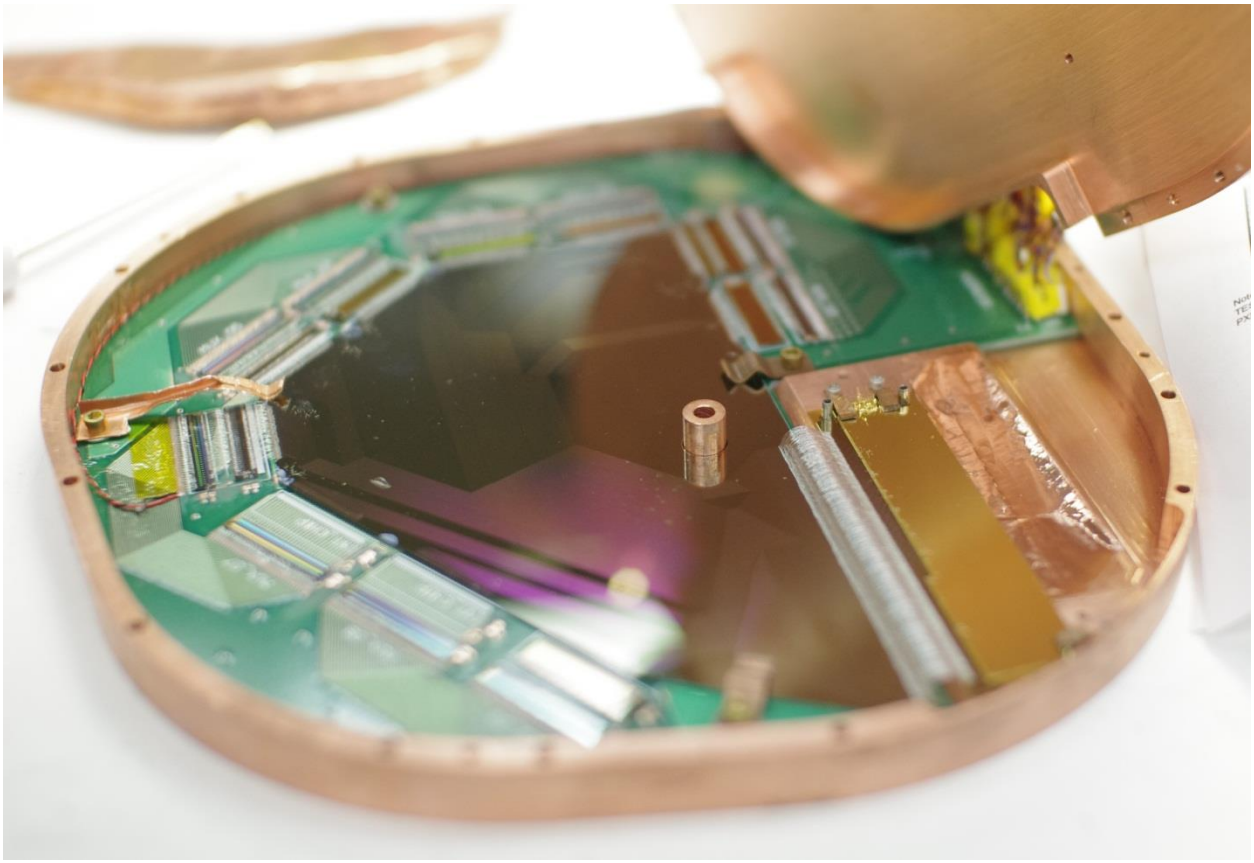

Figure 19: The assembled 400 µm detector-package filling the front-half of the focal plane sandwich. The array is underneath the gold backshort on the right side of the image.

2.5 *Magnetic Shielding*

SQUIDs are extremely sensitive to magnetic fields so adequate magnetic shielding is required to reduce magnetic-noise picked-up by the SQUIDS and to ensure that the fields are below the SQUID saturation point. ZEUS-2 uses a high-permeability shield (Amumetal – Amuneal Mfg. Co.) just inside the vacuum shell to shield against fields sourced externally. Inside the dewar the ADR is designed with several shields that significantly attenuate the field when the ADR magnet is in operation. However, additional shielding is needed for the SQUIDs

to remain functional. All SQUIDs, including the entire detector package, are housed in a A4K (Amuneal Mfg. Co.) shell surrounded by a superconducting niobium shell. This combination creates an essentially zero-field cavity around the SQUIDs once the niobium reaches it transition temperature of 7K, and as long as the magnetic field remains below ~2000 Gauss, the critical field strength of niobium (see Figure 20).

2.6 *Detector Readout Electronics*

2.6.1 *MilliKelvin Electronics*

ZEUS-2 utilizes the three stage time domain SQUID multiplexed readout system developed at NIST Boulder (De Korte et al. 2003). Figure 21 illustrates the detector readout chain. Each TES bolometer is coupled to one of the inputs on a 32-row SQUID multiplexor (28 rows on 20 MUX chips are used in total). The multiplexors are housed in the detector package with their 1st stage SQUIDS (SQ1) serving as row selectors. Their output is coupled to the 3rd stage SQUID series arrays (SA) via a 2nd stage SQUID (SQ2) serving as the column readout.

Figure 20: (top) 4-Kelvin PCB for SQUID Series Arrays and MCE-connector to detector fan-out board, and example Series Array modules. (bottom right) The detector package magnetic shielding. (bottom left) The room temperature Amumetal magnetic shield.

2.6.2 *4-Kelvin Electronics*

The detector package is connected to a 4-Kelvin printed circuit board (4K-PCB) via copper-clad NbTi twisted pair TekData cables. The SQ2 to SA interconnect uses two twisted pairs for each column to ensure that the inductance of that connection is not so high that it would limit the multiplexing rate. The 4K-PCB houses the SAs that amplify the detector signals by a factor of 100 before passing them over twisted-pair copper wires in four TekData cables to 100-pin MDM connectors mounted on the dewar shell.

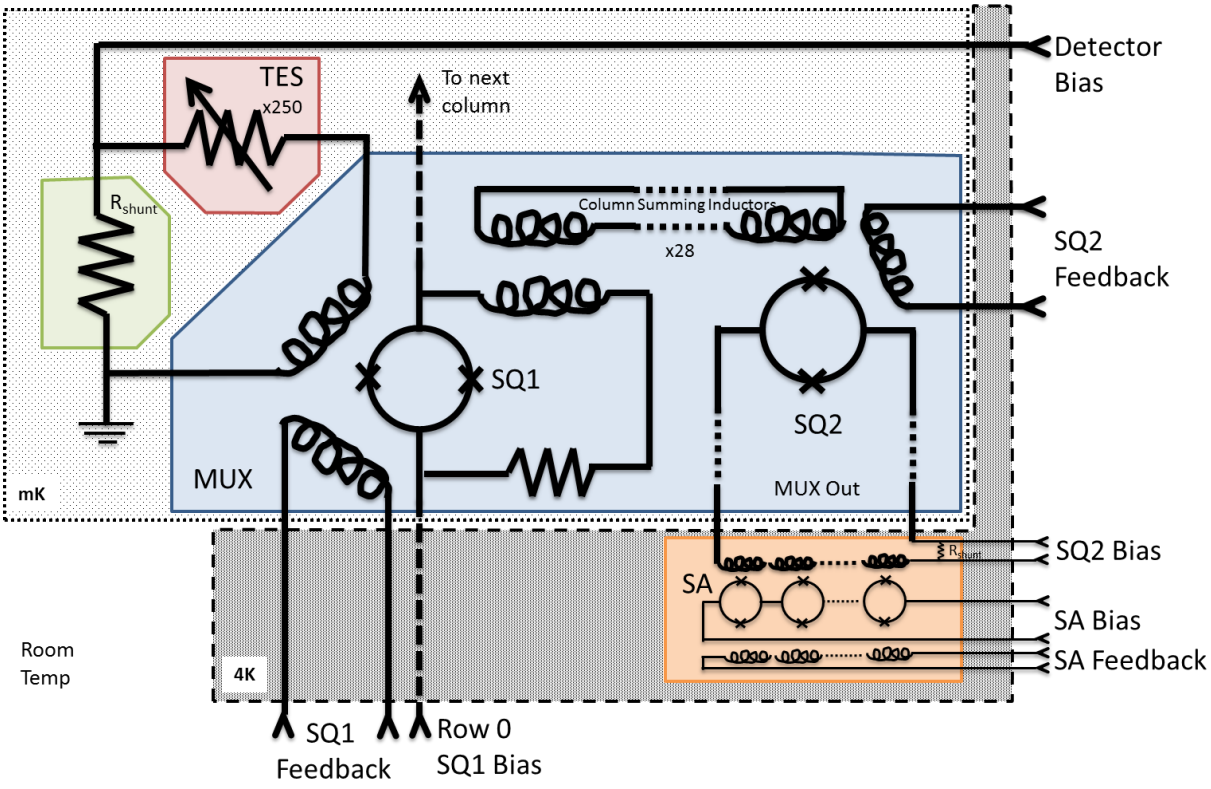

Figure 21: ZEUS-2 electronic schematic for one pixel, i.e. one multiplexor row and column. Colors denote the different chips: red is the array, green the interface chips, blue the SQUID multiplexor, and orange the SQUID series array. Everything in the light gray box is at milliKelvin temperatures in the detector package, while the dark grey is located on the 4 K temperature stage. Outside either box denotes room temperature. All wiring to the milliKelvin first passes through the 4K-PCB and is then thermally sunk at 1.5 K before reaching the milliKelvin stage(not shown). At room temperature all wires start and terminate inside the MCE. When the MCE is in servo mode the output (i.e. the science signal) is the voltage input into the SQ1 Feedback.

2.6.3 *Multi-Channel Electronics (MCE) and Control Software*

Because of the SQUID sinusoidal response to a linearly changing input signal, an active feedback scheme must be used to ensure the SQUIDs are operating in their linear regime. ZEUS-2 uses the Multi-Channel Electronics (MCE) developed for SCUBA-2 by Mark Halpern's group at the University of British Columbia (UBC) to provide the active feedback (Battistelli et al. 2008). The MCE also provides the SQUID bias to power each stage of SQUIDS, the passive feedback for the SQ2 and SA, the SQ1 biases serving as row addressing and the TES biases. The MCE reads the TES response by using a PID control-loop to servo the SQ1 feedback, canceling any change in the current through the TES as sensed through the SQUID readout chain and keeping the SA output constant. It is the SQ1 feedback that is then the TES response and indicates the power incidence on the bolometer. The MCE is mounted directly the ZEUS-2 dewar (see Figure 1) and mates to four 100-pin MDM connectors on the dewar shell.

The MCE is controlled via a fiber connection by a computer running Linux. UBC provides an extensive suite of low-level tools for running the MCE. We have incorporated these tools into a GUI program for easy operation at the telescope. The program also communicates with the telescope systems for obtaining information like the atmospheric transmission and to control the chopping and nodding. Since we observe in chopping mode, we perform a synchronous detection of the time series data using a reference signal from the secondary mirror that is sampled using the "Data_Valid" fiber connector of the MCE clock-card and custom clock-card firmware. When observing science sources we readout the detector at 400 Hz and take 16000 samples (40 seconds) for each plus or minus beam on the sky. A complete integration might typically include 32 beams, for a total of ~21 minutes.

3 SENSITIVITY AND PERFORMANCE

3.1 *In Lab Performance*

Several cool downs were performed to characterize the performance of the 400 μm array. Current versus voltage (IV) curves of the bolometers were taken with the array un-illuminated to determine the saturation power, thermal conductance, and transition temperature of the array. The transition temperature is ~170 mK and thermal conductance ~100 pW/K. At an operating temperature of ~100 mK the saturation power was greater than 2 pW, twice that required to ensure that the bolometers do not saturate due to sky emission. In fact, most pixels in the array are fully functional, with reasonable overhead, up to a bath temperature of 120 mK. This fact is important as operating the system at a high temperature can result in a significantly longer hold time for the ADR. In the next section we summarize the method for characterizing a TES bolometer array. For a detailed discussion of TES bolometers and theory of their operation see Irwin & Hilton (2005).

3.1.1 *Detector Characterization*

3.1.1.1 Thermal Conductance and Saturation Powers

The primary method for determining the thermal properties of a TES bolometer is to measure the current through the TES as a function of bias voltage, i.e. IV curves. For a TES we start at high bias voltage so the TES is normal, and ramp the bias down through the TES's superconducting transition and finally to its superconducting branch (see Figure 22).

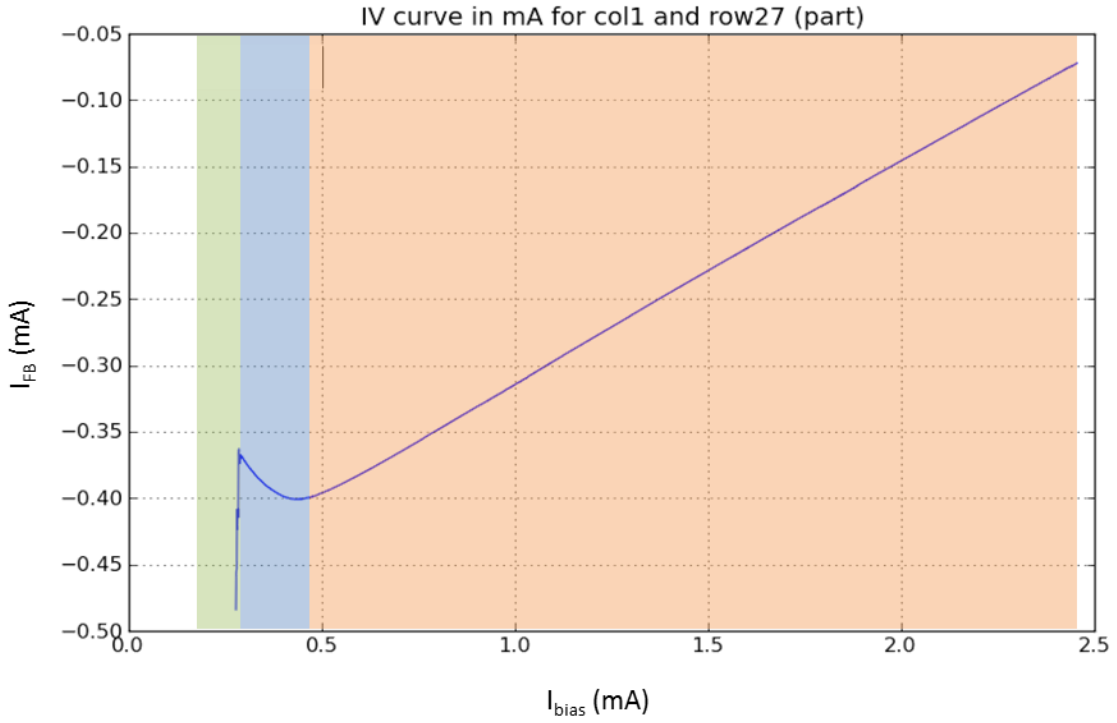

Figure 22: IV curve for a ZEUS-2 bolometer. The y-axis is the current though the SQ feedback coil and proportional to the current through the TES. The x-axis is the current through the TES shunt resistor, and is proportional to the voltage across the TES. The normal (orange), transition (blue), and superconducting regions (green) are indicated.

The TES bias voltage is known since it is set by the voltage bias output, V_{bias}, of the MCE and resistances of the TES bias line, R_{bias}. The current through the TES is measured by the SQUID readout chain and is in terms of the first stage squid feedback voltage, V_{FB}. It is necessary to convert both of these values to the local currents through and voltages across the TES, I_{TES} and V_{TES} respectively. The bias voltage and feedback voltage are first converted to a bias current and feedback current using.

$$I_{bias} = \frac{V_{bias}}{R_{bias}} \quad (1)$$

$$I_{FB} = \frac{V_{FB}}{R_{FB}} \qquad (2)$$

Where R_{bias} = 587 ohm and R_{fb} =5280 ohm, the bias of the feedback line. The TES current is then

$$I_{TES} = \frac{(I_{FB} - I_{offset})}{M_{ratio}} \qquad (3)$$

Where M_{ratio} = 9, is the ratio of the inductance of the TES input coil to the inductance of the feedback coil in the SQUID multiplexors. I_{offset} is the current offset of the 1st stage SQUID which is determined by fitting a line to the normal branch of the IV curve and finding the y-intercept of that line. This is done by first searching the IV curve for the end of the transition region (which is marked by a very large slope as the TES becomes superconducting or the feedback servo unlocks), then finding the minima which occurs at higher bias and fitting between these point. Next, the V_{TES} is determined by

$$V_{TES} = R_{shunt}(I_{bias} - I_{TES}) \quad (4)$$

R_{shunt} = 0.18 milliohm and is the TES shunt resistance for our interface chips. Once both the TES current and voltage are determined several important derived quantities and diagnostic plots can be determined. The normal resistance of the TES, simply the slope of the IV curve at the highest bias voltages is one. The power dissipated in the TES via Joule heating is simply $I \cdot V$. When normal, the TES behaves ohmic with the resistance of the TES constant, but on the transition of

the TES when the resistance is changing, the bolometer enters a constant power regime. If the detector is dark when the IV curve is obtained, then the only power dissipated into the bolometer comes from the TES bias, and is equal to the total saturation power—the maximum optical power the bolometer can see and still be operable at the bath temperature the data were obtained.

Taking IV curves at several bath temperatures (Figure 23) allows us to determine the thermal conductance of the bolometers by fitting plots of the saturation power, P_{sat}, versus bath temperature, T_{bath}, to :

$$P = K({T_c}^n - {T_{bath}}^n) \qquad (5)$$

Where *K*, and *n* are fit parameters. The thermal conductance, G, as discussed in Hilton & Irwin (2005) is then

$$G = nK{T_c}^{n-1} \qquad (6)$$

Another important plot is the TES's percent of normal resistance, $\%R_n$, versus the TES bias, V_{bias}, used for picking the appropriate bias during observations to maximize the response of the bolometers (Figure 24). The thermal properties of the bolometer combined with the TES being biased with a constant voltage causes the pixels to experience a negative electrothermal feedback. This means a change in incident power causes an increase in temperature of the bolometer that in turn increases the resistance of the TES. Since the TES has a constant voltage bias, the increasing resistance causes the current through the TES to go down in turn causing a drop in the amount of Joule heating and forcing the TES back to its starting resistance. This behavior has a couple of important implications. At steady-state the TES will always have the same resistance, set by the bath temperature and TES bias voltage, regardless of the incident optical power as long as the optical power is less than the bolometers saturation power. Second, the current through the TES is inversly proportional to the power incident on the bolometer, a

fact we use to detect submillimeter photons. Lastly, in the small signal regime, i.e. small changes of incident power, the responsivity of the bolometer, like all systems featuring negative feedback, does not depend on the intrinsic properties of the system (i.e. the bolometer), but depends only on extrinsic values. In this case it is the TES bias voltage. For optimal performance we want to use a TES bias that will result in an TES operating resistance that is small as possible compared to its normal resistance, without the TES transitioning to its superconducting state. An operating point of ~30% of the normal resistance is picked so that we maximize the responsivity of the bolometers, while also maximizing the number of pixels that are operational.

As you might expect, large signals that are on the order of a few-precent of the bolometer saturation power, such as changes in the optical load from the sky emissivity or grating efficiency, can drive the bolometers from their ideal operating point. To account for these changes, IV curves must be taken anytime there is a large change in optical power and a new bias voltage picked that keeps the TES at 30% of their normal resistance. The MCE includes software routines that automate this process allowing us to quickly take IV curves (~5 mins.) after large slews of the telescope, changes in the grating tilt, or long periods of time (~60 minutes) and analyzed to pick a new ideal bias.

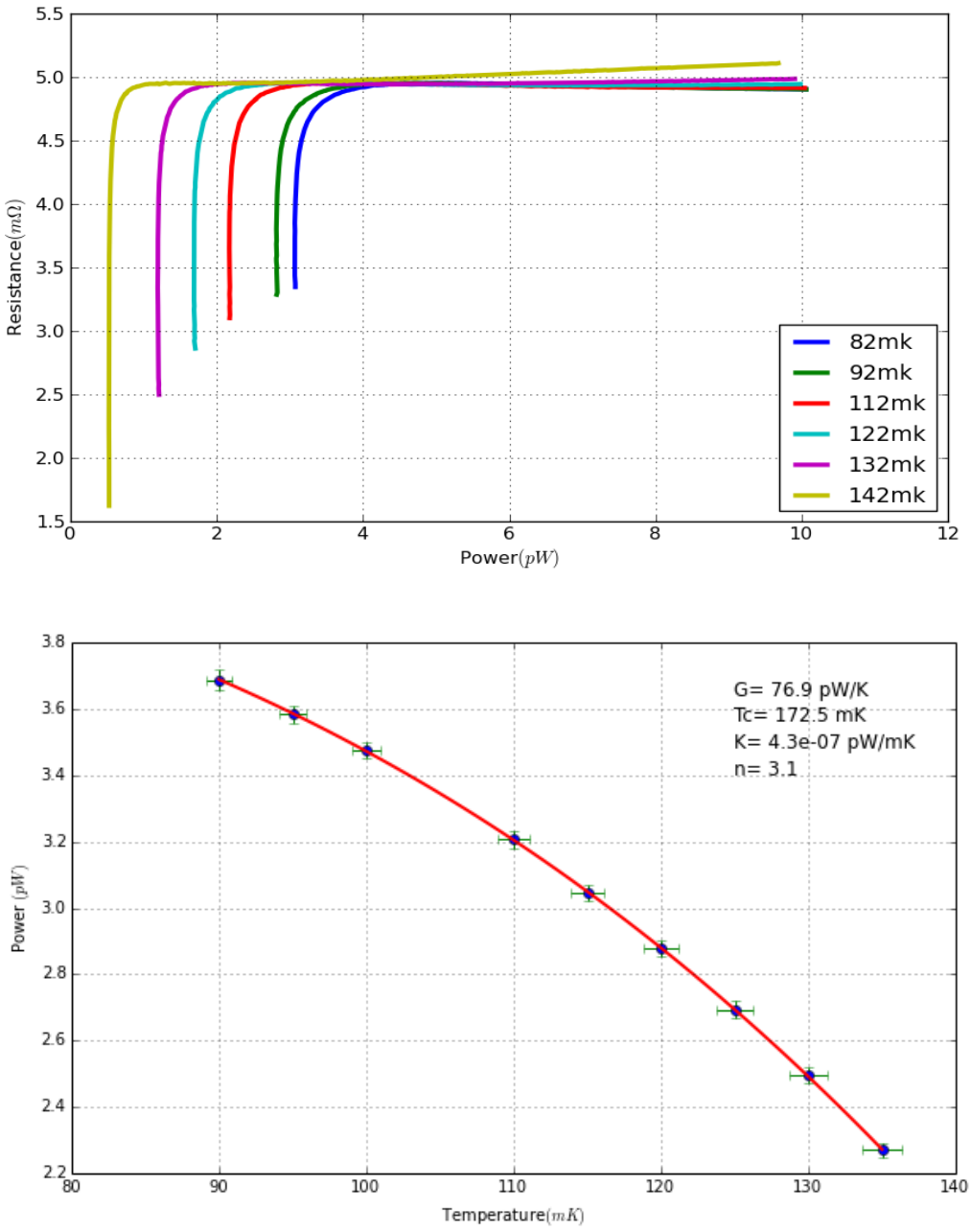

Figure 23: (top) Plot of the resistance of the TES as a function of the power dissipated in the TES for different bath temperatures and no optical loading. The power dissipated is constant when the TES is in its superconducting transition, and is equal to the saturation power of the bolometer at a given bath temperature. (bottom) A representative plot of the saturation powers versus bath temperature for a bolometer in the 400 μm array fit to Equation 5 (red line) to determine the thermal conductance of the bolometer.

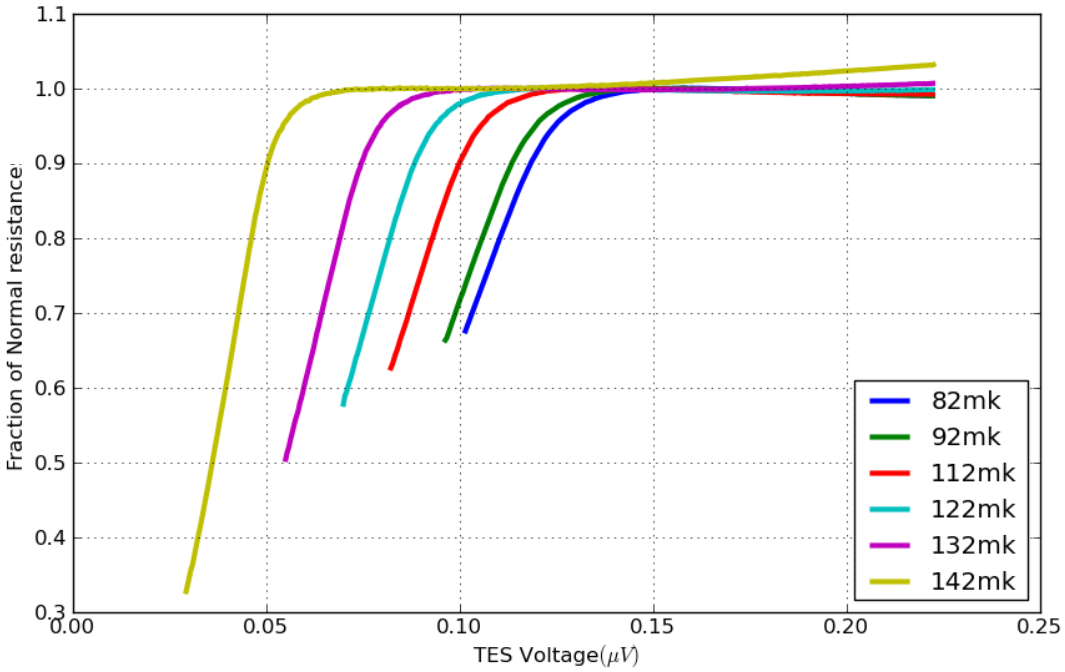

Figure 24: Plot of the TES resistance as a percentage of its normal resistance versus the TES bias voltage used in determining the operating bias point.

3.1.1.2 Dark NEP

In ZEUS-2 there are four main noise contributions: noise from the background photons, detector noise (i.e. bolometer noise), SQUID readout noise, and noise in the warm electronics including the ADCs and DACs of the MCE. For optimal performance we design the instrument so that the background photon-noise dominates the noise of the system. The various instrument components are specifically designed to achieve such a scenario, with the detector noise being the dominate component after the sky background. The lower limit to the detector noise is determined by the thermal fluctuation noise, TFN,

$$TFN = 2T_c(kG)^{1/2} \quad Watts \cdot Hz^{1/2}, \qquad (7)$$

where T_c is the transition temperature of the TES, k is Boltzmann's constant and G is the

thermal conductance of the bolometer (Irwin & Hilton 2005). To achieve the background limited condition requires that we lower the TFN to be less than the sky background by lowering the G and T_c while still achieving the required saturation power and detector time constant. One method to achieve both of these requirements is going to a lower bath temperature; a fact that predicated the need to go to an ADR based system over ZEUS-1's helium-3 fridge. Given the ZEUS-2 detector bath temperature, 120 mK, and the measured thermal conductance and transition temperatures of our bolometers of the 400 μm array (~ 80 pW/K and ~170 mk respectively), we have an expected TFN of $\sim 1 \times 10^{-17}$ Watts $Hz^{-1/2}$. This is ~ 3 and 5 times smaller than the expected photon-noise in the 350 and 450 μm bands respectively (see Table 2) so that we expect ZEUS-2 should be deeply background limited.

Confirming that the ZEUS-2 system should be background limited when observing can be achieved by measuring the noise contributed to the system by the detector and readout electronics when the array is unilluminated. To measure this dark noise-equivalent-power, dark NEP, we cover the detectors so they see a blackbody at the same temperature as their 120 mK bath. While the TES is biased we then take high frequency samples at 15 kHz for 20 seconds. The time stream of SQ1 feedback voltages are converted to power units using equations 1-4 and Fourier transformed to produce a power spectrum. Figure 25 show the dark noise spectrum for one detector at various detector bias points. As calculated later in Section 3.2, the expected NEP for a background limited detector in the 350 and 450 micron windows is $\geq 3.3 \times 10^{-17}$ W $Hz^{-1/2}$. Based on measurements, like the one in Figure 25, our pixels have dark NEPs $\sim 2 \times 10^{-17}$ W $Hz^{-1/2}$ while biased at 30% of their normal resistance so that we expect that ZEUS-2 to be very close (within ~20%) of the background limit when observing on-sky and chopping at 2 Hz.

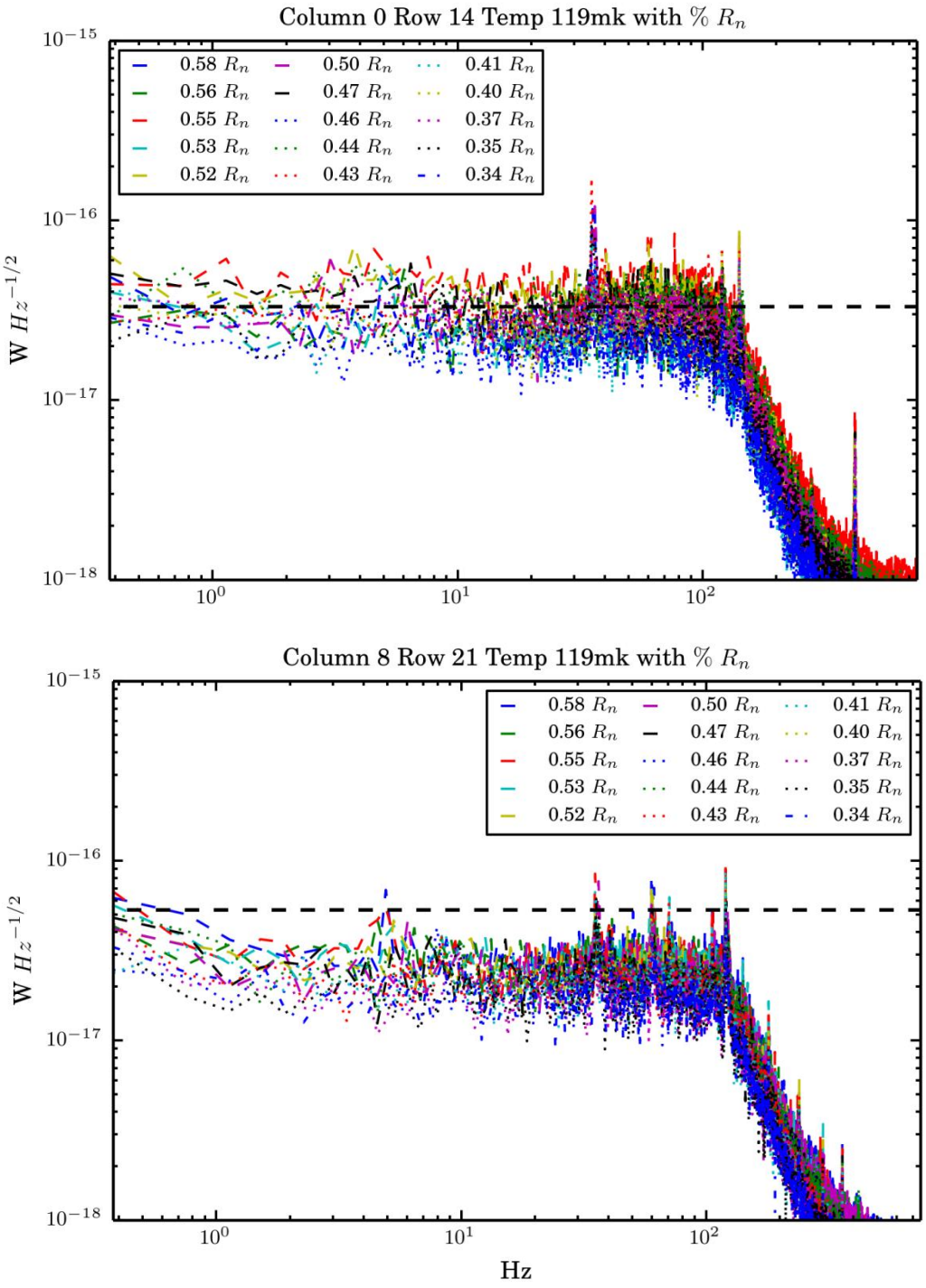

Figure 25: Dark NEP-spectrum for ZEUS-2 bolometers in the 450 µm (top) and 350 µm (bottom) bands at various TES bias points indicated by their faction of the TES normal resistance. The expected photon-NEP for each band, as determined in Section 3.2, is indicated by the thick dashed line.

3.1.2 *Lab Spectrum*

Measurements were made of a chopped liquid-nitrogen cold-load as well as a chopped 80-Celsius heater to assess the responsivity of the system. For background limited performance we expect the signal to noise to be ~20,000 and 2,000 in an integration of 1 second, which we achieved when chopping on cold and hot loads respectively. Figure 26 show the response of the 400 micron array when observing a chopped liquid-nitrogen cold-load. Lastly a lab spectrum (Figure 27) was obtained by observing the chopped heater through a CO gas cell. The grating is calibrated by tilting the grating to move this absorption line across the detector.

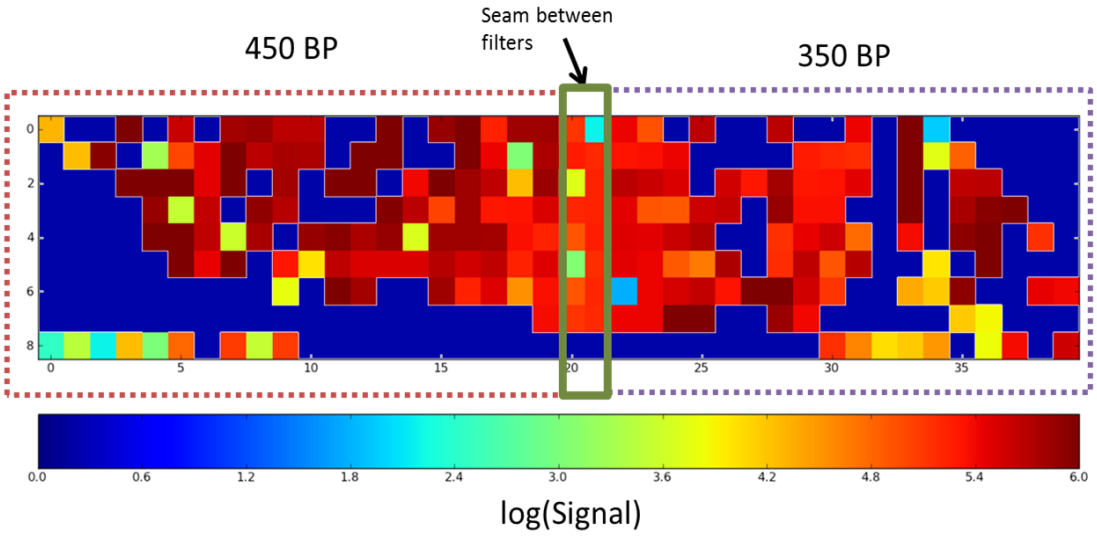

Figure 26: 2D plot of response to a chopped liquid nitrogen cold-load for the ZEUS-2 400 micron array. Typical noise across the array is ~1000 in 2.5 ms, the detector readout period, resulting in SNR of ~ 20,000 in 1sec—the value expected for background limited performance—for most of the pixels. If should be noted, that any pixel with response < half that of the best pixel, is essentially useless, since such pixels would require > 4 times more integration time to reach the same signal to noise.

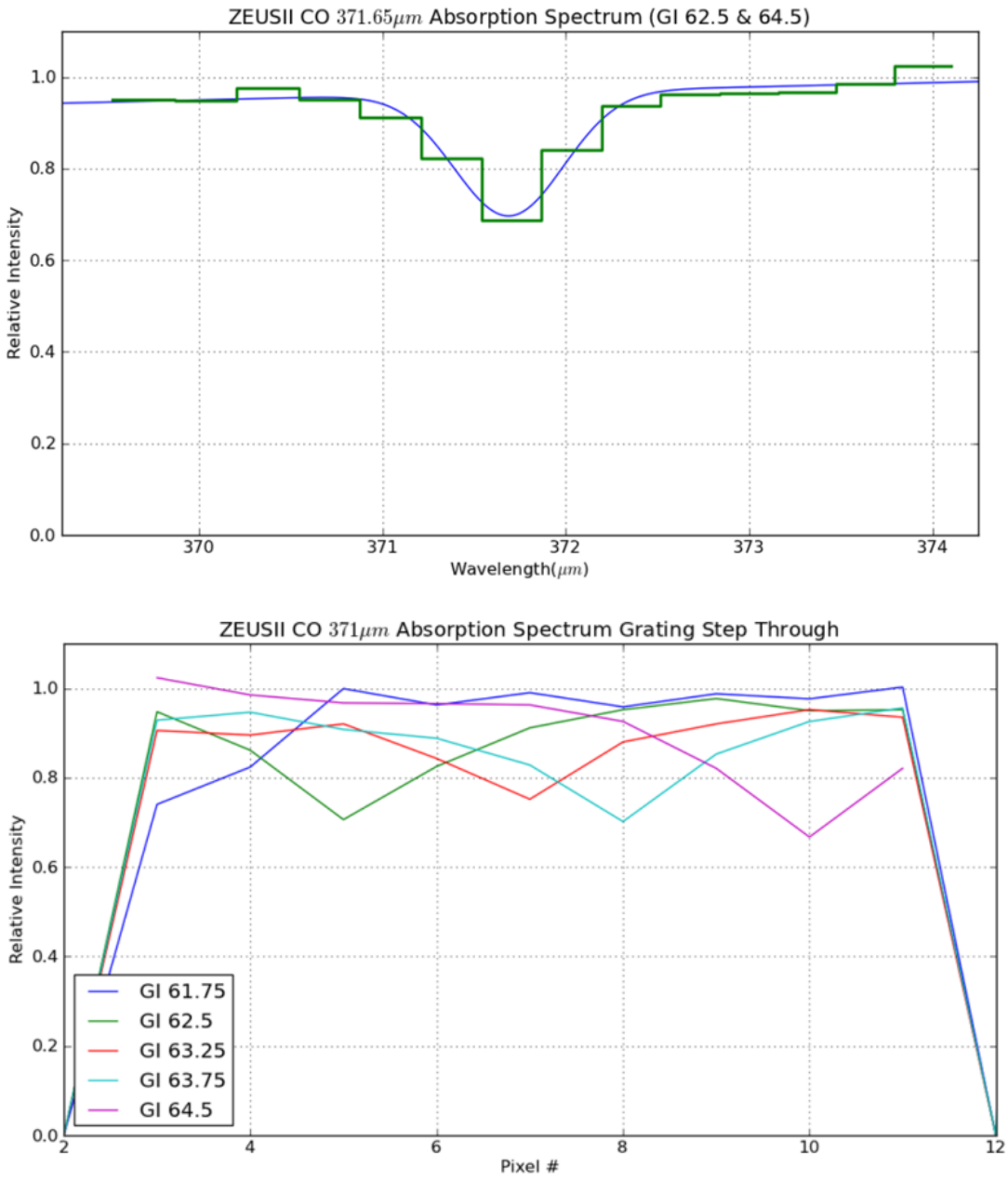

Figure 27: (top) Lab spectrum of a CO 6-5 absorption line. (bottom) The CO line is walked across the detector by changing the grating angle parameterized by grating index GI. All data has been divided by the signal of the chopped hot load when no CO gas is in the cell.

3.2 *Sensitivity*

Here we describe the sensitivity of ZEUS-2 based on models, lab tests, and first light observations at APEX. As previously mentioned we desire that ZEUS-2 be background limited requiring that the system noise is dominated by the statistical fluctuations in the arrival of photons from the background at the detector. At submillimeter wavelengths the background is the sky-emission with temperature T and emissivity ε. In such cases the root mean variance in the number of photons falling on the detector is (Benford, Hunter & Phillips 1998),

$$(\Delta N)_{RMS}{}^2 = rt\eta\tau\varepsilon\bar{n}(1+\eta\tau\varepsilon\bar{n}), \qquad (8)$$

where η and τ are the detector quantum efficiency and instrument throughput respectively, *t* is the integration time, $\bar{n} = (e^{h\nu/kT}-1)^{-1/2}$ the average photon mode occupation number and *r* is the number of photon modes interacting with the detector, equal to

$$r = \frac{2A_t\Omega}{\lambda^2}\Delta\nu. \qquad (9)$$

A_t is the area of the telescope, Ω the solid angle of observation, and λ and Δν the wavelength and spectral bandwidth of the observation respectively. It is useful to characterize the variance in the arrival of photons in terms of noise equivalent power, NEP. This is the equivalent signal power necessary to produce a signal-to-noise ratio of 1 in integration time *t*,

$$\frac{S}{N} = \frac{NEP/_{h\upsilon}\cdot t}{(\Delta N)_{RMS}} = 1. \qquad (10)$$

Solving for the NEP and substituting in Equation 8, we get

$$NEP = h\nu\cdot\frac{(\Delta N)_{RMS}}{t} = h\nu\cdot\left\{\frac{r\eta\tau\varepsilon\bar{n}}{t}(1+\eta\tau\varepsilon\bar{n})\right\}^{1/2} \qquad Watts\cdot Hz^{-1/2}. \qquad (11)$$

Referring to the front end of the dewar, only a fraction $\eta \cdot \tau \cdot \tau_{warm}$, of the incoming photon stream is detected so that the noise equivalent flux, the flux of a source necessary to produce a signal to noise ratio of 1, is then

$$NEF = \frac{2}{A_t}\frac{NEP}{\eta \cdot \tau \cdot \tau_{warm}}, \qquad (12)$$

where the factor of 2 accounts for losses due to chopping of the secondary and τ_{warm} is the warm efficiencies of the instrument and telescope system. Referred to the front end of the dewar, τ_{warm} is just the warm transmission of the instrument—essentially just the transmission of the dewar window. Referred to an astronomical point source, we must also correct for the losses through the sky and telescope ($\eta_{sky}$and η_{tel}) and the point-source coupling (η_{point}). The losses from the sky are given by the atmospheric transmission of the sky determined by the amount precipitable water vapor (PWV) and the air mass through which an observation is made. The through-put of the telescope to ZEUS-2 is primarily set by the surface roughness of the primary dish (17 and 14 μm RMS for APEX and CSO respectively). Lastly, the point-source coupling is determined by the fraction of the airy disk in the focal plan covered by one pixel, i.e. the fraction of power from a point-source that can be coupled to a single pixel.

Using the equations for NEP and NEF above along with the values listed in Table 1, we calculate the point source sensitivities of ZEUS-2 on the CSO and APEX in terms of the minimum detectable line flux (MDLF) that can be observed at the 5σ level in four hours of integration time. Table 2 lists these sensitivities at the center of each ZEUS-2 band along with the wavelength specific parameters necessary for calculating the sensitivities. Figure 28 plots the MDLF as function of wavelength for ZEUS-2, ZEUS-1, the Herschel instruments and the ALMA array. ZEUS-2 is ~1.35 and 1.6 times more sensitive than ZEUS-1 at 350 and 450 μm

bands. The ZEUS-2 sensitivities significantly exceed the sensitivities of all current and recent single dish systems, including Herschel. Except at 200 μm, where ZEUS-2 is equally sensitivite to the PACS-Spectrometer but ~2.5 better spatial resolution, ZEUS-2 is about 10 times more sensitive than the Herschel spectrometers.

ZEUS-2 is competitive even when compared to ALMA. One would expect that the main ALMA array of 12-m dishes would be 50 times more sensitive than ZEUS-2 on APEX since ALMA uses fifty antenna of the same type as APEX, i.e. it has 50 times more collecting area. However, the direct-detection bolometers that we use within ZEUS-2 are significantly more sensitive than a heterodyne system. First, a direct dection spectrometer like ZEUS-2 doesn't have the fundamental noise floor due to quantum noise that exsists with a heterodyne reciever. Furthermore, even the best heterodyne systems, such as the ALMA recievers are still a factor of ~4 worse than this limit (Stacey et al. 2011). Including the contributions from the sky emissivity, it can be shown that ZEUS-2 is ~ 3 times more sensitive than an ALMA receiver on a single dish at 350 and 450 μm. This direct-detection sensitivity advantage reduces ALMA's performance advantage by ~ 2/3, where the numerator is due to ALMA not needing to chop. This means that in ZEUS-2's primary bands at 350 and 450 microns—ALMA bands 10 and 9 respectively—the final 12-m ALMA array is respectively only 30 to 40 times more sensitive. ZEUS-2 fairs even better when one considers ALMA's considerable observational overheads, such as phase-calibration, that are necessary for ALMA observations in these bands. These overheads can easily be ≥100% of the required onsource integration time, negating ALMA's benefit from not having to chop.

All this suggests that ALMA and ZEUS-2 have excellent scientific synergies. Any source whose far-IR fine structure emission can be detected with ZEUS-2 can also be mapped with

ALMA in ~30 beams across the source with the same sensitivity per beam as the ZEUS-2 detection and in the same integration time. Clearly, first observing a source with ZEUS-2 to determine its line flux makes it much easier to estimate the integration times necessary to map a source's emission with ALMA. Lastly, compared to the 4-antenna ALMA total-power array, ZEUS-2 is equally sensitive at 450 microns and twice as sensitive at 350 microns so that ZEUS-2 is useful in measuring emission over large spatial scales that is resolved out by ALMA in very high-resolution observations.

Table 1: Parameters for Calculating NEP at the Detector

Parameter		Value[a] APEX (CSO)	Units
Telescope Diameter	D	12 (10.4)	meters
Sky Temperature	T	265	K
Sky Emissivity[b]	ε	1-η_{sky}	…
DQE	η	0.90	…
ZEUS-2 Instrument Throughput[c]	τ	0.29	…

[a] Parameters for ZEUS-2 on APEX and if different, the CSO values in parenthesis.
[b] The sky transmission η_{sky} is based on models for a specific telescope site and PWV.
[c] Includes DQE. It is determined by comparing detector saturation powers obtained via IV curves when the detector is illuminated by a nitrogen cold load and an 80° C blackbody.

Table 2: ZEUS-2/CSO and ZEUS-2/APEX Sensitivities and System Parameters at the Band Center

Band Center (μm)	Slit (“)	R (λ/Δλ)	η_{sky}	η_{tel}	Power at Detector (Watts)	NEP at Detector (W $Hz^{-1/2}$)	η_{pix}	NEF[a] (W m^{-2} $Hz^{-1/2}$)	MDLF[b] (5σ, 4hrs, W m^{-2})
APEX:	0.2 mm precipitable water vapor (PWV) for 200 – 300 μm bands, 0.5 mm at longer wavelengths								
202	5.6	1550	0.33	0.19	3.8E-12	1.2E-16	0.90	1.3E-16	3.8E-18
233	6.2	1600	0.33	0.25	2.3E-12	8.3E-17	0.86	7.5E-17	2.2E-18
295	6.9	1160	0.36	0.34	2.0E-12	7.3E-17	0.78	5.4E-17	1.6E-18
354	7.5	980	0.53	0.40	1.2E-12	5.3E-17	0.71	2.3E-17	6.8E-19
451	9.4	900	0.58	0.46	5.9E-13	3.3E-17	0.57	1.5E-17	4.4E-19
626	15	580	0.60	0.50	8.3E-13	3.5E-17	0.76	9.4E-18	2.8E-19
830	18	460	0.87	0.55	1.8E-13	1.2E-17	0.59	2.5E-18	7.5E-20
CSO:	Assumes 0.72 mm PWV								
354	8.7	980	0.38	0.41	1.5E-12	5.9E-17	0.71	4.1E-17	1.2E-18
451	11	900	0.43	0.52	7.1E-13	3.6E-17	0.57	2.3E-17	6.9E-19
626	17	580	0.46	0.64	1.1E-13	3.8E-17	0.76	1.3E-17	3.9E-19
830	21	460	0.83	0.70	2.1E-13	1.3E-17	0.59	3.0E-18	8.9E-10

[a]This is the noise equivalent flux for a point source detection, which includes the coupling to the pixel η_{pix}.
[b]MDLF is minimum detectable line flux (5σ) from a point source in 4 hours integration time.

3.3 *On-sky Performance*

Lab measurements indicate about half of the ZEUS-2 pixels are within ~20% of the background limit at 350 and 450 μm. We can confirm this and assess ZEUS-2's on-sky performance by examining the noise in our first light measurement of the high-z galaxy SDP11. As discussed in Chapter 3, the observed [CII] 158 micron line flux from SDP11 is (6.44 ± 0.42) × 10^{-18} W m^{-2} detected in 66 minutes of integration time through ~0.5 mm precipitable-water-vapor. Scaling the 1σ error to the expected 5σ signal obtained in four hours of integration time and accounting for the observed line falling in two spectral bins, the 65% chopper efficiency used in the data reduction and the measured $\eta_{tel} \cdot \eta_{point}$ efficiencies (~20% as measured on Uranus), we get an on-sky MDLF of 4.83 × 10^{-19} W m^{-2}, which is ~1.03 times the expected value 4.71 × 10^{-19} W m^{-2} at the sky wavelength of 438.4 microns. Within the uncertainties of the instrument throughput, DQE, telescope efficiencies, point-source coupling and flux calibration, the observations of SDP11 demonstrate that ZEUS-2 is background limited in its 450 micron band.

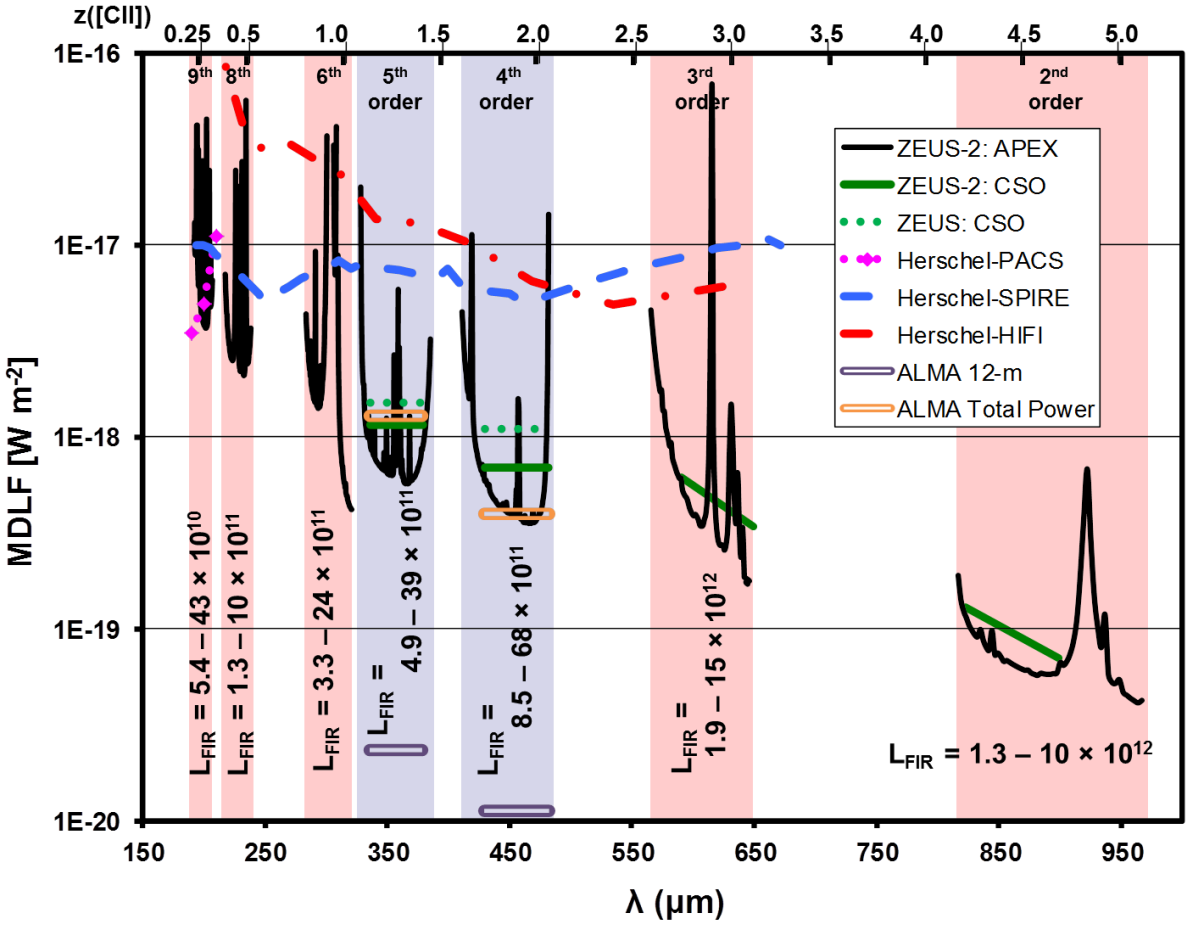

Figure 28: The minimum detectable line flux of a 5σ detection obtained in 4 hours of integration for ZEUS-2 on APEX and CSO. Blue shading indicates the ZEUS-2 primary bands. Telluric transmission models are used with 0.5 mm and 0.72 mm of precipitable water vapor for APEX and CSO respectively, except for wavelengths < 300 μm where we use 0.2 mm. Also plotted is the sensitivity of ZEUS (Hailey-Dunsheath 2009), the sensitivities of the 3 Herschel spectrometers as well as the full ALMA 12-m and Total Power arrays [9,10,11,12]. For comparison we have scaled the resolving power of all instruments to that of ZEUS-2, i.e. R~1000 or Δv = 300 km s^{-1}. The echelle orders and the corresponding [CII] redshift intervals are listed, plus the range of galactic Far-IR luminosities that we would expect to be able to produce a [CII] line with the MDLF shown. We assume the ratio of the [CII] to Far-IR luminosities is between 0.04% to 0.3% as we found in Stacey et al. 2010 and H_o = 71 km s^{-1} Mpc^{-1}, Ω_o = 1 and Ω_Λ= 0.7.

[9] Herschel-PACS sensitivities retrieved from the "PACS Observer's Manual" HERSCHEL-HSC-DOC-0832, Version 2.1, (1 June 2010, accessed 25 October 2010) http://herschel.esac.esa.int/Docs/PACS/html/pacs_om.html

[10] Herschel-SPIRE sensitivities retrieved from the "Herschel Observation Planning Tool", v5, (accessed 25 October 2010) ftp://ftp.sciops.esa.int/pub/hspot/HSpot_download.html

[11] Herschel-HIFI sensitivities retrieved from the "HIFI Observers' Manual", HERSCHEL-HSC-DOC-0784, version 2.0, (20 May2010, accessed 25 October 2010), http://herschel.esac.esa.int/Docs/HIFI/html/hifi.html

[12] ALMA sensitivities of the full 12-m and Total Power arrays were retrieved from the "ALMA Sensitivity Calculator", (accessed 18 November 2013), http://almascience.eso.org/proposing/sensitivity-calculator

4 SUMMARY

The design of ZEUS-2 was driven by our goal to study the star formation history of the universe from just a few billion years after the big bang to the present epoch. Building on the work of ZEUS-1, we will (1) investigate star formation from z ~ 0.25 to 5 by measuring the redshifted fine-structure lines of distant galaxies, (2) obtain redshifts from optically obscured galaxies by detecting the bright [CII] 158 μm line, and (3) investigate the properties of nearby starburst and ultra-luminous galaxies through their [CI] fine-structure and CO rotational lines.

ZEUS-2 is an excellent instrument for this work as the moderate resolution and diffraction-limited beams of the long-slit echelle-grating, combined with our chosen pixel-scale, concentrates all the line-flux from a point-source onto a single pixel—making it relatively easy to be background limited. The diffraction limited beams also ensure that the beam contains only the minimum background noise required for a line detection. ZEUS-2 is therefore optimized for the detection of the broad, faint lines we expect from distant point-source galaxies. Combined with the three state-of-the-art TES bolometer arrays that are tuned for optimal efficiencies at 215, 400, and 625 microns, ZEUS-2 achieves sensitivities on single-dish observatories that are unparalleled from ground or space. The three arrays also allow ZEUS-2 to obtain spectra from up to nine spatial positions on the sky and access to seven different bands between 200 and 850 microns so that ZEUS-2 excels at mapping of nearby systems and is competitive for redshift searches of distant sources.

Both lab measurements and observation of a high-z galaxy confirms that ZEUS-2 is indeed very close (within ~20%) to the background limit. Its exquisite sensitivity makes ZEUS-2 an important instrument for studying galaxies across cosmic time. In the coming years ZEUS-2 has an important role to play as a discovery instrument, makeing intial line detections that can then be followed-up with ALMA to resolve the emission. Ultimately ZEUS-2, even in the ALMA era, will be able to provide unique and important clues to the formation and evolution of galaxies from early times to the current epoch.

REFERENCES

Battistelli, E.S., Amiri, M., Burger, B., et al. (2008), J Low Temp Phys, 151, 908-914

Benford, D.J, Hunter, T. R., and Phillips, T. G. (1998). Int. Journal of Infrared and Millimeter Waves, 19,7, 931-938

Benford, D.J., Gaidis, M.C., & Kooi, J.W., (2003), Applied Optics, 42, 25, 5118-5122.

Brisbin, D., Ferkinhoff, C., Nikola, T., et al. (2013), ApJ, submitted

De Korte, P. A. J., Beyer, J., Deiker, S., et al. (2003), Rev. of Sci. Inst. Vol. 74, 8.

Ferkinhoff et al. (2013), ApJ, in press.

Ferkinhoff, C., Hailey-Dunsheath, S., Nikola, T., et al. (2010), ApJL, 714, L147

Ferkinhoff, Brisbin, D., Nikola, T., et al. (2011), ApJL, 740, L29

Hailey-Dunsheath, S., Nikola, T., Stacey, G.J., et al. , (2008), ApJL, 689, L109-L112 .

Hailey-Dunsheath, S., Ph.D. Thesis, Cornell University (2009)

Hailey-Dunsheath, S., Nikola, T., Stacey, G. J., et al. (2010), ApJL, 714, L162

Irwin, K. D., & Hilton, G. C., (2005), Cryogenic Particle Detection, C. Enss, ed., Topics Appl. Phys., 99, 63-149

Muething, K., Ihas, G.G., & Landau, J., (1977), Rev. Sci. Instrum., 48, 7, 906-909.

Nikola,T., Stacey, G. J., Brisbin, D., et al. (2011), ApJ, 742, 88

Rieke, G. H (2002) Dection of Light, From the Ultraviolet to the Submillimeter, 2nd Ed., Cambridge University Press.

Roach, P., (1998), Nasa Tech Briefs, http://www.techbriefs.com/Briefs/Apr98/ARC11983.html

Smith, S.M., & Howitt, R.V.,(1986), NASA TM-88204.

Smith, S.M., (1986), Applied Optics 25, 16, 2747-2751.

Stacey, G. J., Hailey-Dunsheath, S., Ferkinhoff, C., et al. (2010), ApJ, 724, 957.

Stacey, G. J. IEEE, Transactions on Terahertz Science and Technology, 2011

Weisend II, J.G., (1998), Handbook of Cryogenic Engineering, Taylor & Francis, Philadelphia.

POSTFACE: LOOKING FORWARD ON THE INFRARED UNIVERSE

In the proceeding chapters we have covered important methods for studying early galaxies through the observation of the [OIII], [NII] and [CII] fine-structure lines using our spectrometers ZEUS-1 and ZEUS-2. The observations we described however, are just the starting point. There is much work yet to be done in spatially resolving the emission we detected with both ZEUS-1 & 2, using ZEUS-2 to expand our survey of fine-structure lines in early galaxies and investigating complexities of [CII] emission that have recently become apparent from our studies.

The primary tool for resolved studies of the fine-structure lines of high-z galaxies is ALMA since it began science operations in 2012. As part of the early science phase and the observing cycles since, we have had programs to resolve the [CII] emission from our ZEUS-1 sample of sources using ALMA Band 9. However, due to challenges in observing in this band, these have yet to bear fruit, but another ALMA program that mapped the [NII] line in SMMJ02399 and the Cloverleaf have produced fantastic maps. Analysis of these exciting data is ongoing, and will provide vital details on the nature of the [NII] line emission in those sources.

As of December 2012 about half of all high-z detections of fine-structure lines had been made by ZEUS-1. With ZEUS-2 we are now poised to further our already significant contribution to the number fine-structure line detections in early galaxies. We will continue to observe galaxies between $z \sim 1 - 2$ in their [CII] emission to improve the statistical rigor of our conclusion, but we will also expand our observations to include other lines and a wider range of redshifts. Based on the work in Chapters 1 and 2, observations of the [OIII] 88 μm and [NII] 122 μm lines are especially high priority. Performing a survey of these lines will allow us to (1)

measure the age of the starburst in our sources to probe the evolutionary connection between starburst galaxies and AGN, (2) further test the relationship between star formation rate surface density and ionized-gas mass as seen at lower redshifts that we discovered in Chapter 2 and (3) determine the number and type of the most massive stars still on the main sequence to constrain the high-mass end of the stellar initial mass function (IMF) at high redshift.

The prospect of the last goal is especially compelling. Galaxies locally are well fit by more or less "universal" stellar initial-mass-function characterized by a power-law with Salpeter-index ($\alpha = 2.35$) for stars above ~ 1 solar mass. However, in the extreme star-forming environments of early galaxies (e.g. SFR ~ 1000 $M_{\odot}$ yr^{-1}) there is compelling evidence for a top-heavy IMF, i.e. galaxies have a higher fraction of high-mass stars than in local systems (Bastian, Covey, Meyer 2010). For instance a top heavy IMF is invoked when explaining the number of observed SMG's (Baugh et al. 2005) or the present day stellar mass density (Wilkins et al. 2008). Direct measurements of the IMF, especially in the early universe, are quite difficult. However, using the [OIII] and [NII] lines we can directly sample the high-mass end of the IMF in our targets and determine if early galaxies do indeed tend towards a top-heavy IMF.

Just as IRAS, then COBE, and eventually SCUBA made discoveries that answered questions about galaxies only to have these same discoveries raise new questions, our studies with ZEUS-1 have raised new questions as well. As discussed in Chapter 3, our observations of the [CII] line suggest that high-z ULIRGs need not be powered through the merger of two or more massive galaxies, though it is definitely possible as we argue for SDP11. Our observations have also revealed complexities in our understanding of the [CII] line. In local galaxies [CII] arises mostly in the neutral and molecular hydrogen phases of the ISM within photo-dissociations regions, with only ~30% of the line emission coming from ionized gas. In our latest

batch of ZEUS-1 observations however there is strong indication that in some sources it could be reversed with ~70% of the emission coming from the ionized gas and the PDR only producing 30% (Brisbin et al. 2014). To further complicate matters, some sources indicate that [CII] emission is being enhanced by shock-compression of PDRs. An important project will be to obtain low-J CO observations from these sources to confirm that there is indeed a non-PDR source of [CII] emission. Unfortunately, all of the sources are too far north to be observed with ALMA, so we will have to observe them with the Plateau de Bure Interferometer. Perhaps more important is the need to use ZEUS-2 to observe the [NII] 205 μm line in these sources Having similar critical density, temperature of excitation, and ionization potential to [CII], the [NII] 205 μm line is an ideal tracer of the amount of [CII] emission coming from the ionized medium.

The scientific potential of both ZEUS-2 and ALMA makes it an exciting time to be studying galaxies in the early universe, especially via the far-IR fine-structure lines. In the years to come we will make great strides in our understanding of early galaxies, answering many of today's outstanding questions. Equally likely is that for every question we answer, a new one will emerge. Addressing these new questions will undoubtedly require more sensitivity and larger sample sizes than the generation of questions that came before. Luckily there is already work being done to ensure the next generation of observatories and instruments will be available to answer the new questions being revealed by ZEUS-1 & 2, and ALMA. CCAT, a proposed 25-m submillimeter telescope to be built near ALMA in the Atacama Desert in Chile, will be a vital tool to address the next set of questions with large-format cameras, a multi-object spectrograph, and a large field of view. CCAT will excel at performing large-scale surveys of the sky at submillimeter wavelengths, detecting thousands of galaxies in both their continuum and the far-IR fine-structure lines, allowing our understanding of the Universe to evolve still further.

REFERENCES:

Bastian, Covey, Meyer 2010, ARA&A, 48, 339

Baugh et al. 2005, MNRAS, 356, 1191

Brisbin et al. 2014, ApJ, submitted

Wilkens et al. 2008, MNRAS, 391, 363